WARWICK
THE UNIVERSITY OF WARWICK

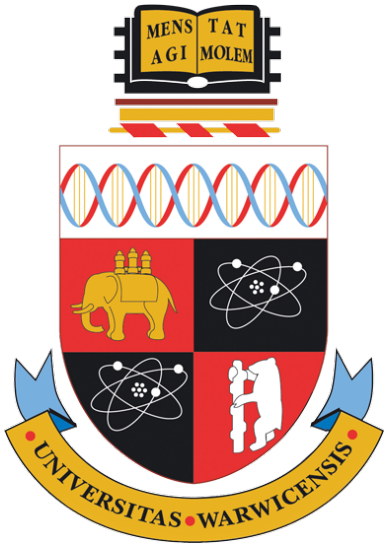

Sensitivity of the first ATLAS measurement of the CKM matrix element $|V_{cb}|$

by

Vangelis Vladimirov

Thesis

Submitted to the University of Warwick

in partial fulfilment of the requirements

for admission to the degree of

Doctor of Philosophy in Physics

Department of Physics

January 2022

Contents

List of Tables

List of Figures

Acknowledgments

I owe thanks to every member, both present and past, of the Warwick ATLAS group for providing an accommodating working environment. I would like to thank my supervisor, Paul Harrison, for his patience and guidance throughout the duration of my project. I am also grateful for working on this analysis alongside Bryn Roberts. Special thanks go to Tim Martin, who was always happy to help me with anything ranging from C++ related questions to Geneva's public transportation. Also thank you to William Murray for frequently imparting his vast knowledge. Thank you to Adomas Jelinskas, Christopher McNicol and Martin Spangenberg, who helped me get comfortable with the ATLAS workflow. Finally, I would like to express my gratitude to Ankush Mitra and Keith Jewkes for their help and guidance with my ATLAS authorship task. Everyone else not mentioned by name, please know that the time spent together is appreciated.

Of course, this analysis would have been impossible to undertake without the countless personnel ensuring the successful operation of the LHC and the ATLAS experiment. In addition, I would like to thank the Top Reconstruction and Top Properties working groups, and in particular Tomáš Dado for his continuous help.

In the end, I would like to thank my parents for always supporting me in anything I do.

Declarations

This work is submitted to the University of Warwick as part of my application for the degree of Doctor of Philosophy. It was produced by me and has not been submitted for any other degree applications.

My contribution to ATLAS as my authorship qualification task was to finalise the data taking and estimate the effects of thermal variations on the future ITk strip modules of High Luminosity Large Hadron Collider (HL-LHC). The work is described in Chapter 4.

The main research presented in this thesis is the optimisation of the measurement of the Cabibbo-Kobayashi-Maskawa (CKM) matrix element $|V_{cb}|$ using the ATLAS experiment and the estimation of its error using Monte Carlo simulated events. The whole analysis team is based in the University of Warwick and consists of myself, Bryn Roberts and our supervisor, Paul Harrison. My contributions to the analysis consisted of:

- collaborating in the preparation of a feasibility study for the analysis [1]
- developing the analysis framework in the programming languages C++ and Python using ROOT [2, 3]
- developing bespoke truth matching code for the simulated analysis
- investigating and developing object and event selection criteria optimised for background rejection
- selecting the optimal for the analysis c-tagging working point
- implementing the treatment of systematic uncertainties.

1 Sponsorships and Grants

This research was funded by the Science and Technology Facilities Council.

Abstract

The sensitivity of the measurement of the magnitude of the Cabibbo-Kobayashi-Maskawa quark-mixing matrix element $|V_{cb}|$ was estimated using full Monte Carlo simulation of the data recorded by the ATLAS experiment. The Monte Carlo dataset corresponds to the luminosity of 139 fb^{-1} at centre-of-mass energy of $\sqrt{s} = 13$ TeV which was recorded by the ATLAS experiment during the full Run 2 of the Large Hadron Collider. The analysis utilises the on-shell W boson decays in top quark pair events in which one top quark decays leptonically, $t \to Wb \to (\ell\nu)b$, and serves as the tag of the event, while the other top quark decays hadronically, $t \to Wb \to (cb)b$. Selection criteria were implemented in order to reject background events stemming from single top, W+jets, Z+jets and diboson events, as well as other top quark pair decay modes. Finally, a maximum likelihood method was used to reach the estimation of the fractional sensitivity of the measurement of $\Delta|V_{cb}|/|V_{cb}| = 0.14(\text{stat.}) \oplus 0.10(\text{syst.})$. The outlined analysis will be the first attempt to measure $|V_{cb}|$ at the energy scale of the on-shell W boson mass, $Q^2 \sim (10^4)$ GeV^2.

Acronyms

ALICE A Large Ion Collider Experiment
ASIC application specific integrated circuit
ATLAS A Toroidal LHC ApparatuS
BDT boosted decision tree
BSM Beyond the Standard Model
CCWI charged current weak interaction
CDF cumulative distribution function
CERN the European Organisation for Nuclear Research
CKM Cabibbo-Kobayashi-Maskawa
CMS Compact Muon Spectrometer
CSC cathode strip chamber
ECal Electromagnetic Calorimeter
EM electromagnetic
FSR final state radiation
HCal Hadronic Calorimeter
HL-LHC High Luminosity Large Hadron Collider
HLT High Level Trigger
ID Inner Detector
IP interaction point
ISR initial state radiation
ITk Inner Tracker
JER jet energy resolution
JES jet energy scale
JVT jet vertex tagger
L1 Level-1 trigger
LAr liquid Argon
LEP the Large Electron-Positron collider
LHC Large Hadron Collider
LHCb Large Hadron Collider beauty
Linac 2 the Linear Accelerator 2
LS long shutdown
MC Monte Carlo
MCEG Monte Carlo event generator
MDT monitored drift tube
ME matrix element
MET missing transverse momentum
ML maximum likelihood
MS Muon Spectrometer
NLO next-to-leading order
NN neural network
NP nuisance parameter
OR overlap removal
PD Pixel Detector
PDF parton distribution function
PFlow particle flow
PMNS Pontecorvo-Maki-Nakagawa-Sakata
PoI parameter of interest
PrDF probability distribution function
PS parton shower
PSB the Proton Synchrotron Booster
QCD Quantum Chromodynamics
QED Quantum Electrodynamics
QFT Quantum Field Theory
QM quantum mechanics
RoI region of interest
RPC resistive plate chamber

SCT Semi-Conductor Tracker
SF scale factor
SM Standard Model
SR special relativity
TGC thin-gap chamber
TRT Transition Ratiation Tracker
WP working point

Chapter 1

Introduction

The field of elementary particle physics studies the smallest indivisible constituents of matter and the electromagnetic, weak and strong interactions between them. The currently accepted mainstream theory in particle physics is the Standard Model (SM), formulated by the global physics community during the second half of the 20th century. Through its development, it has been used to make predictions about the existence of previously unobserved particles, among which are the charm, beauty and top quarks and the Higgs boson. In addition, predictions made with the SM about numerical values of physical quantities have been tested experimentally, including the most accurately predicted value in any theory to date, the anomalous magnetic moment of the electron (the value has been measured to have an agreement with theory up to $\mathcal{O}(10^{-12})$ [4]).

Despite its predictive power, the SM contains a number of free parameters, which are not predicted by the theory and can only be measured experimentally (a list of the SM free parameters can be found in Table 2.2). A subset of these parameters define the values of the Cabibbo-Kobayashi-Maskawa (CKM) matrix elements, which determine the mixing of the mass and weak interaction eigenstates in the quark sector. This results in the different couplings of inter-family quark pairs with the W boson. Measurements of the matrix element $|V_{cb}|$ have been performed in both inclusive ($X_b \to X_c l\nu$) and exclusive ($B \to D^{(*)} l\nu$, $B_s \to D^{(*)} l\nu$) decays of B-hadrons to C-hadrons (hadrons in which the heaviest flavour valence quark is a beauty or a charm quark respectively), Figure 1.1, left.

The inclusive measurements use decays of B-hadrons to C-hadrons and a lepton and depend on the operator product expansion and heavy quark effective theory [5, 6]. The total decay width is connected to $|V_{cb}|$ through Quantum Chromodynamics (QCD) perturbative and non-perturbative corrections expanded in terms of α_s and Λ_{QCD}/m_b respectively, with α_s being the strong interaction coupling strength, $\Lambda_{QCD} \sim 200$ MeV - the representative

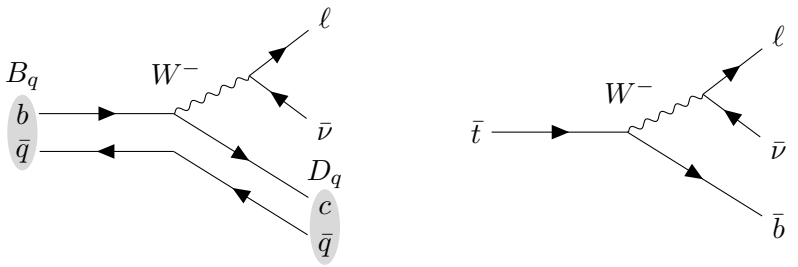

Figure 1.1: Leading order Feynman diagrams of the processes used to measure $|V_{cb}|$ at B-hadron decays (left) and on-shell W bosons in top decays (right).

energy scale of the strong interaction, and m_b - the mass of the beauty quark. Simultaneous fits of heavy quark effective theory parameters in order to over-constrain them using moments of the hadron mass and lepton energy spectra have been performed [7]. The global average of all inclusive measurements is $|V_{cb}| = (42.19 \pm 0.78) \times 10^{-3}$ [8].

In exclusive decays, $|V_{cb}|$ is extracted from the decay rate using form factors $\mathcal{F}(w)$, which are dependent on the product of the B and resulting D meson four-velocities $w = v_B^\mu v_{D\mu}$ and are calculated using heavy quark effective theory at $w = 1$, the "zero recoil point" [9]. Measurements of the differential decay rate $d\Gamma/dw$ are then extrapolated to $w = 1$ to obtain $|V_{cb}|$ [9, 10]. The global average exclusive measurement is $|V_{cb}| = (39.25 \pm 0.56) \times 10^{-3}$ [8], leading to a discrepancy of $\sim 3\sigma$ between the inclusive and exclusive measurements. The averages of both types of measurements are shown in Figure 1.2.

While the first measurement of the matrix element at a hadron collider was performed by the Large Hadron Collider beauty (LHCb) collaboration using exclusive $B_s \to D_s^{(*)-}\mu^+\nu_\mu$ meson decays [12], the analysis presented in this thesis aims to be the first measurement of $|V_{cb}|$ using decays of on-shell W bosons produced in top quark decays (Figure 1.1, right). The energy scale of the interaction is $Q^2 \sim m_W^2 \sim \mathcal{O}(10^4)$ GeV^2, compared to the energy scale of B-hadron decays, $Q^2 \sim \mathcal{O}(10)$ GeV^2. While the parameters of the CKM matrix are known to be "running" (they have a dependence on the energy scale of the interaction) at energies above m_W [13], below this scale, the matrix elements are considered to be constant, with all energy dependence absorbed into the quark masses and higher dimension operators [9]. Thus, the analysis at $Q^2 \sim m_W^2$ can be used as a direct and independent way of measuring the CKM matrix element at the weak scale. The measurement is performed using $t\bar{t}$ (top quark pair) decay events recorded by the A Toroidal LHC ApparatuS (ATLAS) experiment during the full Run 2 of proton-proton (pp) collisions at centre-of-mass energy $\sqrt{s} = 13$ TeV of the Large Hadron Collider (LHC), corresponding to an integrated luminosity of ~ 140 fb^{-1}.

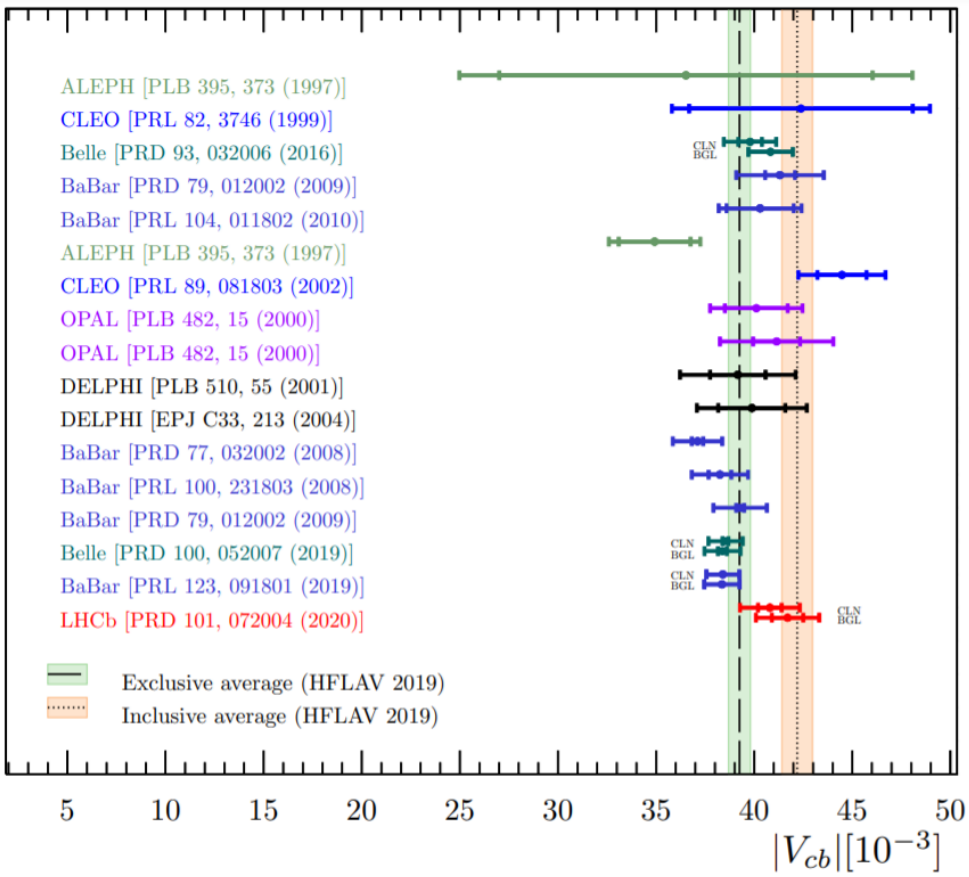

Figure 1.2: Exclusive $|V_{cb}|$ measurements and their average (green band), excluding LHCb 2020 and BaBar 2019. The outer (inner) error bars represent the total (statistical) uncertainty of the measurements. The orange band represents the world average of inclusive measurements. CLN (Caprini, Lellouch, Neubert) and BGL (Boyd, Grinstein, Lebed) represent different parameterisations used in the exclusive determination, with CLN being used unless otherwise stated. Taken from [11].

Chapter 2

Theoretical background

The theoretical model used for describing all elementary particles and interactions in nature (apart from gravity, which is described at large scales by general relativity) is the Standard Model (SM) of particle physics. The SM is an example of a Quantum Field Theory (QFT), a type of theory which combines classical field theory, quantum mechanics (QM), and special relativity (SR). In this theory, physical particles are quanta of their corresponding fields defined at every point $(t, \vec{x})$ [1] of a Minkowski space-time manifold characterised by a metric tensor $\eta_{\mu\nu} = diag(1, -1, -1, -1)$[2]. As in QM, observables correspond to Hermitian operators acting on a Hilbert space of states.

2.1 Symmetries in Physics

Physical systems are said to be symmetric if they remain unchanged under an applied transformation. These transformations can be divided into two types - space-time transformations, acting on x^μ, and internal transformations, acting on degrees of freedom associated with the fields of the theory. As a relativistic theory, any QFT must satisfy the two postulates of SR:

- the same laws of physics must apply in all inertial (not undergoing acceleration) frames of reference
- the speed of light in vacuum, measured in any inertial frame, is $c = 1$.

The first postulate can be represented as the requirement that two inertial frames of reference characterised by coordinate systems defining the same point as x^μ and x'^μ observe the same physical quantities, for example the amplitude of the scalar wavefunction ϕ:

$$|\phi(x)|^2 = |\phi'(x')|^2. \tag{2.1.1}$$

[1] The use of natural units is adopted throughout this thesis, where $c = \hbar = 1$.
[2] An equivalent choice is $\eta_{\mu\nu} = diag(-1, 1, 1, 1)$.

In addition, $\phi(x)$ and $\phi'(x')$ must obey equations of motion (defined in Section 2.2) of the same form, in order to preserve the equivalence throughout space-time. A change between inertial frames of reference is achieved by a Poincaré transformation:

$$x^\mu \to x'^\mu = \Lambda^\mu{}_\nu x^\nu + a^\mu, \tag{2.1.2}$$

where $\Lambda^\mu{}_\nu$ is a Lorentz transformation matrix (responsible for boosts and rotations) and a^μ is a space-time translation vector. These transformations preserve the constant velocity of light c between inertial frames of reference, but in contrast to the non-relativistic Galilean transformations, they do not preserve space-distances $|\Delta\vec{x}|$ or time separately. The quantity which is preserved by Poincaré transformations is the space-time interval between events:

$$(\Delta x)^2 = (\Delta t)^2 - (|\Delta\vec{x}|)^2. \tag{2.1.3}$$

The transformations defined by Equation 2.1.2 form the Poincaré group. Irreducible representations (particles) of this group are labeled by the Casimir operators of the group related to mass and spin. The Lorentz transformations also form a group which is split into 4 connected components, which are determined by the signs of $\Lambda^0{}_0$ and $\det(\Lambda)$. The identity element of the group is contained within the proper ($\det(\Lambda) = 1$) orthochronous ($\Lambda^0{}_0 > 0$) subgroup, $\mathcal{L}_+^\uparrow$ or $SO^+(1,3)$. Transformations from the other subsets of the Lorentz group are achieved through the additional application of the discrete space-time operators parity $\mathcal{P} : (t, \vec{x}) \to (t, -\vec{x})$ and time reversal $\mathcal{T} : (t, \vec{x}) \to (-t, \vec{x})$, Figure 2.1.

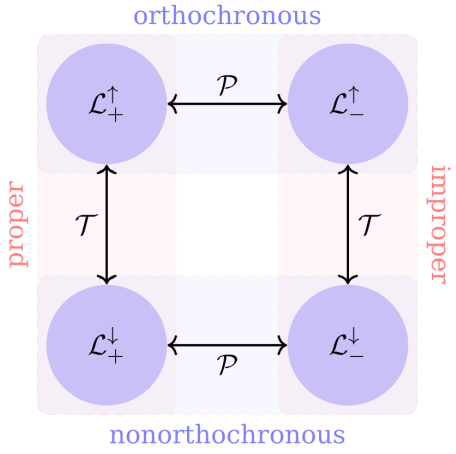

Figure 2.1: The subsets of the Lorentz group connected through the operators of parity ($\mathcal{P}$) and time reversal ($\mathcal{T}$), e.g. $\mathcal{L}_-^\downarrow = \mathcal{P}\mathcal{T}\mathcal{L}_+^\uparrow = \mathcal{P}\mathcal{L}_+^\downarrow$.

Different fields in the SM belong in different representations of the Lorentz Group, meaning they transform differently under Lorentz transformations. The generators of $SO^+(1,3)$ can be divided into two subsets which satisfy the

commutation relations of the group $SU(2)$ separately and commute with each other. A general irreducible representation can be classified by the way it transforms under those two groups as (m, n) - as spin-m and spin-n under the two groups. The fields of the SM can be either scalar $(0, 0)$ (remains invariant under Lorentz transformations), vector $(1/2, 1/2)$, or a Dirac spinor, a direct sum of left- and right-handed Weyl representations $(1/2, 0)\oplus(0, 1/2)$, with each transforming differently under Lorentz transformations [14].

Dirac spinors describe the half-odd-integer spin particles - fermions. In addition to the elementary fermions of the SM - the quarks and the leptons - any composite state of odd number of fermions is also a fermion. Dirac spinors follow anti-commutation rules, resulting in them obeying Fermi-Dirac statistics [15, 16] and the Pauli exclusion principle [17], allowing only one fermion to occupy a state with a particular set of quantum numbers. Some of the consequences of this are the periodic table of elements and the stability of white dwarfs and neutron stars.

Scalars and vectors describe the zero and non-zero integer spin particles respectively - bosons. In the SM, the only elementary scalar boson is the Higgs boson (which is also complex), while the vector bosons emerge from local gauge symmetries, see Section 2.2.1. Bosons obey commutation relations and are not restricted by the Pauli exclusion principle - multiple bosons can occupy the same state. At low temperatures or high concentration, they follow Bose-Einstein statistics [18] instead.

The Lagrangian, which describes any physical system and is defined as the difference between the kinetic and potential energies of a system, $L = K - V$, can be ensured to transform as a scalar under Lorentz transformations when all present Lorentz indices are contracted. Any Lorentz invariant local quantum field theory with a Hermitian Hamiltonian is automatically invariant under the combination of parity, time reversal and charge conjugation (denoted by $\mathcal{C}$ and defined as the transformation which replaces particles with their antiparticles, e.g. $q \to \bar{q}$) transformations [19][3], or $\mathcal{CPT}$. While there has been no experiment indicating $\mathcal{CPT}$ is not an exact symmetry, it is possible to have violation under only one of its constituent symmetries, which automatically implies that there is a violation under the combination of the remaining two. Maximal $\mathcal{P}$ and $\mathcal{C}$ violation in the weak interaction were first discovered in β-decays [20], and $\mathcal{CP}$ violation was observed in neutral kaon decays [21].

[3]This requirement is further relaxed in Ref. [19].

2.2 Lagrangian formalism

In classical mechanics, and by extension in QFT, the fundamental quantity is the action of a system, S, which, in 4 dimensions, is defined as:

$$S = \int L dt = \int \mathcal{L} d^4x, \tag{2.2.1}$$

where L is the Lagrangian and $\mathcal{L} = \mathcal{L}(\{\phi_i\}, \{\partial_\mu \phi_i\})$ is the Lagrangian density, which is a function of a collection of fields and their derivatives. Often, the Lagrangian density is referred to as the Lagrangian. When a system evolves with time, it does so along a path in configuration space which extremises the action:

$$0 = \delta S = \int d^4x \left(\frac{\partial \mathcal{L}}{\partial \phi_i} \delta \phi_i + \frac{\partial \mathcal{L}}{\partial(\partial_\mu \phi_i)} \delta(\partial_\mu \phi_i) \right). \tag{2.2.2}$$

From this, the Euler-Lagrange equation of motion for each field appearing in the Lagrangian can be found:

$$\frac{\partial \mathcal{L}}{\partial \phi_i} = \partial_\mu \left(\frac{\partial \mathcal{L}}{\partial(\partial_\mu \phi_i)} \right). \tag{2.2.3}$$

The appropriate equation describing a free (non-interacting) Dirac spinor field ψ with mass m is the Dirac Lagrangian:

$$\mathcal{L}_{\text{Dirac}} = \bar{\psi}(i\gamma^\mu \partial_\mu - m)\psi, \tag{2.2.4}$$

where $\bar{\psi}$ is the Dirac adjoint spinor, defined as $\bar{\psi} = \psi^\dagger \gamma^0$, and γ^μ are the Dirac matrices. These matrices obey the Clifford algebra $\{\gamma^\mu, \gamma^\nu\} = 2\eta^{\mu\nu}$, with the smallest dimensionality satisfying this relation being 4 (γ^μ are 4×4 matrices, while ψ has 4 components). The Lagrangian describing a scalar boson field is the Klein-Gordon Lagrangian, which, for the case of a free complex field ϕ with mass m, takes the form:

$$\mathcal{L}_{\text{K.-G.}} = \frac{1}{2}(\partial^\mu \phi)^\dagger \partial_\mu \phi - \frac{1}{2} m^2 \phi^\dagger \phi. \tag{2.2.5}$$

The Lagrangian for the SM vector bosons are shown in Sections 2.2.1 and 2.2.2 for Abelian and non-Abelian cases respectively.

Another important concept is the connection between continuous transformations of fields in a theory and conservation laws, Noether's theorem. For such a transformation, $\phi \to \phi + \delta\phi$, to be a symmetry of the system, the equations of motion should remain unchanged. This is achieved if the Lagrangian density is unchanged or changed by the divergence of a vector $\mathcal{K}^\mu$, $\mathcal{L} \to \mathcal{L} + \partial_\mu \mathcal{K}^\mu$.

This leads to the conservation of the current j^μ, defined as:

$$j^\mu = \frac{\partial \mathcal{L}}{\partial(\partial_\mu \phi)} \delta\phi - \mathcal{K}^\mu, \tag{2.2.6}$$

or equivalently, the Noether charge defined as $Q = \int j^0 d^3x$ is a constant in time [14]. Examples of such conserved charges are the energy and the momentum carried by the field under time and spatial translations.

2.2.1 Local (gauge) Abelian symmetries

The following subsection introduces gauge symmetries, the type of symmetries which the SM is based on. They are internal symmetries, which, with the additional requirement of being local (x^μ-dependent), require the introduction of gauge bosons associated with them in order to preserve the gauge invariance of the Lagrangian.

A local transformation of a Dirac field $\psi(x)$ with Lagrangian

$$\mathcal{L} = \overline{\psi}(i\partial\!\!\!/ - m)\psi \tag{2.2.7}$$

based on the symmetry $U(1)$ is introduced by the unitary operator V:

$$\psi(x) \to \psi'(x) = V\psi(x) = e^{i\alpha(x)}\psi(x), \tag{2.2.8}$$

where $\alpha(x)$ is a real parameter of the transformation. The kinetic term (and any other terms containing derivatives of the field) in the Lagrangian is no longer invariant under this transformation. In order to restore the invariance, an addition to the derivative is required[4]:

$$D_\mu\psi(x) = \partial_\mu\psi(x) + ieA_\mu\psi(x), \tag{2.2.9}$$

where A_μ is a gauge field (the connection 1-form) associated with the gauge transformation, and e is a constant for convenience, characterising the coupling between the Dirac and gauge fields. Simultaneously with Equation (2.2.8), A_μ undergoes transformations according to

$$A_\mu(x) \to A_\mu(x) - \frac{1}{e}\partial_\mu\alpha(x). \tag{2.2.10}$$

In this way, $D_\mu\psi(x)$ is ensured to transform in the same way as $\psi(x)$ does,

$$D_\mu\psi(x) \to V(D_\mu\psi(x)), \tag{2.2.11}$$

[4]Geometric derivations of the covariant derivative and the gauge field are given in Ref [22].

and it is called the covariant derivative. Interactions between the Dirac spinor ψ and the gauge field are introduced by the last term of Equation (2.2.9). In order for the gauge field to propagate, a suitable gauge invariant kinetic term must be introduced to the Lagrangian. A suitable choice is $F_{\mu\nu}F^{\mu\nu}$, with $F_{\mu\nu} = \frac{i}{e}[D_\mu, D_\nu] = \partial_\mu A_\nu - \partial_\nu A_\mu$. Terms proportional to $A_\mu A^\mu$ (e.g. a mass term for the gauge field) are forbidden, since they are not gauge invariant.

Thus, the Lagrangian which is invariant under the local transformation of Equation 2.2.8 is:

$$\mathcal{L} = -\frac{1}{4}F_{\mu\nu}F^{\mu\nu} + \overline{\psi}(i\not{D} - m)\psi, \tag{2.2.12}$$

where the Feynman slash notation, $\not{a} = \gamma_\mu a^\mu$, is used. The equations of motion (Equation (2.2.3)) for A_μ produce the inhomogeneous Maxwell equations:

$$0 = \frac{\partial\mathcal{L}}{\partial A_\mu} - \partial_\nu \frac{\partial\mathcal{L}}{\partial(\partial_\nu A_\mu)} = \partial_\nu F^{\nu\mu} - e\overline{\psi}\gamma^\mu\psi, \tag{2.2.13}$$

with the current identified as $j^\mu = e\overline{\psi}\gamma^\mu\psi$. Equation (2.2.12) is the Lagrangian of Quantum Electrodynamics (QED), describing the interactions between photons and electrically charged fermions [22].

2.2.2 Local (gauge) non-Abelian symmetries

Local non-Abelian (or Yang-Mills) symmetries result in more complicated interactions than the Abelian case described in Section 2.2.1, but follow the same prescription for building the Lagrangian. The transformations of a Dirac field as an N-plet under the local non-Abelian group $SU(N)$ are introduced by:

$$\Psi(x) \to V\Psi(x) = e^{i\alpha^i(x)t^i} \begin{pmatrix} \Psi_1 \\ \vdots \\ \vdots \\ \Psi_N \end{pmatrix}, \tag{2.2.14}$$

where $\alpha^i(x)$ are real parameters and t^i are the generators of the transformations (they are Hermitian quantities which, according to QM, correspond to observable quantities), with $i = 1, 2, ..., (N^2 - 1)$. The difference from the Abelian case is that the generators of the transformations no longer commute:

$$[t^k, t^l] = if^{klm}t^m, \tag{2.2.15}$$

where the f^{klm} are the structure constants of the group. The derivative is required to be modified to

$$D_\mu = \partial_\mu - igA^i_\mu t^i, \tag{2.2.16}$$

introducing $N^2 - 1$ gauge bosons to the theory, which undergo the transformations:

$$A^i_\mu \to A^i_\mu + \frac{1}{g}\partial_\mu a^i(x) + f^{ijk}A^j_\mu a^k(x), \tag{2.2.17}$$

where g is a constant characterising the coupling strength to the gauge fields [22]. In addition, the field strength tensor now reads $F^i_{\mu\nu} = \partial_\mu A^i_\nu - \partial_\nu A^i_\mu + g f^{ijk} A^j_\mu A^k_\nu$. The last term leads to interactions between the gauge fields of the theory. The Lagrangian which is invariant under the gauge transformation is then given by

$$\mathcal{L} = -\frac{1}{4}F^i_{\mu\nu}F^{i\ \mu\nu} - \overline{\psi}(i\not{D} - m)\psi. \tag{2.2.18}$$

2.3 The Standard Model

The interactions of the SM are described by local gauge symmetries characterised by the group product $SU(3)_C \times SU(2)_T \times U(1)_Y$, with particles categorised by their quantum numbers (charges) under these symmetries. The subscripts indicate the "spaces" in which the symmetries operate. $SU(3)_C$ is the group connected to the theory of strong interactions, Quantum Chromodynamics (QCD), where C refers to colour - the quantum number associated with the group. $SU(2)_T$ describes the weak interaction which acts on left-handed spinors with weak isospin (T) charges, and $U(1)_Y$ refers to the Abelian symmetry with the hypercharge (Y) quantum number. The matter (fermion) fields are divided into two groups of 3 families each - those which possess the colour charge (quarks) and those which do not (leptons).

2.3.1 Quantum chromodynamics

The theory of QCD [23] describes the strong interaction through the non-Abelian group $SU(3)_C$. The 8 generators of the gauge transformation, the Gell-Mann matrices, act in colour space (red, green, blue, not associated with the colour of the electromagnetic spectrum) with the Dirac spinors, $\Psi = (\Psi_r, \Psi_g, \Psi_b)^T$. There are 8 corresponding massless gauge bosons, the gluons, which serve as the interaction mediators. Since the theory is non-Abelian, the gluons themselves carry the colour charge of the interaction, leading to triple and quadruple gluon vertices. Colour is a conserved quantity and the bound states of QCD are required to be colourless. They are referred to as hadrons and the ones discovered are divided into states containing two (mesons), three (baryons), four (tetraquarks [24]) or five (pentaquarks [25]) valence quarks.

Compared to the coupling strength of QED, $\alpha = e^2/4\pi \sim 1/137$, the QCD analogue is "strong" - $\alpha_s = g_s^2/4\pi \sim 1$. In addition, the two coupling strengths differ in their dependence on the energy scale of the process, Q^2, due to the

Particle	Symbol	Colour charge	Weak isospin (T_3)	EM charge (Q) [e]	mass [MeV]
Fermions (spin 1/2)					
Quarks					
up	u	yes	1/2	2/3	~ 2.16
down	d	yes	-1/2	-1/3	~ 4.6
charm	c	yes	1/2	2/3	$\sim 1.27 \times 10^3$
strange	s	yes	-1/2	-1/3	~ 93
top	t	yes	1/2	2/3	$\sim 173 \times 10^3$
bottom	b	yes	-1/2	-1/3	$\sim 4.2 \times 10^3$
Leptons					
neutrino one	ν_1	no	1/2	0	$< 1.1 \times 10^{-3}$
electron	e	no	-1/2	-1	~ 0.51
neutrino two	ν_2	no	1/2	0	< 0.19
muon	e	no	-1/2	-1	~ 105.7
neutrino three	ν_3	no	1/2	0	< 18.2
tau	e	no	-1/2	-1	1.8×10^3
Bosons (spin 1)					
photon	γ	no	0	0	0
W bosons	$W^{\pm}$	no	± 1	± 1	$\sim 80.4 \times 10^3$
Z boson	Z^0	no	0	0	$\sim 91 \times 10^3$
gluon	g	yes($\times 2$)	0	0	0
Bosons (spin 0)					
Higgs	H^0	no	1/2	0	$\sim 125 \times 10^3$

Table 2.1: The SM particles with their quantum numbers. Fermions are divided into three generations by horizontal lines. The weak isospin numbers are given for the left-hand chirality component of fermions, while for the right-handed, it is $T_3 = 0$. The weak hypercharge Y is connected with Q and T_3 through $Y = 2(Q - T_3)$. Data was taken from Ref. [9].

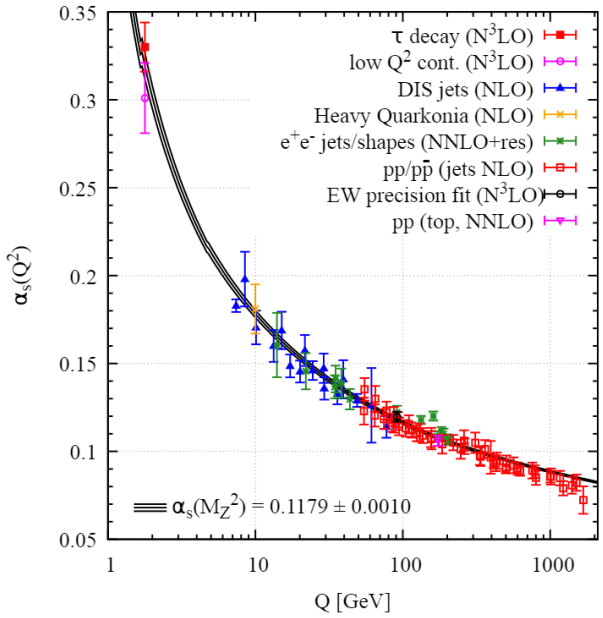

Figure 2.2: Measurements of the QCD coupling strength α_s at different energy scales Q. Taken from Ref. [9].

non-Abelian nature of QCD. The evolution (or "running") of the coupling strength with the energy scale is governed by its β function, which in the case of α_s is given to first order by the expression

$$Q^2 \frac{\partial \alpha_s}{\partial Q^2} = \beta(\alpha_s) = -(11 - \frac{2n_f}{3}) \frac{\alpha_s^2}{4\pi} + \mathcal{O}(\alpha_s^3), \tag{2.3.1}$$

where n_f is the number of quark flavours which couple to the effective theory ($m_q \ll Q$). In contrast, the QED coupling strength evolves as

$$\beta(\alpha) = \frac{\alpha^2}{3\pi} + \mathcal{O}(\alpha^3). \tag{2.3.2}$$

This results in α increasing as the momentum transfer increases (or equivalently as distances decrease), while α_s has the opposite effect, $\alpha_s \xrightarrow{Q \to \infty} 0$, Figure 2.2.

One of the consequences of the running of α_s is asymptotic freedom [26] - this causes quarks inside a hadron, when probed at high energies, to experience feeble coupling, allowing them to be treated as quasi-free particles when probed at large energies ($Q \gg \Lambda_{QCD} \sim 200$ MeV). This allows for perturbation theory to be used, enabling the calculation of relevant hard scattering cross-sections. On the other end of the spectrum, the running of α_s leads to colour confinement [27, 28]. Quarks bound into a hadron experience increasingly strong coupling as they are pulled farther apart. When the system overcomes a threshold energy, a quark antiquark ($q\bar{q}$) pair is produced and forms new hadrons together

with the initial quarks, making the isolation of single quarks outside hadrons impossible. Any coloured states created at a scattering experiment undergo hadronisation through the creation of such quark pairs, resulting in a collection (shower) of colourless states propagating in the direction of the initial quarks.

2.3.2 Glashow-Weinberg-Salam theory of the electroweak interaction

The theory of electroweak interactions was developed by Glashow, Weinberg and Salam [29–31]. It involves the gauge group $SU(2)_T \times U(1)_Y$, with corresponding gauge fields W^i_μ, $i = 1, 2, 3$, and B_μ. The interactions with fermions are introduced through the covariant derivative of the form:

$$D_\mu = \partial_\mu + igW^i_\mu t^i + ig'YB_\mu, \tag{2.3.3}$$

where g and g' are coupling constants and t^i are the generators of $SU(2)_T$. A Dirac field ψ can be split into left-handed and right-handed fields using the chirality projection operators, $P_L = \frac{1}{2}(1 - \gamma^5)$, $P_R = \frac{1}{2}(1 + \gamma^5)$:

$$\psi = \psi_L + \psi_R = P_L\psi + P_R\psi \tag{2.3.4}$$

$$\overline{\psi} = \overline{\psi}_L + \overline{\psi}_R = \overline{\psi}P_R + \overline{\psi}P_L. \tag{2.3.5}$$

The kinetic term of a Dirac field is decomposed into separate components:

$$\overline{\psi}i\not{D}\psi = \overline{\psi}_L i\not{D}\psi_L + \cancelto{0}{\overline{\psi}_L i\not{D}\psi_R} + \cancelto{0}{\overline{\psi}_R i\not{D}\psi_L} + \overline{\psi}_R i\not{D}\psi_R, \tag{2.3.6}$$

thus decoupling the interactions involving the left- and right-handed chiralities with bosons arising from gauge symmetries. The terms can be assigned to different representations of the gauge group, so the left-handed and right-handed component coupling to the gauge fields could in general be different. Experiments (the first one being Wu et al. [20]) show that charged current weak interactions violate parity maximally (they are of the $V - A$ form, i.e. the current is proportional to $\gamma^\mu(1-\gamma^5)$). Since the gauge bosons of $SU(2)_T$ couple only to the left-handed particles (and right-handed antiparticles), only they carry a non-zero weak isospin quantum number and are arranged in doublets in the flavour basis, while right-handed fields form singlets:

$$L^i_L = \begin{pmatrix} \nu^i \\ \ell^i \end{pmatrix}_L, Q^i_L = \begin{pmatrix} u^i \\ d^i \end{pmatrix}_L, \ell^i_R, u^i_R, d^i_R, \tag{2.3.7}$$

where $i = 1, 2, 3$ is the generation index and $\ell = e, \mu, \tau$[5]. As a result, the usual mass term in the Lagrangian which mixes the left- and right-handed fields:

$$m\overline{\psi}\psi = m(\overline{\psi}_L\psi_R + \cancelto{0}{\overline{\psi}_L\psi_L} + \cancelto{0}{\overline{\psi}_R\psi_R} + \overline{\psi}_R\psi_L) = m(\overline{\psi}_L\psi_R + \overline{\psi}_R\psi_L), \quad (2.3.8)$$

is no longer gauge invariant and is thus forbidden. However, experiments indicate that the bosons responsible for the interaction, as well as the fermions, are massive (Table 2.1), which breaks the gauge invariance.

The mass problem connected to the fermions and gauge bosons is remedied by the introduction of a complex scalar $SU(2)_T$ doublet to the theory with $T_3 = -1/2$ and $Y = 1$, the Higgs boson:

$$\Phi = \begin{pmatrix} \phi^+ \\ \phi^0 \end{pmatrix} = \frac{1}{\sqrt{2}} \begin{pmatrix} \phi_1 + i\phi_2 \\ \phi_3 + i\phi_4 \end{pmatrix}. \quad (2.3.9)$$

The most general renormalisable Lagrangian contains the following terms involving the scalar field:

$$\mathcal{L} \ni |(\partial^\mu + igW^{i\mu}t^i + ig'B^\mu)\Phi|^2 - \mu^2\Phi^\dagger\Phi + \lambda(\Phi^\dagger\Phi)^2 + \mathcal{L}_{\text{Yukawa}}, \quad (2.3.10)$$

where $\mathcal{L}_{\text{Yukawa}}$ contains the Higgs-fermion interactions. If the coefficients satisfy the requirements $\lambda > 0$ and $\mu^2 > 0$, the field potential term of the Lagrangian will have a family of related non-zero minima, or vacuum expectation values (VEV) which are at $|\Phi| = \mu/\sqrt{2\lambda} = v/\sqrt{2}$. This VEV is not invariant under $SU(2)_T \times U(1)_Y$ and thus spontaneously breaks the symmetry. The field can be expanded in the unitary gauge as

$$\Phi = \frac{1}{\sqrt{2}} \begin{pmatrix} 0 \\ v + H(x) \end{pmatrix}, \quad (2.3.11)$$

where v is a constant and the massless Goldstone fields are rotated away. To preserve electric charge, only the neutral component of the Higgs doublet can acquire a VEV, and the EM symmetry is not broken by the VEV. The covariant derivative acting on this field yields:

$$D_\mu\Phi = \begin{pmatrix} \partial_\mu + i(g'B_\mu + gW_\mu^3) & ig(W_\mu^1 - iW_\mu^2) \\ ig(W_\mu^1 + W_\mu^2) & \partial_\mu + i(g'B_\mu - gW_\mu^3) \end{pmatrix} \frac{1}{\sqrt{2}} \begin{pmatrix} 0 \\ v + H(x) \end{pmatrix}, \quad (2.3.12)$$

giving rise to interaction terms between the gauge bosons and H, as well as mass terms for the gauge bosons. By identifying the charged and neutral weak

[5]Right-handed neutrinos do not participate in any interactions in the SM and are thus not included.

interaction bosons as:

$$W_\mu^\pm = \frac{1}{\sqrt{2}}(W_\mu^1 \mp iW_\mu^2) \tag{2.3.13}$$

$$Z_\mu = \frac{1}{\sqrt{g^2+g'^2}}(gW_\mu^3 - g'B_\mu), \tag{2.3.14}$$

their masses (to first order) are extracted to be

$$m_W = \frac{v}{2}g \tag{2.3.15}$$

$$m_Z = \frac{v}{4}\sqrt{g^2+g'^2}. \tag{2.3.16}$$

The photon is identified as the orthogonal state to the Z boson with no mass term (corresponding to the unbroken symmetry of the combination of T_3 and Y transformations):

$$A_\mu = \frac{1}{\sqrt{g^2+g'^2}}(gW_\mu^3 + g'B_\mu). \tag{2.3.17}$$

After the Higgs field obtains its VEV, the Yukawa interaction

$$\mathcal{L}^q_{\text{Yukawa}} = -Y^d_{ij}\overline{Q^I_{Li}}\Phi d^I_{Rj} - Y^u_{ij}\overline{Q^I_{Li}}\epsilon\Phi^* u^I_R + h.c. \tag{2.3.18}$$

generates masses for the quarks and their couplings to H:

$$\mathcal{L}^q_{\text{Yukawa}} = -\frac{(v+H)}{\sqrt{2}}(Y^d_{ij}\overline{d}^I_{Li}d^I_{Rj} + Y^u_{ij}\overline{u}^I_{Li}u^I_{Rj} + h.c.), \tag{2.3.19}$$

where $h.c.$ stands for Hermitian conjugate. In general, the two Y_{ij} are arbitrary and non-diagonal. The physical (mass) eigenstates are acquired after diagonalising them by introducing four unitary matrices. As an example, the masses of the up-type quarks are given by:

$$M^u = V^u_L Y^u V^{u\dagger}_R \frac{v}{\sqrt{2}}, \tag{2.3.20}$$

which gives the relations between the mass eigenstates on the left and the weak interaction eigenstates on the right. Making the substitution and working with the mass eigenstates for the quarks, the kinetic terms, neutral currents and electric currents remain in the same form, but the charged current weak interaction (CCWI) for the quarks now reads:

$$\mathcal{L}_{CC} = -\frac{g}{\sqrt{2}}(\overline{\mathcal{U}}_L\gamma^\mu W^+_\mu V_{CKM}\mathcal{D}_L + h.c.), \tag{2.3.21}$$

where the Cabibbo-Kobayashi-Maskawa matrix is defined as $V_{CKM} = V_L^{u\dagger} V_L^d$, $\overline{\mathcal{U}}_L = (\overline{u_L}, \overline{c_L}, \overline{c_L})$ and $\mathcal{D}_L = (d_L, s_L, b_L)^T$. As only the left-handed particles interact through the CCWI, the right-handed equivalent of this matrix is not observed. It is customary to write the matrix with each row representing the interaction of each up-type quark in the mass basis:

$$|V_{CKM}| = \begin{pmatrix} |V_{ud}| & |V_{us}| & |V_{ub}| \\ |V_{cd}| & |V_{cs}| & |V_{cb}| \\ |V_{td}| & |V_{ts}| & |V_{tb}| \end{pmatrix} \sim \begin{pmatrix} 0.97 & 0.227 & 0.0036 \\ 0.227 & 0.97 & 0.04 \\ 0.0085 & 0.04 & 1 \end{pmatrix}. \quad (2.3.22)$$

The charged leptons also acquire their masses through the Yukawa interaction similar to Equation (2.3.18):

$$\mathcal{L}^l_{\text{Yukawa}} = -Y^l_{ij} \overline{L^I_{Li}} \Phi e^I_{Rj}, \quad (2.3.23)$$

while the neturinos remain massless. However, observed neutrino oscillations require neutrinos to have non-zero masses, thus extending the SM by multiple different possible mechanisms for neutrino mass generation. Like in the case of quarks, the neutrino mass eigenstates (commonly labeled as ν_1, ν_2, ν_3) are a mixture of their weak interaction eigenstates (ν_e, ν_μ, ν_τ):

$$\begin{pmatrix} \nu_e \\ \nu_\mu \\ \nu_\tau \end{pmatrix} = V_{\text{PMNS}} \begin{pmatrix} \nu_1 \\ \nu_2 \\ \nu_3 \end{pmatrix}, \quad (2.3.24)$$

where the Pontecorvo-Maki-Nakagawa-Sakata (PMNS) matrix V_{PMNS} is the lepton sector equivalent of V_{CKM} - a unitary matrix with 4 independent parameters, one of which allows for $\mathcal{CP}$ violation. A comparison between the magnitudes of the measured elements is shown in Figure 2.3. A hierarchy in the magnitudes of the matrix elements in the quark sector can be observed, while such is absent in the lepton sector.

As a 3×3 unitary matrix, V_{CKM} has 9 independent parameters. Since phase changes to the quarks are possible as they do not change the kinetic or mass terms in the Lagrangian, 5 of those parameters (the relative quark phases) can be removed, resulting in 4 independent parameters. One of the most common parameterisations of V_{CKM} is a decomposition into three plane rotations and a phase change:

$$\begin{pmatrix} 1 & 0 & 0 \\ 0 & \cos\theta_{23} & \sin\theta_{23} \\ 0 & -\sin\theta_{23} & \cos\theta_{23} \end{pmatrix} \begin{pmatrix} \cos\theta_{13} & 0 & e^{-i\delta}\sin\theta_{13} \\ 0 & 1 & 0 \\ -e^{i\delta}\sin\theta_{13} & 0 & \cos\theta_{13} \end{pmatrix} \begin{pmatrix} \cos\theta_{12} & \sin\theta_{12} & 0 \\ -\sin\theta_{12} & \cos\theta_{12} & 0 \\ 0 & 0 & 1 \end{pmatrix},$$

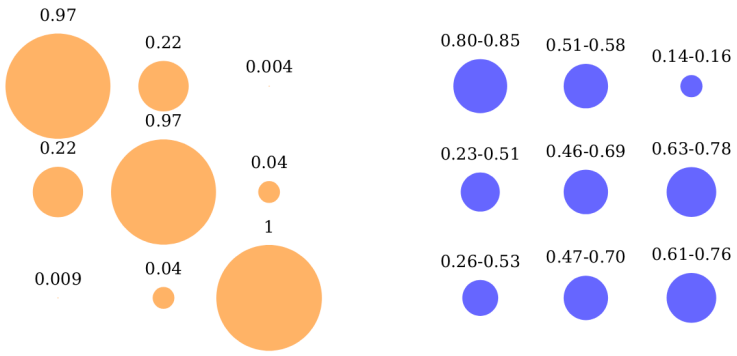

Figure 2.3: A comparison between the CKM quark and the PMNS neutrino mixing matrices. The areas of the circles represent the absolute magnitudes of the corresponding elements.

where δ is the CP violating phase. Another commonly used parameterisation is the Wolfenstein parameterisation, displaying the hierarchy of the elements as different powers of the parameter λ:

$$\begin{pmatrix} 1-\frac{\lambda^2}{2} & \lambda & A\lambda^3(\rho-i\eta) \\ -\lambda & 1-\frac{\lambda^2}{2} & A\lambda^2 \\ A\lambda^3(1-\rho-i\eta) & A\lambda^2 & 1 \end{pmatrix} + \mathcal{O}(\lambda^4), \tag{2.3.25}$$

with the relationships between the two parameterisations given by [9]

$$\sin\theta_{12} = \lambda = \frac{|V_{us}|}{\sqrt{|V_{ud}|^2 + |V_{us}|^2}}, \tag{2.3.26}$$

$$\sin\theta_{23} = A\lambda^2 = \lambda\frac{|V_{cb}|}{|V_{us}|}, \tag{2.3.27}$$

$$e^{i\delta}\sin\theta_{13} = V_{ub}^* = A\lambda^3(\rho - i\eta) = \frac{A\lambda^3(\overline{\rho}+i\overline{\eta})\sqrt{1-A^2\lambda^4}}{\sqrt{1-\lambda^2}(1-A^2\lambda^4(\overline{\rho}+i\overline{\eta}))}. \tag{2.3.28}$$

The unitarity constraints are $V_{ij}V_{ik}^* = \delta_{jk}$ and $V_{ji}V_{ki}^* = \delta_{jk}$, where the indices denote the quark generations. The six cases for which $j \neq k$ can be depicted as triangles in the complex plane. The most commonly used one (ofter referred to as the unitarity triangle) is given by the relation $V_{i1}V_{i3}^* = 0$, which, due to the definitions of $\overline{\rho}$ and $\overline{\eta}$ in Equation (2.3.28), can be rescaled, with vertices at $(0,0)$, (1,0) and $(\overline{\rho},\overline{\eta})$. The angles of the triangle are given by:

$$\beta = arg\Big(-\frac{V_{cd}V_{cb}^*}{V_{td}V_{tb}^*}\Big), \tag{2.3.29}$$

$$\alpha = arg\Big(-\frac{V_{td}V_{tb}^*}{V_{ud}V_{ub}^*}\Big), \tag{2.3.30}$$

$$\gamma = arg\Big(- \frac{V_{ud}V_{ub}^*}{V_{cd}V_{cb}^*}\Big). \tag{2.3.31}$$

The constraints in the unitarity triangle plane imposed by measurements are shown in Figure 2.4 [9].

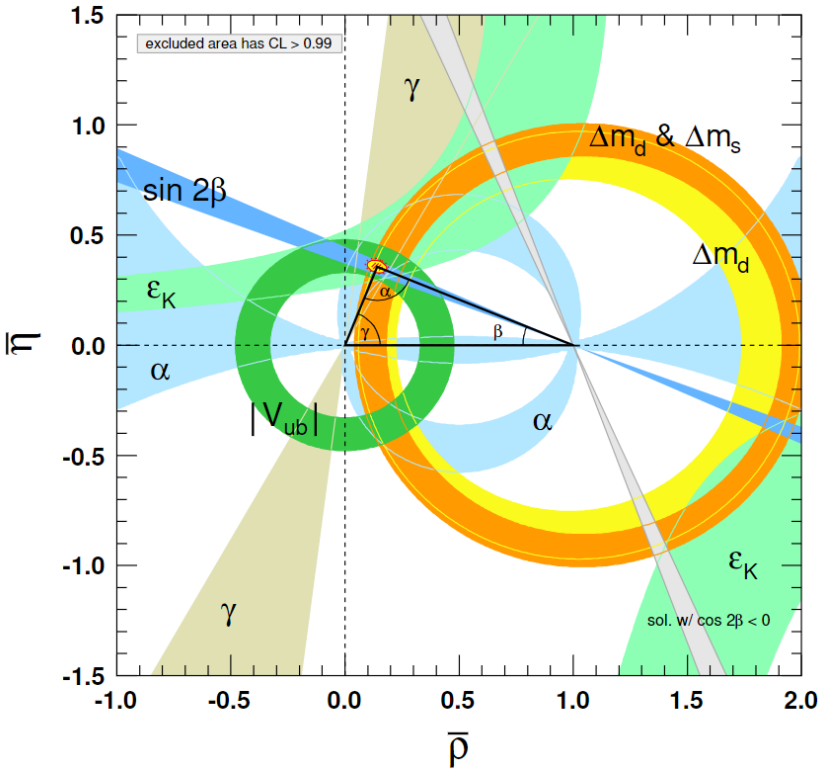

Figure 2.4: Constraints on the CKM unitarity triangle. Taken from Ref. [9].

Renormalisation group studies of the CKM matrix [13] have shown that only the Wolfenstein parameter A evolves significantly with energy between the electroweak $\sim \mathcal{O}(10^2)$ GeV and grand unified theories (GUT) $\sim \mathcal{O}(10^{15})$ GeV scales.

Including lepton mixing, the weak interaction is connected to 22 out of 26 free parameters of the SM (Table 2.2), which can be determined only from experiment.

2.4 Physics at the Large Hadron Collider

This section summarises a set of concepts relevant to particle collider experiments and to the Large Hadron Collider (LHC) in particular.

2.4.1 Luminosity

The luminosity L of a particle accelerator relates the number of observed collision events N_{process} of a given process over time T and the total cross-

Symbol	Parameter
Electroweak interaction sector	
g	coupling strength to the $SU_T(2)$ gauge bosons
g'	coupling strength to the $U_Y(1)$ gauge boson
$\theta_{12}, \theta_{13}, \theta_{23}, \delta$	4 CKM matrix parameters
$\theta_{12}, \theta_{13}, \theta_{23}, \delta$	4 PMNS matrix parameters
m_i	6 quark and 6 lepton masses
Strong interaction sector	
g_s	coupling strength to the $SU_C(3)$ gauge bosons
θ_{QCD}	$SU_C(3)$ $\mathcal{CP}$ phase
Higgs sector	
v	vacuum expectation value of the Higgs field
λ	Higgs field quartic self-coupling

Table 2.2: Free parameters of the Standard Model. The choice of free parameters is not unique, for example one can choose the Yukawa couplings instead of the quark masses. θ_{QCD} is an allowed strong interaction Lagrangian term, $\theta_{QCD}\epsilon^{\mu\nu\sigma\rho}G^a_{\mu\nu}G^a_{\sigma\rho}$, which violates $\mathcal{P}$ and $\mathcal{T}$ symmetries [32].

section σ_{process} for the process to occur:

$$N_{\text{process}} = \sigma_{\text{process}} L = \sigma_{\text{process}} \int^{T} L(t)dt, \tag{2.4.1}$$

where $L(t)$ is the instantaneous luminosity. In circular particle collider experiments, like the LHC, with head-on colliding bunches of particles with Gaussian profiles and travelling at speed $\sim c$, the luminosity can be derived from the expression:

$$L = \frac{N_1 N_2 f_{rev} n_b}{4\pi\sigma_x\sigma_y}\mathcal{F}. \tag{2.4.2}$$

In the case where the beams in the collision are identical, the above expression simplifies to

$$L = \frac{N^2 f_{rev} n_b}{4\pi\sigma^2}\mathcal{F}, \tag{2.4.3}$$

where N is the number of particles in the colliding bunches, f_{rev} is the revolution frequency (for the LHC circumference of ~ 27 km, $f_{rev} = 11245$ Hz), n_b is the number of particle bunches per beam, σ is the transverse size of the beams in the interaction point (IP) and $\mathcal{F}$ is a correction factor. The transverse sizes σ can also be expressed via the transverse emmitance ϵ, the relativistic γ factor and the β-function[6] at the IP, β^*, as $\sigma = \sqrt{\epsilon\beta^*\gamma^{-1}}$. Contributions to $\mathcal{F}$ arise from effects including non-zero crossing angle of the beams, deviation from Gaussian beam profiles, dependence of β on distance from the IP, resulting in modified transverse distributions [33, 34].

[6]Not related to the β-function which governs the evolution of physical parameters with energy scale.

The designed LHC peak instantaneous luminosity was 10^{34} cm^{-2}s^{-1} [35], which was reached and almost doubled during Run 2. The bunch spacing in the proton beams is 25 ns, with ~ 2500 bunches of $\sim 10^{11}$ protons per beam [36].

2.4.2 Parton distribution functions

As a QCD bound state, the proton consists of three valence quarks (uud) and a "sea" of quark-anti-quark pairs and gluons, collectively referred to as partons. Each parton i carries a different fraction x_i (also known as Bjorken x) of the hadron's four-momentum P^μ, $p_i^\mu = x_i P^\mu$, where the transverse components can be neglected in high energy collisions [37]. In such collisions, x_i would be different on an event-by-event basis for each parton, but they are expected to follow statistical distributions $f_i(x, \mu_F)$, known as parton distribution functions (PDFs). The parameter μ_F represents the factorisation scale at which the hadron is probed. As these functions are used to estimate the long-range QCD (non-perturbative) effects due to colour confinement, they cannot be calculated. However, they obey a renormalisation group equation (the DGLAP equation [38–40][7]) governing their evolution with respect to μ_F. As a result, different measurements (like deep inelastic scattering and Drell-Yan processes) are used to derive the PDFs at different x and μ_F, which can then be evolved with respect to μ_F. At low energies ($Q = \mu_F \sim 2$ GeV), the probed partons are the valence quarks, with the gluon and sea quark contribution increasing as the energy increases, Figure 2.5. The general formula for a hard scattering cross-section of two hadrons H_1 and H_2 into a final state X is given following the factorisation theorem [42] as:

$$\sigma_{H_1 H_2 \to X} = \sum_{i,j} \int_0^1 dx_i f_i^{H_1}(x_i, \mu_F) \int_0^1 dx_j f_j^{H_2}(x_j, \mu_F) \times \hat{\sigma}_{ij \to X}(\mu_F, \mu_R), \tag{2.4.4}$$

where the sum runs over all types of partons i, j in the hadrons. The long-range effects are handled by the initial state PDFs $f_i^{H_1}$ and $f_j^{H_2}$, while $\hat{\sigma}_{ij \to X}$ is the cross-section derived to any order in perturbation theory, which only depends on the partons involved in the hard scatter. The parameter μ_R is the renormalisation scale.

2.4.3 The top quark and its production at the LHC

With mass $m_t \sim 173$ GeV, the top quark is the only fermion with Yukawa coupling to the Higgs boson of $\mathcal{O}(1)$ and it is a major contributor in loop correction calculations. It is the only fermion which is massive enough to decay

[7] Named after Dokshitzer, Gribov, Lipatov, Altarelli and Parisi.

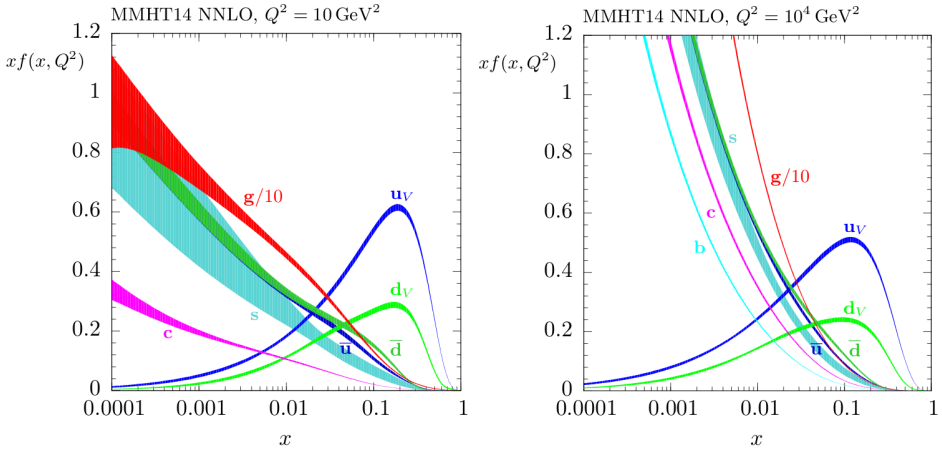

Figure 2.5: MMHT2014 NNLO x times the unpolarised proton PDFs $f(x)$ at $Q^2 = \mu_F^2 = 10$ GeV^2 (left) and $Q^2 = \mu_F^2 = 10^4$ GeV^2 (right). The subscript V denotes the valence quarks. The distributions for $\bar{b}$, $\bar{c}$, $\bar{s}$ are the same as the ones for b, c and s respectively. The bands represent the 68% confidence-level regions. Taken from Ref. [41].

into an on-shell W boson. The timescale of this decay ($\sim 10^{-25}$ s) is short enough that the top quark does not undergo hadronisation, the timescale of which can be estimated by the inverse of the QCD energy scale, $1/\Lambda_{QCD} \sim 10^{-24}$ s. As a result, the top quark does not form a QCD bound state before decaying, making it possible to extract kinematic information about the "bare" quark directly from its decay products [43].

At the LHC, the dominant production of top quarks is in $t\bar{t}$ pairs, Figure 2.6, with $\sim 90\%$ of the events being produced through gluon fusion and $\sim 10\%$ in $q\bar{q}$ annihilation at $\sqrt{s} = 13$ TeV. Since the predominant decay channel for

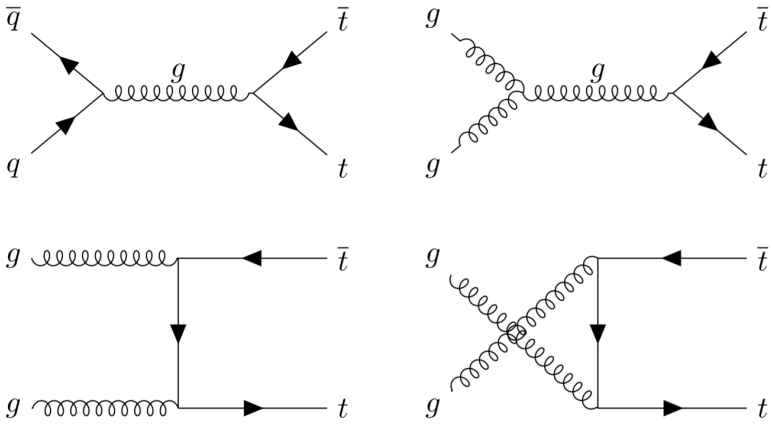

Figure 2.6: The leading order Feynman diagrams of $t\bar{t}$ production at the LHC. Top left represents $q\bar{q}$ annihilation, while the rest represent gluon fusion.

the top quarks is $t \to Wb$ with decay rate $\sim 1(\propto |V_{tb}|^2)$, the $t\bar{t}$ decay modes are divided according to the decay products of the two W bosons, which could

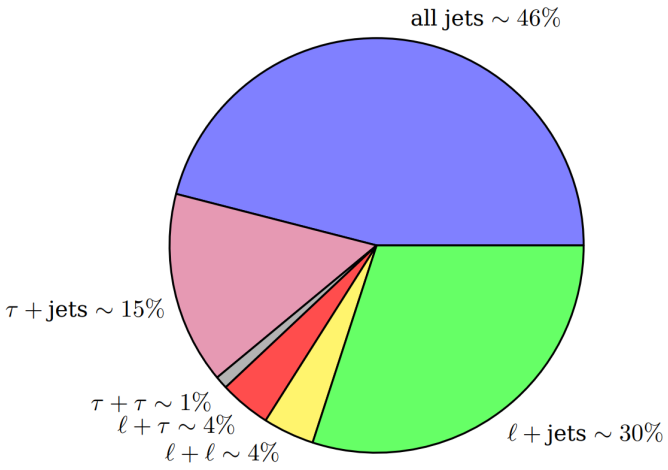

Figure 2.7: Branching fractions of the different $t\bar{t}$ decay modes, $\ell = e, \mu$.

be either τ, $\ell(e, \mu)$ or quarks. The branching fractions of the different decay modes of the $t\bar{t}$ system are summarised in Figure 2.7.

Measurements of the total $t\bar{t}$ cross-section from both Compact Muon Spectrometer (CMS) and ATLAS are shown in Figure 2.8. The different decay modes lead to separate topologies, resulting in differences in available statistics and in analysis uncertainties.

In addition to top pair production, processes with different final states containing a single top quark take place. The tree level Feynman diagrams for these processes, collectively referred to as single top production, are shown in Figure 2.9. Despite these processes resulting in different detector signatures than the semi-leptonic $t\bar{t}$ decay, they can still satisfy the selection requirements if additional jets (due to pile-up, defined in Section 3.4) are present.

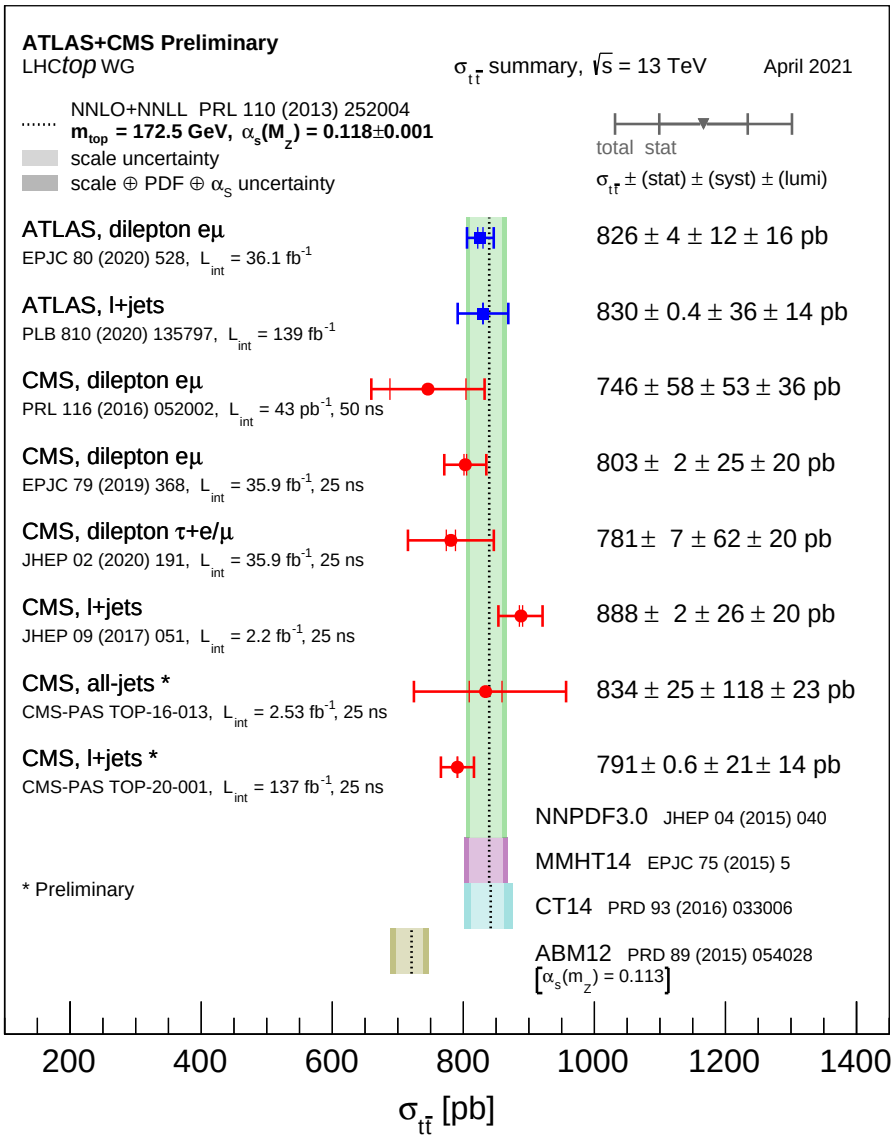

Figure 2.8: Total $t\bar{t}$ cross-section measured by the ATLAS and CMS collaborations in the dilepton and single lepton channels at $\sqrt{s} = 13$ TeV compared to the exact NNLO QCD calculation complemented with NNLL resummation (top++2.0). The theory uncertainties stem from renormalisation and factorisation scales, PDFs and the strong coupling. Taken from Ref. [44].

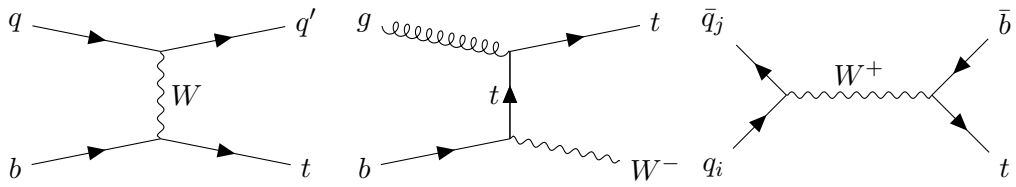

Figure 2.9: Tree level Feynman diagrams of single top processes - t-channel (left), Wt (centre), s-channel (right).

Chapter 3

Experimental setup

3.1 The Large Hadron Collider

The European Organisation for Nuclear Research (CERN) (from French - Conseil européen pour la recherche nucléaire) was established in 1954 and is the largest particle physics research laboratory in the world, situated near Geneva, Switzerland. The main goal of CERN and the many experiments it has hosted throughout the years is the study of the constituents of matter and their interactions. A schematic view of the CERN accelerator complex is shown in Figure 3.1.

The most powerful particle accelerator in the world to date, Large Hadron Collider (LHC) [35], is situated at CERN. It was installed in the same circular tunnel that housed the Large Electron-Positron collider (LEP), but instead of colliding e^+e^-, it was designed for proton-proton collisions, pp[1]. The protons are produced and accelerated in a series of repurposed accelerators before being injected into the LHC ring, Figure 3.1. First, electrons are stripped from hydrogen atoms by an electric field, with the resulting nuclei (protons) being sent to the Linear Accelerator 2 (Linac 2) [46], where they are accelerated up to 50 MeV. They are then transferred into the Proton Synchrotron Booster - reaching 1.4 GeV, the Proton Synchrotron - 25 GeV, and to the Super Proton Synchrotron, where the beam reaches the energy of 450 GeV. The protons are then split into two beams entering their own vacuum pipe where they travel in opposite directions around the LHC ring. In order to bend the beam along the LHC pipes, a collection of more than 1200 superconducting dipole magnets generating a magnetic field of 8.3 T and requiring temperatures of 1.9 K are used. In addition, 392 quadrupole magnets are used to focus the beam, with higher multipoles being used for magnetic field corrections [47]. In the end, the proton beams reach the energy of 6.5 TeV, separated into bunches

[1]Some special runs also take place involving lead nuclei - proton-lead (pPb), and lead-lead collisions ($PbPb$).

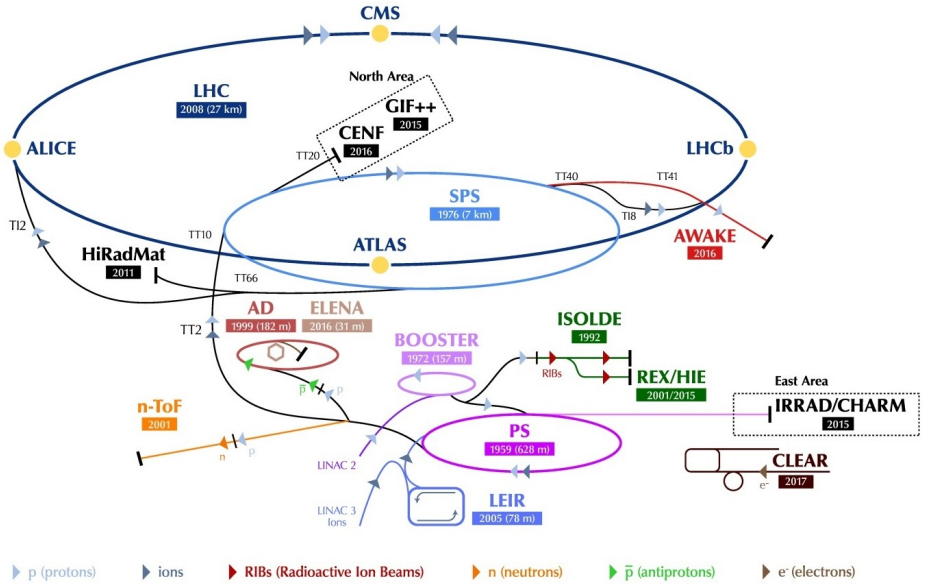

Figure 3.1: The CERN accelerator complex. SPS - Super Proton Synchrotron, PS - Proton Synchrotron, ELENA - Extra Low ENergy Antiproton ring, AD - Antiproton Decelerator, CLEAR - CERN Linear Electron Accelerator for Research, AWAKE - Advanced WAKefield Experiment, ISOLDE - Isotrope Separator OnLine, REX/HIE - Radioactive EXperiment/High Intensity and Energy ISOLDE, LEIR - Low Energy Ion Ring, LINAC - LINear ACcelerator, n-ToF - Neutrinos Time Of Flight, HiRadMat - High-Radiation to Materials, CHARM - CERN High Energy AcceleRator Mixed field facility, IRRAD - proton IRRADiation facility, GIF++ - Gamma Irradiation Facility, CENF - CERN Neutrino platForm. Taken from Ref. [45].

of $\sim 1.1 \times 10^{11}$ protons and bunch spacing of 25 ns [48]. The proton bunches are then made to collide at 4 different points, around which the main LHC experiments - ATLAS [49], Compact Muon Spectrometer (CMS) [50], A Large Ion Collider Experiment (ALICE) [51], Large Hadron Collider beauty (LHCb) [52] - are set-up.

The operation of the LHC consists of periods of data taking, or Runs, followed by long shutdowns (LSs), during which upgrades to the LHC and its detectors are carried out in preparation for the following Run. After Run 3, a transition to a stage with increased luminosity ($5 - 7.5 \times 10^{34}$ cm^{-2}s^{-1}) and $\sqrt{s} = 14$ TeV, the High Luminosity Large Hadron Collider (HL-LHC), is planned. The aim of the programme is to reach an integrated luminosity of 3000 fb^{-1} (4000 fb^{-1} if the machine is exploited to its maximum potential) during the first $\sim$ 12 years of HL-LHC operation [53]. In preparation for this transition, major upgrades of the LHC and replacement of experiment subdetectors are scheduled to take place during LS3 in order to allow operation under the resulting harsher conditions. A timeline of past and planned LHC operational periods is shown in Figure 3.2.

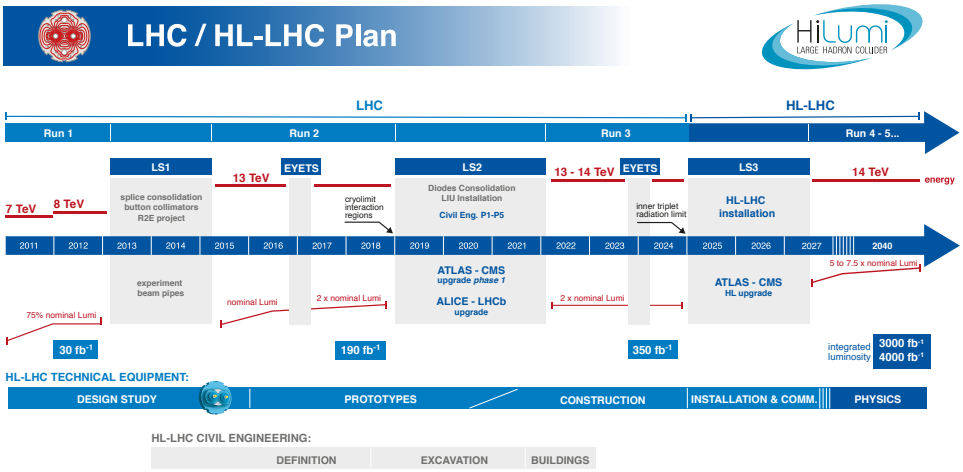

Figure 3.2: Timeline of past and planned LHC operation periods. EYETS periods represent Extended Year-End Technical Stops. Taken from Ref. [54]. An enlarged version of the figure is available in Figure A.1 of the Appendix A.1.

The analysis presented in this thesis uses Monte Carlo (MC) generated events corresponding to the complete dataset collected by the ATLAS experiment during Run 2 of the LHC, equivalent to the integrated luminosity of ~ 139 fb^{-1}.

3.2 The ATLAS experiment

The ATLAS detector is situated at collision Point-1 of the LHC. As a general purpose detector, it was designed to identify and measure all particles (apart from the neutrinos, which escape the detector without interacting with it) within the Standard Model and potentially Beyond the Standard Model (BSM) produced in hadron collisions at the TeV scale. Since these particles take part in different interactions as they propagate away from the interaction point (IP), a number of specialised subdetectors are positioned around the IP and employed to distinguish specific particles. These subdetectors are arranged in an onion shell-like configuration and include, starting from the IP outwards - a tracking system (Inner Detector (ID)), a calorimetry system (Electromagnetic Calorimeter (ECal) and Hadronic Calorimeter (HCal)), and a Muon Spectrometer (MS) - with each system surrounding the previous, as shown in Figure 3.3.

The ATLAS detector has cylindrical geometry, with the beamline going through the central axis of the cylinder. The curved cylindrical surface of the detector is referred to as the "barrel", while the disks forming the circular

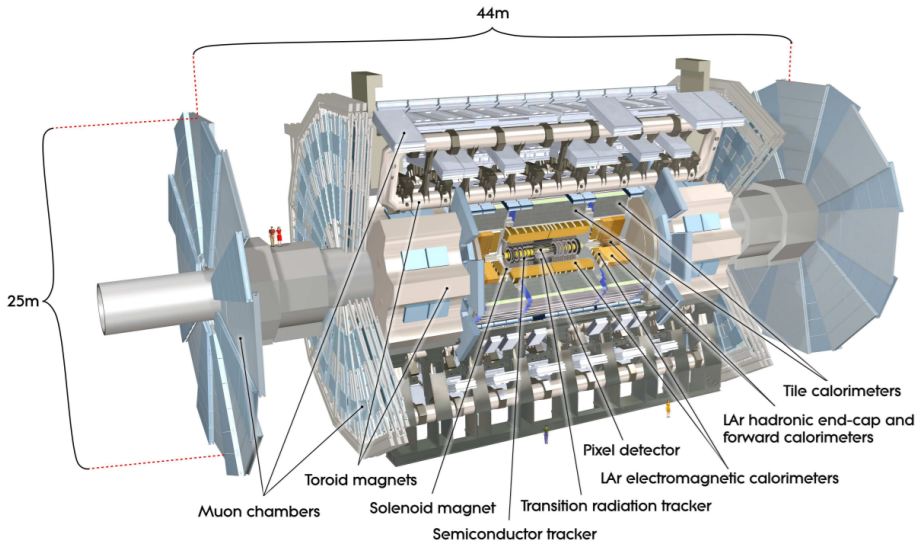

Figure 3.3: Cut-away schematic view of the ATLAS detector with its dimensions and subcomponents. Taken from Ref. [49].

surfaces in the forward regions are referred to as "end caps". A right-handed Cartesian coordinate system is employed, with the origin at the nominal IP at the centre of the detector, the x-axis pointing towards the centre of the LHC ring, the y-axis pointing vertically upwards towards Earth's surface, and the z-axis aligned with the beamline. Alternatively, cylindrical coordinates are also used, with the azimuthal angle $\phi = 0$ along the x-axis, and the polar angle $\theta = 0$ along the z-axis. Since θ is not a Lorentz invariant quantity, the rapidity H is used, defined as:

$$H = \frac{1}{2} ln \left(\frac{E + p_z}{E - p_z} \right), \tag{3.2.1}$$

where E is the energy of a particle with momentum p_z along the z-axis. Differences in rapidity are Lorentz invariant quantities, and in the case of highly relativistic particles, the rapidity H can be approximated by the pseudorapidity, which is connected to θ through:

$$H \overset{m \to 0}{\approx} \eta \equiv -ln \left(tan \frac{\theta}{2} \right). \tag{3.2.2}$$

Since the ATLAS detector is forward-backward symmetric, $|\eta|$ is often used.

3.2.1 The Inner Detector

The purpose of the ID is to provide the particle tracking and vertexing for ATLAS in the range $|\eta| < 2.5$. This is achieved with the help of a superconducting solenoid magnet, which provides a uniform 2 T magnetic field, in which the trajectories of charged particles are altered following Lorentz's law.

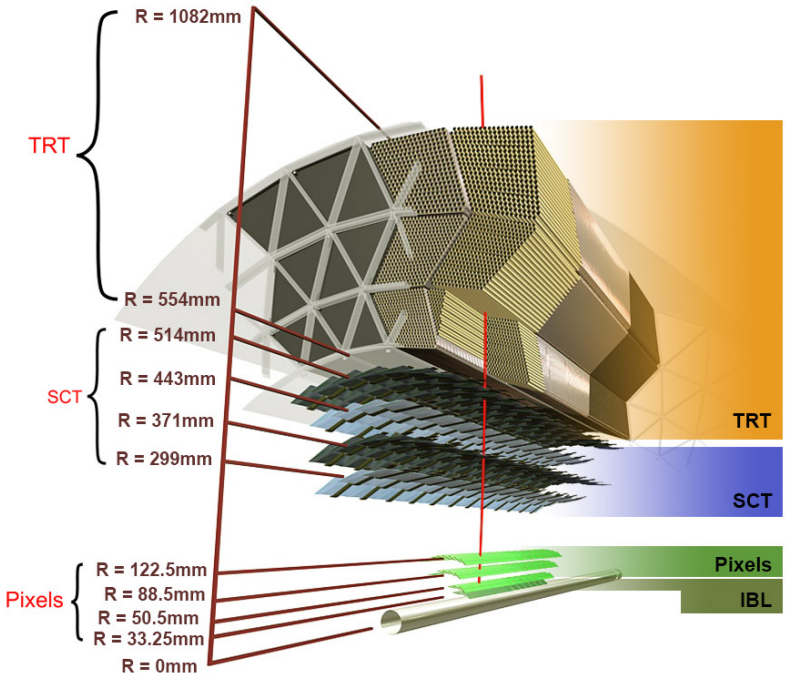

Figure 3.4: Schematic view of a sector of the ATLAS Inner Detector. Taken from [58].

Charged particles propagating through the different layers of the detector form "hits" by interacting with it. Using dedicated algorithms [55, 56], these hits are combined into "tracks" - a reconstruction of the particle's trajectory. The momentum and charge of the particle can then be inferred from the curvature of these tracks, as well as whether the particle was produced at the primary vertex or a secondary vertex of an interaction. The designed partial transverse momentum resolution if the ID is $\sigma_{p_T}/p_T = 0.05\% p_T \oplus 1\%$ [57] . The ID consists of three sub-detectors: the Pixel Detector (PD), the Semi-Conductor Tracker (SCT) and the Transition Ratiation Tracker (TRT), Figure 3.4.

The Pixel Detector

The silicon PD is the part of the ID closest to the beam pipe. It consists of 4 concentric cylindrical layers (barrel) around the interaction point and 3 disks at the ends (end caps). During LS1 between Run 1 and Run 2, a new layer was inserted, also known as the insertable B-layer. As it is situated at about 3 cm from the interaction point for improved tracking and secondary vertex reconstruction, it is built from radiation resilient materials in order to continue its operation in such a high particle density environment.

The Semi-Conductor Tracker

The SCT is similar in structure and function to the PD, but it uses silicon strips instead of pixels. It consists of 4 barrel layers and 9 disks on each end cap. The strips are mounted on both sides of the modules at a stereo angle of 40 mrad. This allows for the measurement of space-points with resolution of 17 μm in the $R-\phi$ plane and 580 μm along the z direction [49, 59].

The Transition Radiation Tracker

Unlike the other two ID subdetectors, the TRT consists of drift tubes. It provides track information within the transverse plane, with precision of 140 μm. This is achieved by exploiting the transition radiation phenomenon, occurring when a charged particle propagates through a boundary of two materials with different refractive indices. As the radiation is dependent on the relativistic γ factor of the particle, the TRT(Copy) provides differentiation between electrons and heavier charged particles.

3.2.2 The Electromagnetic Calorimeter

The ECal (Figure 3.5) is designed to measure the total energy of electrons and photons. It is of the sampling type with accordion geometry, where liquid Argon (LAr) serves as the active material and lead as the absorber. The combined thickness of the ECal corresponds to $\sim 22X_0$ [60], where X_0 is the radiation length at which an electron has lost $(e-1)/e$ of its energy through bremsstrahlung. The ECal is also split into barrel and end cap regions, providing coverage of $|\eta| < 1.475$ and $1.375 < |\eta| < 3.2$ respectively, with designed resolution of $\sigma_E/E = 10\%/\sqrt{E} \oplus 0.7\%$ [49].

3.2.3 The Hadronic Calorimeter

The measurement of jets, hadronically decaying tau leptons and missing transverse energies with resolutions of $\sigma_E/E = 50(100)\%/\sqrt{E} \oplus 3(10)\%$ in the barrel (end-cap) regions is provided by the ATLAS HCal (Figure 3.5). The barrel region of the HCal is divided into three sections, covering the rapidity range of $|\eta| < 1.7$. It is a non-compensating sampling calorimeter consisting of alternating layers of active scintillating material and absorber material in the form of steel tiles. The barrel thickness is $\sim 7.4\lambda$, where $\lambda = 20.7$ cm is the mean distance a hadron travels before it is inelasticly scattered [62]. In the forward region, the hadronic end-caps (HEC) consist of two wheels of copper-LAr sampling calorimeters each, extending the covered rapidity range to $|\eta| < 3.2$. High granularity information from both ECal and HCal is used to define regions of interest used by the ATLAS trigger system.

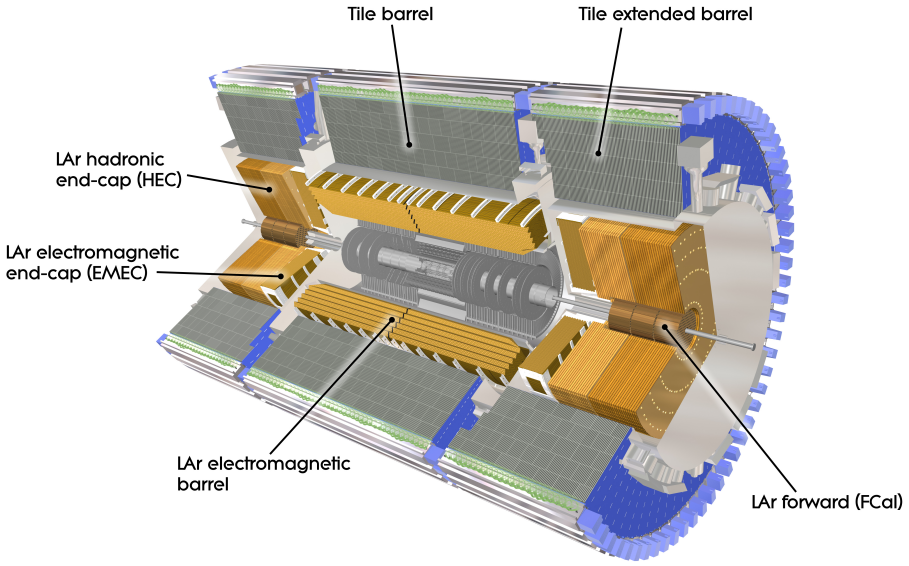

Figure 3.5: Computer generated image of the ATLAS calorimetry system. Taken from [61].

3.2.4 The Muon Spectrometer

The muon spectrometer is the outermost part of the ATLAS detector, designed to identify and measure the momentum of muons, as they travel through the rest of the detector without much interaction. The typical fractional momentum resolution is $\sim 3\%$, rising to $\sim 10\%$ at 1 TeV [63]. In addition to providing muon momentum measurement in the region $|\eta| < 2.7$, the MS also provides trigger systems for the particles in the range of $|\eta| < 2.4$.

The detector employs multiple technologies:

- monitored drift tubes (MDTs)
- gaseous parallel electrode plate detectors - resistive plate chambers (RPCs)
- two kinds of multi-wire proportional chambers - cathode strip chambers (CSCs) and thin-gap chambers (TGCs).

The magnetic fields generated by 3 air-core toroidal magnets (corresponding to the barrel and the two end cap regions) allow the measurement of the muon momentum. The muon trajectory in the barrel ($|\eta| < 1.05$) region is reconstructed from the hits of the muon on 3 cylindrical layers containing MDTs providing momentum tracking in the bending plane, while the non-bending coordinate information is provided by the RPCs. In the end-cap regions, $1.05 < |\eta| < 2.7$, the MDTs are mounted on four wheels, with the non-bending coordinate being measured by TGCs. In the most forward region

$(2.0 < |\eta| < 2.7)$ of the innermost wheel, the MDTs are replaced by CSCs, since the background rate in the region is too high for MDTs to be used. The layout of the MS is shown in Figure 3.6. Both RPCs and TGCs provide information to the ATLAS Level-1 trigger (L1), since they were designed to also provide coarser resolution measurements in the bending direction as well, with latency lower than the LHC bunch spacing [49, 64]. The operation of the trigger is summarised in Section 3.4.

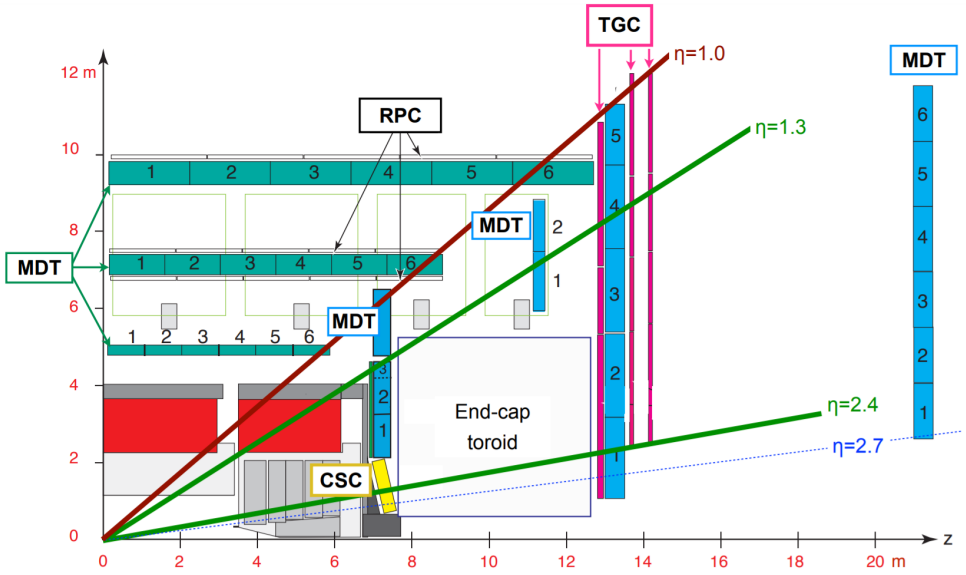

Figure 3.6: Quarter section cut-away view of the ATLAS muon spectrometer. Taken from Ref. [65].

3.3 Physical object reconstruction

As discussed in Section 3.2, different types of particles interact in different ways with the ATLAS subdetectors. A schematic of each kind of Standard Model (SM) particle and the expected signatures it leaves in the ATLAS system is shown in Figure 3.7. The following subsections define the objects which are built out of the detector readings and which are used in the analysis to represent these particles. The first step in reconstructing and identifying these objects is the formation of tracks in the ID and MS, identifying the primary vertex of the interaction and forming clusters out of calorimeter energy deposits. The physical object reconstruction is performed using the ATLAS software framework, Athena [66].

3.3.1 Track reconstruction

Tracks are seeded by requiring at least 3 space-points in the silicon trackers. Through the use of a combinatorial Kalman fitter [68], track candidates are

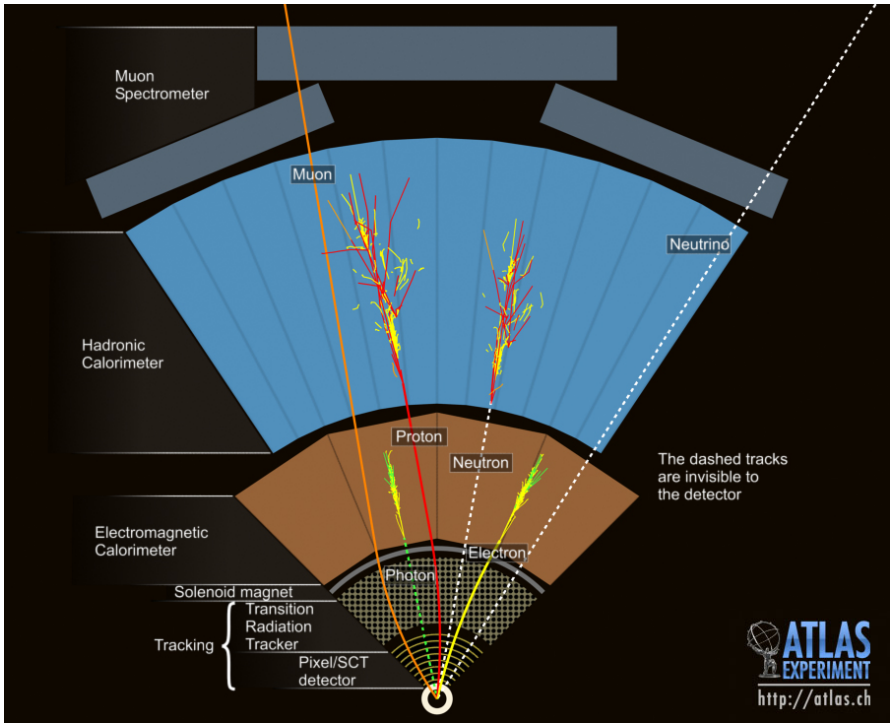

Figure 3.7: Computer generated schematic image of SM particles interacting with the ATLAS subdetectors. Taken from Ref. [67].

built by iteratively adding space-points from the silicon detector layers farther away from the IP. It is possible that multiple tracks are reconstructed by the fitting algorithm using the same track seed, in which case an ambiguity solver selects the track with the highest purity score. This score depends on the number of total hits in the track, the detector resolution in which the hits have occurred, the goodness of track fit. The remaining track candidates are then extended by including hits inside the TRT, increasing the momentum resolution. This method of track reconstruction is referred to as the "inside-out" approach. An "outside-in" approach, which starts from TRT hits and extending inwards, is employed to identify tracks which were missed by the "inside-out" method [69, 70]. Hits formed in the MS are further used in combination with the ID tracks in order to reconstruct possible muon candidates (see Section 3.3.5).

3.3.2 Vertex finding

Vertices are defined using an iterative fitting algorithm. A primary vertex seed is defined on the beam axis with z coordinate equal to the mode of z coordinates of the tracks at their points of closest approach. Tracks which are less compatible with the vertex are assigned smaller weights, after which the fit is repeated. After identifying the primary vertex of the interaction, each track with incompatibility of more than 7σ are not considered to be associated with it. A search for a new primary vertex is then performed with the remaining

unassociated tracks. Each primary vertex candidate is required to have at least two tracks associated with it. All vertices found by this approach, apart from the primary vertex, are considered as corresponding to pile-up events [71].

Additional vertices can be associated with the primary vertex due to long-lived particle decays originating from it - these vertices are identified using separate algorithms and used as inputs in jet flavour tagging, as described in Section 3.3.7.

3.3.3 Topological cluster formation

Three-dimensional reconstruction of localised energy structures, called topological clusters (or topo-clusters), is possible due to the calorimeters being segmented both radially and in the $\eta - \phi$ plane into cells. Depending on the incoming particle and any activity in the neighbourhood, the particle's cascade/shower could be entirely contained within one cluster, split into multiple clusters, or showers of multiple particles could contribute to a common cluster. A cluster can contain cells from both the ECal and the HCal.

The topological cluster formation algorithm is dependent on the cell signal-significance $|\varsigma_{\text{cell}}|$, defined as the ratio between the absolute value of the measured energy in the cell[2], $|E_{\text{cell}}|$, and the expected noise of the cell $\varsigma^{\text{exp}}_{\text{noise,cell}}$, which depends on the electronic noise and the average pile-up interactions, which is in turn dependent on the running conditions of the ATLAS detector. $|E_{\text{cell}}|$ and $\varsigma^{\text{exp}}_{\text{noise,cell}}$ are measured on the electromagnetic (EM) energy scale, which reconstructs the correct energies deposited by photons and electrons, but does not reconstruct the correct energies for hadrons due to the ATLAS calorimeter having a non-compensating nature. The clusters are seeded by cells with significance $|\varsigma_{\text{cell}}| > 4$, with adjacent cells being added to the cluster if they satisfy $|\varsigma_{\text{cell}}| > 2$. Finally, all cells adjacent to the boundary cells of the cluster are also included in it. A cluster splitting algorithm is also employed in case there are several local $|\varsigma_{\text{cell}}|$ maxima, a signature of multiple separate showers contributing to the structure [72, 73].

3.3.4 Electron reconstruction

In the analysis presented in this thesis, a single lepton (electron or muon) trigger is employed, leading to the requirement that an event must have a single lepton satisfying both the trigger requirements and the offline reconstruction selection.

Offline electron reconstruction

Electrons and photons deposit their energy inside the calorimeters through the chained mechanisms of bremsstrahlung and photon conversion. For electrons in

[2]Due to cell noise, the energy measured could be negative.

the region $|\eta| < 2.47$, ECal and HCal topo-clusters containing energy deposits are required to be matched with tracks in the ID. These tracks are refitted with a Gaussian Sum Filter to account for bremsstrahlung, since it can lead to deviations from the initial electron path [74]. Modified clusters, called superclusters, are built from the matched EM topo-clusters. If an EM topo-cluster satisfies the selection criteria ($E_T > 1$ GeV, matched to a track with > 4 hits in silicon detectors), it is used as a seed for a supercluster. Neighbouring topo-clusters in the $\eta - \phi$ plane, compatible with secondary EM showers, are also added to the supercluster. Calibrations to the superclusters are performed and a new matching, this time between the sets of superclusters and modified tracks, is performed. After an ambiguity resolver to differentiate between an electron and a photon reconstruction candidate is used, the appropriate physical objects are prepared for use in data analyses [75, 76].

To improve the purity of the selected electrons, additional identification based on a likelihood discriminant is used, with input variables derived from both the tracker and the calorimeter [77]. The electron identification can be defined at different values of the likelihood discriminant, resulting in different working points (WPs), each having an associated set of signal efficiency, background rejection rates and related uncertainties. While the optimal WP is different for each analysis depending on its selection criteria, a default set of already calibrated WPs is provided by ATLAS, with efficiencies shown in Figure 3.8. In addition to electron identification, isolation requirements are also imposed in order to distinguish electrons produced in the hard scatter or through the decay of heavy resonances from the electrons produced in heavy quark decays, electrons arising from photon conversion or misidentification of hadrons. This is performed by considering the calorimeter deposits in the vicinity of the electron candidate (excluding the candidate itself).

Photons are also commonly reconstructed by ATLAS (following a procedure parallel to the electron algorithm), but are not used in the analysis presented in this thesis.

Single electron triggers

The L1 trigger uses information from the calorimeters in the region $|\eta| < 2.5$ to build regions of interest (RoIs) to be used by the High Level Trigger (HLT). A sliding window algorithm is used in order to define 2×2 trigger towers with granularity 0.1×0.1 in η and ϕ and satisfying an transverse energy (E_T) threshold. Details of the procedure can be found in Ref. [78]. The HLT trigger consists of fast algorithms for early event rejection as well as precision algorithms, both of which require a match between tracks in the ID and calorimeter energy deposits. For electrons with $p_T > 15$ GeV, the fast

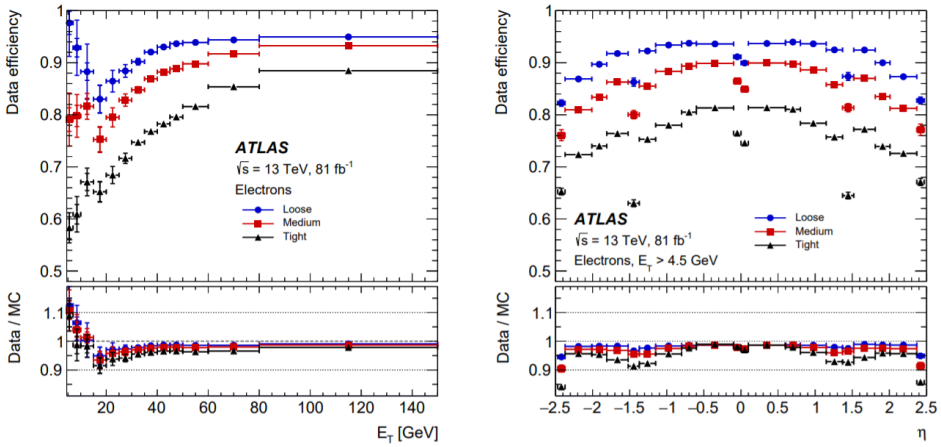

Figure 3.8: Measured electron identification efficiencies for *Tight*, *Medium* and *Loose* working points in $Z \to ee$ data events. The inner (outer) error bars represent the statistical (total) uncertainty. Taken from Ref. [75].

reconstruction algorithm employed is the 'Ringer' algorithm, which makes use of the conical structure of the EM showers around the initialising particle. The sum E_T in concentric rings in the different layers of the calorimeters around the most energetic tower are used as inputs into a neural network. For the precision algorithm, tracks from the ID are extrapolated to the EM calorimeter and required to be within $\Delta\eta < 0.05$ and $\Delta\phi < 0.05$ rad away from the matched cluster. The selection is based on a likelihood discriminant and the reconstruction resembles the offline reconstruction algorithm without the corrections for bremsstrahlung. Isolation requirements are applied based on track p_T in a cone around the electron - $p_T^{\text{iso}}(\Delta R^{\text{var}} < 0.2)/p_T^{\mu}$. The efficiency of the combination of the triggers e26_lhtight_nod0_ivarloose, e60_lhmedium_nod0 and e140_lhloose_nod0 is shown in Figure 3.9.

3.3.5 Muon reconstruction

Offline muon reconstruction

Muon spectrometer tracks are reconstructed by local track segments within separate muon stations. These segments are combined with other segments and a fit for the muon trajectory inside the magnetic field is performed [80].

Muon candidates are reconstructed using information from different combinations of the ID, calorimeters and the MS:

- combined (CB) - CB muons use the full information of the ATLAS detector - they match tracks from the ID and MS, taking into account energy losses inside the calorimeters

- inside-out combined (IO) - in the cases there is no reconstructed MS

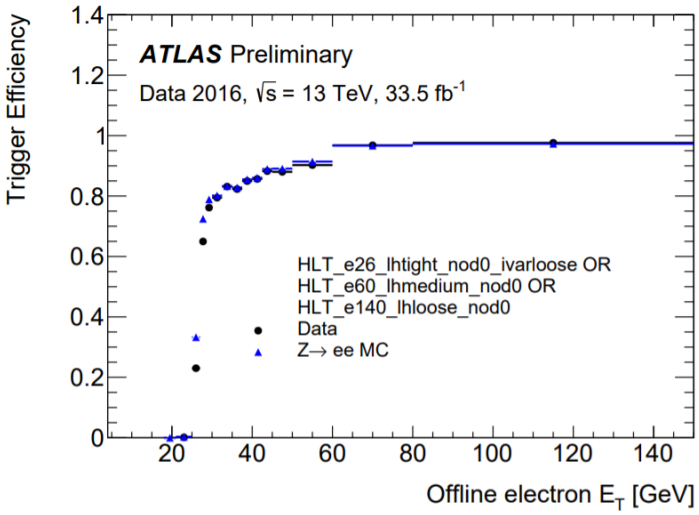

Figure 3.9: The trigger efficiency as a function of offline reconstructed E_T for the combination of triggers e26_lhtight_nod0_ivarloose, e60_lhmedium_nod0 and e140_lhloose_nod0 in the year 2016. The tag and probe method in $Z \to ee$ decays was used. Taken from Ref. [79].

track, this method extrapolates an ID track outwards and searches for at least three MS hits compatible with it

- Muon-spectrometer extrapolated (ME) - this method extrapolates an MS track with no corresponding ID track inwards

- segment tagged (ST) - an ID track is extrapolated outwards with the requirement that it is compatible with at least one MS segment. The muon parameters are extracted only from the ID track

- calorimeter tagged (CT) - an ID track is extrapolated outwards with the requirement it is compatible with calorimeter energy deposits consistent with a minimum-ionising particle. As in the ST case, the muon parameters are extracted only from the ID track [80].

Similar to the electron reconstruction, additional identification and isolation options exist in order to improve the purity of the selected muons. The muon identification depends on the type of reconstructed muon listed above, the number of hits in the ID and MS, as well as the compatibility of ID and MS track parameters. This compatibility is quantified by the significance $\varsigma_{q/p}$, defined as:

$$\varsigma_{q/p} = \frac{|q/p_{\mathrm{ID}} - q/p_{\mathrm{MS}}|}{\sqrt{\sigma^2(q/p_{\mathrm{ID}}) + \sigma^2(q/p_{\mathrm{MS}})}}, \tag{3.3.1}$$

where $q/p_{\mathrm{ID(MS)}}$ is the measurement of the charge-momentum ratio of the muon in the ID(MS) with corresponding uncertainties $\sigma(q/p_{\mathrm{ID(MS)}})$. The identification efficiency for *Medium* quality muons, requiring the muons to be

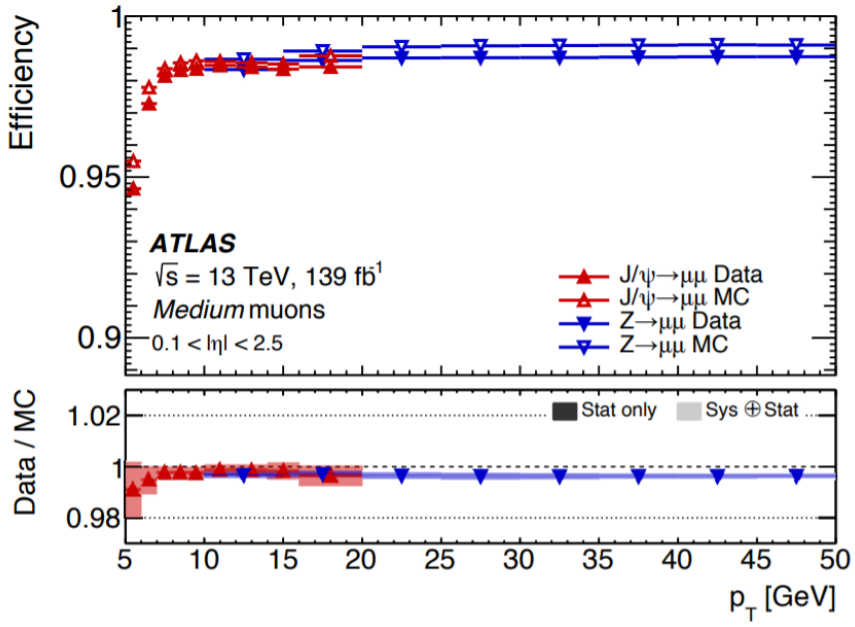

Figure 3.10: Efficiency for the *Medium* identification working point for muons as a function of p_T in the region $0.1 < |\eta| < 2.5$. The bottom panel shows the ratio between expected and measured efficiencies. Taken from Ref. [80].

either CB or IO muons, have at least two precision stations and a significance of $\varsigma_{q/p} < 7$, is shown in Figure 3.10.

As with electrons, isolation requirements are based on ID and calorimeter activity in a cone around the muon candidate [80, 81]. The sum of the transverse momenta $p_T^{\text{varcone30}}$ of tracks within a cone of variable radius of up to 0.3, $\Delta R = \min(10\text{ GeV}/p_T^{\mu}, 0, 3)$, around the muon in the ID is used, while the calorimeter based isolation variable is the sum of energy deposits $E_T^{\text{topocone20}}$ in a cone of $\Delta R = 0.2$.

Single muon triggers

As discussed in the MS section (Section 3.2.4), the sub-detector provides trigger information for muons. L1 receives information from the RPCs and TGCs in the barrel ($|\eta| < 1.05$) and end-cap ($1.05 < |\eta| < 2.4$) regions respectively. During Run 2, the L1 single muon trigger algorithm required a set of 3 concentric RPC station hits to be compatible with a muon trajectory. In the end-cap regions, 3-station-stip[3] coincidence of TGC hits were required. The RoIs indentified this way are sent to the HLT, where fast reconstruction algorithms are applied. The candidate muons are identified using MS information only (stand-alone muons) and then combined with ID tracks to form combined (CB) muons. Requirements for muon isolation are implemented by a requirement on the sum

[3]In the 2015 period, only 2 hits were required.

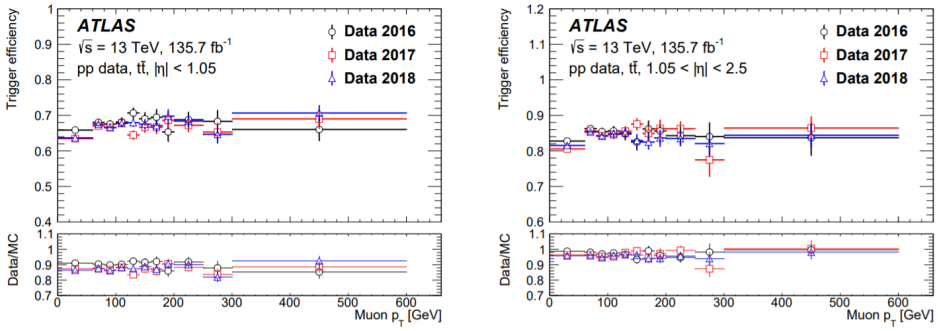

Figure 3.11: Efficiencies of passing either mu26_ivarmedium or mu_50 as a function of muon p_T in the barrel region (left) and the end-cap regions (right). Error bars show statistical uncertainty only. Taken from Ref. [82].

of track p_T in the vicinity of the muon in the ID as a fraction of the muon's p_T, $\sum_{\Delta z<6(2)} p^{\text{trk}}/p_T^{\mu}$. The region is defined as $\Delta z < 6$ mm (2 mm in 2018), where Δz is the distance between the track and the primary vertex along the z-axis [82].

The efficiency of triggering on muons using mu26_ivarmedium or mu_50, corresponding to requirements of a $p_T > 26$ GeV CB muon with $\sum_{\Delta z<6(2)} p^{\text{trk}}/p_T^{\mu}$¡0.07, or a CB muon with $p_T > 50$ GeV is shown in Figure 3.11.

3.3.6 Jet reconstruction

As Quantum Chromodynamics (QCD) is a non-Abelian Quantum Field Theory (QFT), the force carriers (gluons) also carry the charge of the interaction - colour. Gluons and quarks, unlike photons and charged leptons, are not directly observable due to the colour confinement phenomenon - after production, they immediately undergo hadronisation, generating a collection of collimated colourless bound states - hadrons. In order to study the properties of the initiating particle, the final state shower of particles associated with it are combined together into a jet. In ATLAS, jets form cascades/showers in the ECal and HCal, as well as tracks in the ID.

There are two categories of jet-finding algorithms, cone and sequential recombination algorithms, with jet definitions required to satisfy the following criteria:

- could be easily implemented in both experimental and theoretical analyses
- defined at and yielding finite cross-sections at any order of perturbation theory
- yield cross-section which is insensitive to hadronisation effects [83].

The ATLAS experiment uses a type of sequential recombination algorithm.

In this approach, the "distances"[4] between every two particles i and j, d_{ij}, and each particle and the beam direction, d_{iB}, are used. If the smallest of all, $\min\{d_{ij}, d_{iB}\}$, is d_{mn}, particles m and n are combined into a pseudo-particle and the search for the next minimum distance is performed. In case $\min\{d_{ij}, d_{iB}\} = d_{kB}$, (pseudo-)particle k is declared a jet and is removed from consequent searches. This is repeated until there are no particles remaining. In collider experiments, the choice for the definition is made so d_{ij} is invariant under boosts along the beam axis:

$$d_{ij} = \min\{p_{T,i}^{2n}, p_{T,j}^{2n}\}\frac{\Delta R_{ij}^2}{R^2}, \tag{3.3.2}$$

while the beam distance is:

$$d_{iB} = p_{T,i}^{2n}, \tag{3.3.3}$$

where $p_{T,i}$ is the transverse momentum of particle i, ΔR_{ij} is the angular distance between i and j, with $\Delta R_{ij} = (H_i - H_j)^2 + (\phi_i - \phi_j)^2$ with H the rapidity, ϕ the azimuth angle, and R is the radial parameter of the jet. The anti-k_T algorithm is defined by setting $n = -1$, favouring the clustering of hard collinear particles as opposed to the k_T ($n = 1$) and the Cambridge/Aachen ($n = 0$) algorithms [84].

Jets are reconstructed using the anti-k_T algorithm described above in combination with the particle flow (PFlow) algorithm [85], which exploits the better ID momentum resolution of low momentum charged particles compared to the corresponding calorimeter energy resolution. The tracks used are required to have $0.5 < p_T < 40$ GeV and not be associated with any reconstructed electrons or muons. The algorithm then matches a track to a single topological cluster in the $\eta - \phi$ plane and computes the expected energy deposited in the calorimeter based on the momentum of the track. A discriminant is then used to estimate the compatibility of the deposited energy in the matched cluster to the expected energy. If the matched cluster energy is insufficient, additional clusters are added to the track-cluster system. The expected energy is then subtracted from the collection of matched cluster energy cell by cell. If the remainder is compatible with shower fluctuations, the remnant of the measured cluster system is discarded, while if the remainder is incompatible, the cluster is kept. Compared to previous (topo-cluster based) jet reconstruction algorithms, the PFlow algorithm yields improved jet energy resolution (JER), reduced pile-up (defined in Section 3.4) jet rates [85] and better estimation of E_T^{miss} in high pile-up environments [86].

Pile-up jets are suppressed by the jet vertex tagger (JVT) likelihood discriminant. This method uses track based variables to derive a score which

[4]Here, the "distances" used do not have the usual units of measurement - the units depend on the weight given to the particle p_T defined below.

varies between 0 (more characteristic of a pile-up jet) and 1 (more characteristic of a jet produced from the hard-scatter of the event recorded) [87]. Jets with $20 < p_T < 60$ GeV and $|\eta| < 2.4$ are required to satisfy a JVT cut of 0.5.

3.3.7 Jet flavour tagging

ATLAS makes use of flavour labels (*jet_truthflav* container), by which a jet is labeled as a b-/c-/τ-jet depending on whether the heaviest flavour particle found with $p_T \geq 5$ GeV and within $\Delta R \leq 0.3$ of the jet axis is a b-/c-hadron or a τ-lepton. In the case none of these are found, the jet is labeled as a light(l)-jet[5].

The presence of a heavy (b- or c-) quark inside a jet can be inferred from the jet properties extracted by several low-level tagging algorithms, the outputs of which are then combined into a single variable by a high-level algorithm. The high-level flavour tagging algorithm used in this analysis is based on a deep learning neural network (NN) known as DL1r [88]. The low-level taggers used with DL1r are [89]:

- Secondary vertex (SV1) algorithm [90] - this tagger makes use of the decay time of B-hadrons. Due to the dominant decays of b-hadrons being weak decays to c-hadrons, the rate of the decay is proportional to $1/|V_{cb}|^2$, leading to the relatively long lifetimes of b-hadrons (typical mean lifetime of $\tau_b \sim 1.5$ ps [9]). This leads to the displacement of the vertex of the b-hadron decay from the primary interaction vertex. Information about the secondary vertex, like its mass and number of tracks, is passed by SV1 to the high-level tagger.

- Topological secondary and tertiary vertices (JetFitter) [91] - this tagger makes use of the lifetime of both the B-hadron and the subsequent C-hadron, which result in two displaced vertices inside the jet. JetFitter attempts to reconstruct the full $b \to c \to s$ decay chain, providing additional discrimination power from jets initiated by C-hadrons and hadronically decaying τ leptons.

- Impact parameter based algorithms (IP2D,IP3D, RNNIP)[92, 93] - these taggers make use of the significance of impact parameters of the tracks within jets. IP2D makes use of the transverse impact parameter significance ($d_0/{\sigma_{d_0}}^6$), while IP3D, uses in addition the longitudinal impact parameter significance ($z_0 sin\theta/{\sigma_{z_0 sin\theta}}^7$). The outputs of IP2D and

[5]The symbol l will be used to refer to light quarks (u, d or s, unless otherwise stated), while leptons will be referred to by the symbol ℓ.

[6]d_0 is defined as the distance of closest approach to the primary vertex of the interaction in the $r - \phi$ plane.

[7]$z_0 sin\theta$ is defined as the distance along the z axis of the point defined by d_0.

IP3D for each track are independent, while RNNIP includes correlations between tracks inside the jet by using a recurrent NN.

The DL1r algorithm provides 3 outputs - p_l, p_c, p_b - which represent the probability of the jet in question being a light, charm or beauty jet. These outputs are combined into a final score, which determines whether a jet is flavour tagged or not.

The efficiencies and mistag rates at ATLAS are defined using the flavour labels (*jet_truthflav*) defined previously. The efficiency ϵ_i is defined as the probability of identifying a jet of flavour i as an i-tagged jet, while the mistag rate f_{ij} is defined as the probability of misidentifying a jet of flavour i as a j-tagged jet. In the analysis presented in this thesis, a slightly different definition was used in the event selection. The container *jet_truth_partonLabel* was used, which assigns the jet the flavour of the truth parton with the highest energy within its cone and differentiates between g-, u-, d- and s- jets, while *jet_truthflav* classifies all of them as l-jets. In addition, as the aim is the measurement of the CKM matrix element $|V_{cb}|$, the flavour of the quark initiating the jet is of interest, which is not necessarily the same flavour as the flavour label (*jet_truthflav*) of the jet (e.g. a radiated gluon inside a jet could decay into a $b\bar{b}$ pair satisfying the label requirements for classifying the jet as a b-jet, while the initial quark is not itself a b-quark).

Beauty tagging (b-tagging)

The DL1r final score for b-tagging is determined based on the tagger outputs using the equation:

$$S^b_{\text{DL1r}} = \frac{p_b}{(1 - f_c)p_l + f_c p_c}, \tag{3.3.4}$$

where f_c is the weight given to the c-jets in relation to the light jets in the determination of the score. This fraction is fixed to $f_c = 0.018$ [88], but in general can be tuned. A jet is considered a b-tagged jet if its S^b_{DL1r} score is greater than a value depending on the WP used. The efficiency and mistag rates of the DL1r b-tagger compared to the other available ATLAS high-level taggers are shown in Figure 3.12. DL1 uses the same deep-learning NN as DL1r and has the same low-level tagger inputs, apart from RNNIP. MV2 [92] has the same inputs as DL1, but it is based on a boosted decision tree (BDT) discriminant.

Charm tagging (c-tagging)

d taganThe method of identifying jets as c-tagged follows the same logic and tagger outputs as the one used for b-tagging, with the final score being modified

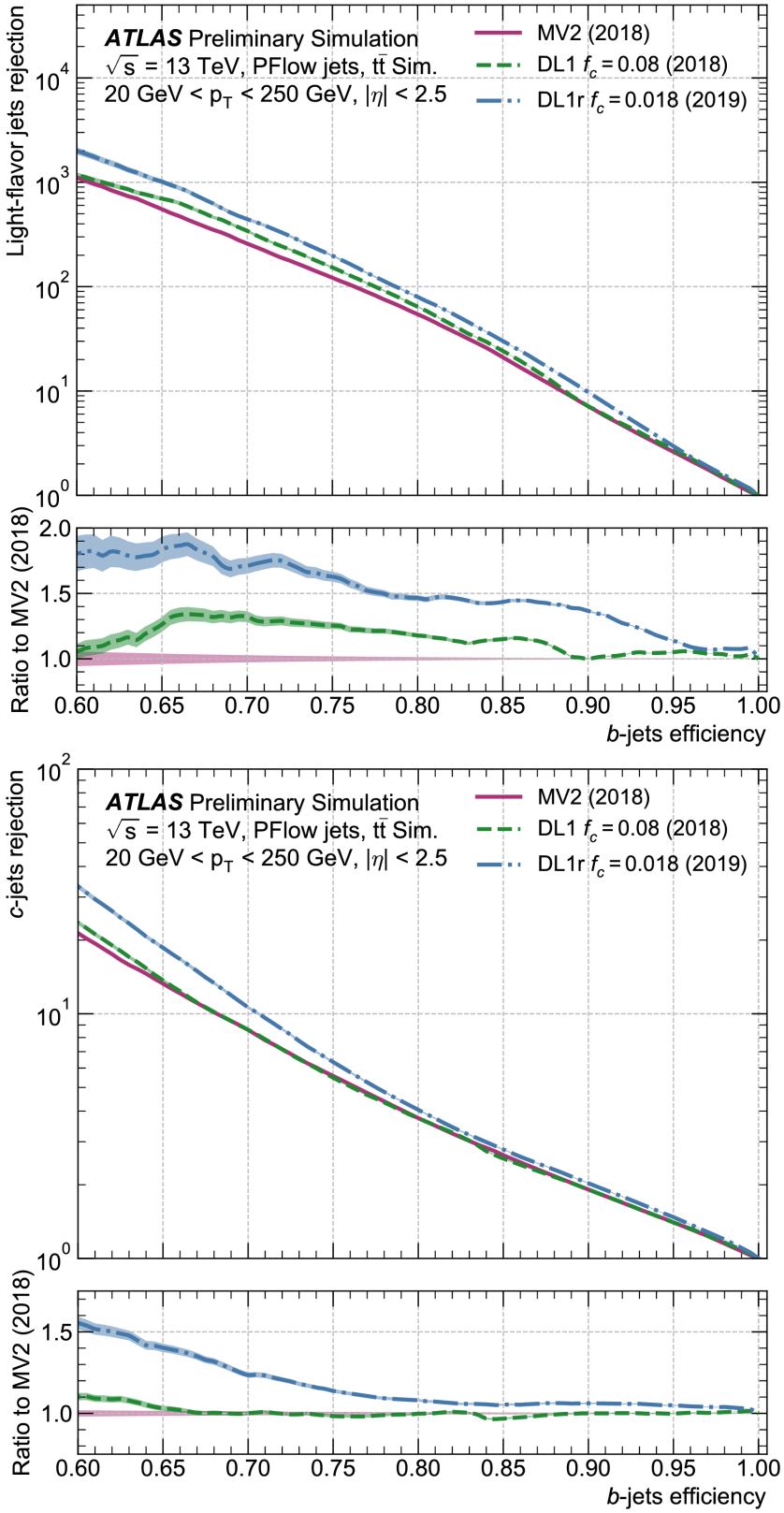

Figure 3.12: Comparison between DL1r, DL1 and MV2 high-level flavour taggers used in b-tagging of EMPFlow jets in $t\bar{t}$ events in ATLAS. Light-jet rejection (top) and c-jet rejection (bottom) as functions of b-jet efficiency, with rejection defined as the reciprocal of the mistag rate. The shaded regions represent the statistical uncertainties. Taken from Ref. [94].

to:

$$S^c_{\mathrm{DL1r}} = \frac{p_c}{(1-f_b)p_l + f_b p_b}, \tag{3.3.5}$$

where f_b is the weight given to the b-jets in relation to the light jets. For the analysis presented in this thesis, an optimal WP was chosen, defined by the cut value of $S^c_{\mathrm{DL1r}} = 2.13$ and $f_b = 0.01$.

Mutually exclusive tagging outcomes

With the use of both b-tagging and c-tagging algorithms, there exists a probability for a jet to be tagged by both. In order to eliminate ambiguities, any jets tagged by the b-tagging algorithm are considered b-tagged jets. Jets which do not satisfy the b-tagging criterion but satisfy the c-tagging one are considered c-tagged jets. A truth-matched sample (defined in Section 6.2) was used to generate the distributions of jets in the (S^b_{DL1r}, S^b_{DL1r}) plane for (f_b, f_c) = (0.001, 0.018) shown in Figure 3.13 separately for jets marked as b-/c-/l-quark by the *jet_truth_partonLabel* variable.

This mutual exclusivity allows for the tagging matrix:

$$\begin{pmatrix} f_{ll} & f_{lc} & f_{lb} \\ f_{cl} & f_{cc} & f_{cb} \\ f_{bl} & f_{bc} & f_{bb} \end{pmatrix} = \begin{pmatrix} \epsilon_l & f_{lc} & f_{lb} \\ f_{cl} & \epsilon_c & f_{cb} \\ f_{bl} & f_{bc} & \epsilon_b \end{pmatrix} \tag{3.3.6}$$

to have the constraints $\sum_i f_{ij} = 1$, where i,j $\in\{l,c,b\}$. Jets which were generated by gluons are not included in the simplified model using the above tagging matrix. Effects caused by gluon jets and strategies to reject them are discussed in Section 6.2.3.

3.3.8 Tau reconstruction

With a lifetime of $\tau_\tau \sim 0.3$ ps [9], tauons decay before reaching the ATLAS tracker, making their reconstruction dependent on the detection of their decay products. They are the only leptons with enough mass to allow their decay into hadrons. In the leptonic decay case τ_{lep} ($\tau \to \ell\overline{\nu}_\ell\nu_\tau$), the produced electron or muon are indistinguishable from their prompt counterparts and are thus reconstructed using the lepton reconstruction algorithms. The hadronic case (τ_{had}) is characterised by the production of an odd number of charged hadrons imposed by charge conservation - the vast majority of decays are either 1-prong or 3-prong[8], referring to the number of tracks associated with the τ_{had}. The object which is reconstructed by the tau algorithm is the visible part of the tau decay, $\tau_{\mathrm{had\text{-}vis}}$, representing the collection of observed charged and

[8]Decays with 5 charged hadrons are allowed, but they are rare and not investigated by the default tau reconstruction algorithm.

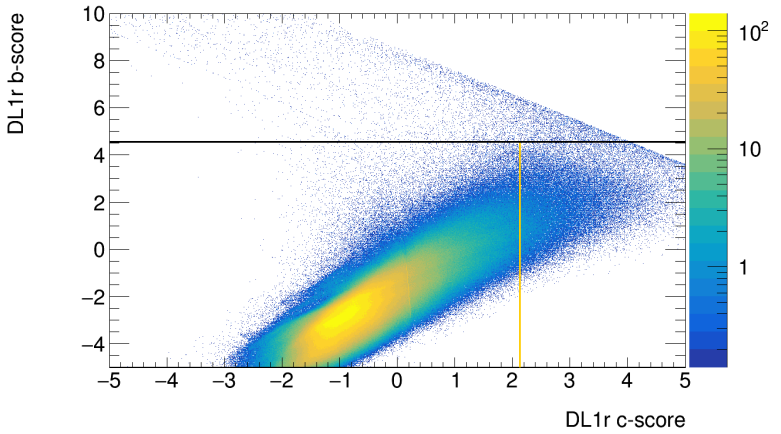

(a) l-jets

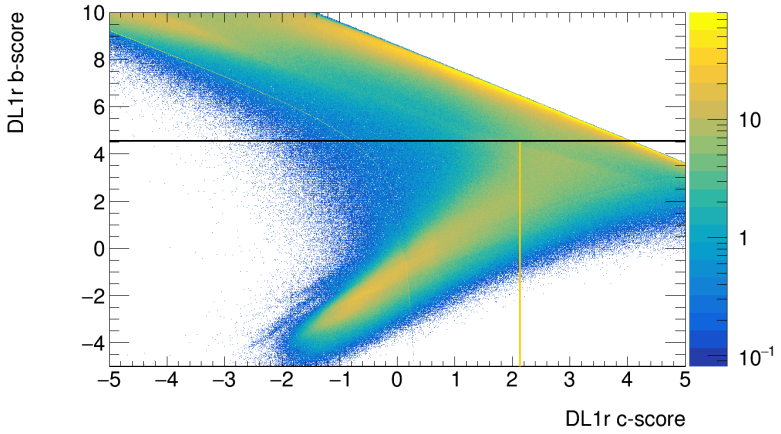

(b) b-jets

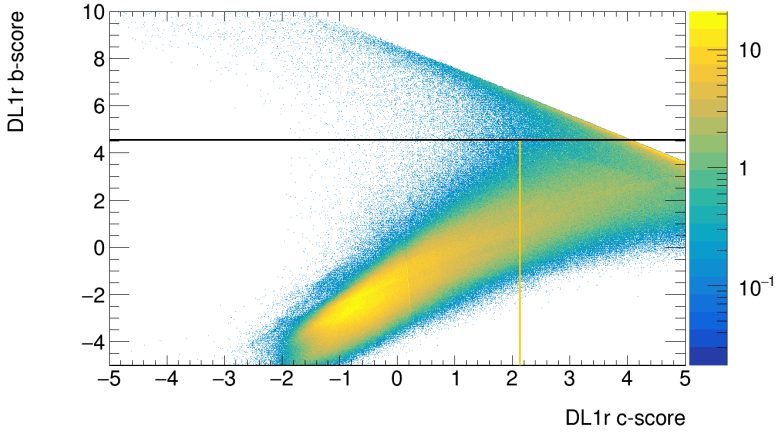

(c) c-jets

Figure 3.13: Scatter plots of the DL1r b-tagging score against the DL1r c-tagging score for (a) - light jets, (b) - beauty jets, (c) - charm jets for fractions $f_c = 0.018$ and $f_b = 0.01$. For the combination of working points optimal for this analysis, jets with b-score above 4.565 (black line) are taken to be b-tagged jets (corresponding to the 60% WP), jets with b-score below 4.565 and c-score above 2.13 (orange line) are taken to be c-tagged jets, while the rest are considered light jets. The z axes are logarithmic to aid visualisation.

possible neutral hadrons generated in the decay. The invisible decay products correspond to the neutrino and any charged or neutral decay products which are not detected, resulting in missing transverse energy.

Candidates for $\tau_{\text{had-vis}}$ are seeded by reconstructed jets fulfilling the requirements of $p_T > 10$ GeV and $|\eta| < 2.5$, excluding the transition region between the end-cap and barrel calorimeters ($1.37 < |\eta| < 1.52$). The tau vertex is defined as the vertex with the highest p_T sum of tracks associated with the jet ($\Delta R < 0.2$). These tracks are required to satisfy $p_T > 1$ GeV and impact parameter criteria with respect to the tau vertex. The vertex is used to define the direction of $\tau_{\text{had-vis}}$ and to define the origin for identification variables [95]. Special energy calibrations are then applied to the candidates. In order to distinguish true tau decays from jets, a BDT is employed with the variables extracted from the tracker and calorimeter mentioned above. This is done for taus associated with one track and three tracks separately [95].

3.3.9 Overlap removal

Since the different physical object reconstruction algorithms use detector information independently, the identification of an object is sometimes ambiguous. In order to select only one outcome for the particle so it is not doubly counted in the event, a procedure known as overlap removal (OR) is employed. In the analysis presented in this thesis, the "recommended" OR options are used, with the relevant removed objects being:

- any electron with a track overlapping with any other electron
- any calorimeter muon found to share a track with an electron
- any electron found to share a track with a muon
- any jet found within $\Delta R < 0.2$ of an electron
- any electron subsequently found within $\Delta R < 0.4$ of a jet
- any jet with less than 3 tracks associated to it found within $\Delta R < 0.2$ of a muon
- any jet with less than 3 tracks associated to it which has a muon inner-detector track ghost-associated to it
- any muon subsequently found within $\Delta R < 0.4$ of a jet is removed
- any tau found within $\Delta R < 0.2$ of a LooseLH electron
- any tau found within $\Delta R < 0.2$ of any type of muon with $p_T > 2$ GeV
- any jet found within $\Delta R < 0.2$ of a tau.

3.3.10 Missing transverse momentum

Particles which interact only weakly (neutrinos) and potential BSM candidate particles which do not interact with the detector escape without being detected by it. Despite this, information about them could be inferred through the use of the magnitude of the missing transverse momentum (MET), p_T^{miss} or E_T^{miss}, of the event. Since protons are composite objects, the momentum fraction carried by the interacting parton along the beam axis is unknown. However, the partonic momentum in the transverse plane can be considered negligible. Thus, any transverse imbalance in the reconstructed final state could indicate the presence of an undetected particle. The missing transverse momentum is defined as:

$$\vec{p}_T^{\,\text{miss}} = -\sum_{i\in\{\text{hard objects}\}} \vec{p}_{T,i} \; - \sum_{j\in\{\text{soft objects}\}} \vec{p}_{T,j}, \tag{3.3.7}$$

where the first term of the right hand side represents the sum over the transverse momenta of the reconstructed hard objects (in this analysis, they are the lepton and the jets), while the second, "soft" term, is the sum over charged-particle tracks which are associated with the interaction but are not associated with any reconstructed hard object. As the calculation of the MET involves input from all ATLAS subdetectors, it is susceptible to errors arising from object momentum mismeasurement and miscalibration, objects missing the detector, as well as from objects arising from pile-up interactions [86, 96].

3.4 Data taking with ATLAS during LHC Run 2

The analysis presented in this thesis aims to use the complete dataset collected during the LHC Run 2 period of pp collisions with centre-of-mass energy of $\sqrt{s} = 13$ TeV using the ATLAS detector. The luminosity generated (also referred to as the delivered luminosity from the start of stable beams operation until the LHC requests ATLAS to be put on stand-by mode to allow for a beam dump or beam studies) by the LHC during Run 2 and the fraction of it satisfying the data quality required to be available for physics analyses at ATLAS is shown in Figure 3.14.

With the designed LHC peak luminosity of 10^{34} cm^{-2}s^{-1} (which was more than doubled in Run 2), the rate of collision information being generated is higher than the speed at which it can be processed by the detector and saved to disk. In order to select and record only physically "interesting" events, a two stage trigger system [98] is employed with selections on online reconstructed objects. The first step is the L1 [99], which reduces the rate from 40 MHz (corresponding to the 25 ns bunch spacing) to a maximum of 100 kHz. It

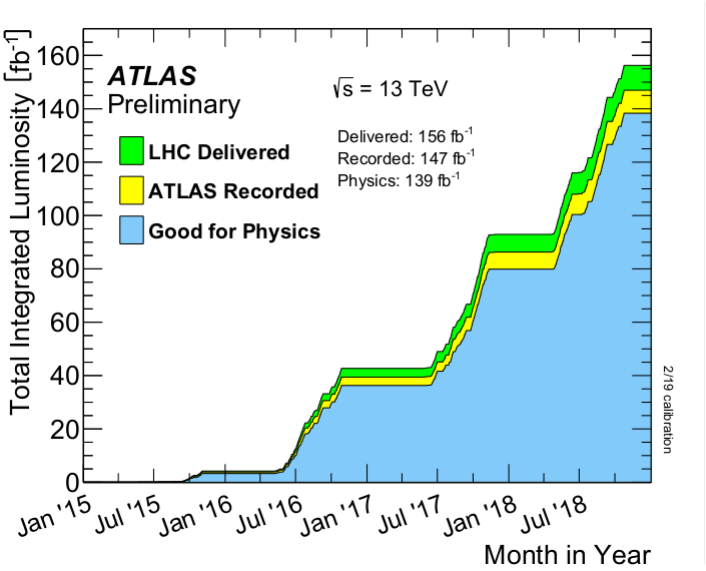

Figure 3.14: Cumulative luminosity over time during Run 2 of the LHC. Luminosity delivered by the LHC to the ATLAS detector (green), luminosity recorded by the ATLAS detector (yellow), luminosity satisfying the requirement for good quality physics objects (blue). Taken from Ref. [97].

is a hardware-based trigger using coarse granularity information from the calorimeters and the muon spectrometer to define RoIs within 2.5 μs per event. The RoIs are then sent to the software-based HLT, which uses the full detector information within the RoIs or the whole event to make the final decision whether to discard the event or send it for storage. This reduces the rate further from 100 kHz to 1 kHz [100]. After the data is stored at the CERN Tier-0 computing centre, more user-friendly formats are prepared from it with post-processing, including offline physical object reconstruction and calibration. A schematic view of the trigger system is shown in Figure 3.15.

As the event rate at the LHC is so high, detector readings from collisions other than the event of interest could affect its object reconstruction. Such collisions are collectively referred to as pile-up, divided into in-time and out-of-time contributions. In-time pile-up is caused by additional pp interactions in the same bunch crossing as the collision of interest. The average interactions per bunch crossing for Run 2 is shown in Figure 3.16. Out-of-time pile-up is caused by collisions from previous and next bunch crossings, where the electronics have longer processing time than the 25 ns bunch crossing rate. Pile-up contributions to events are reduced by methods described in Section 3.3.

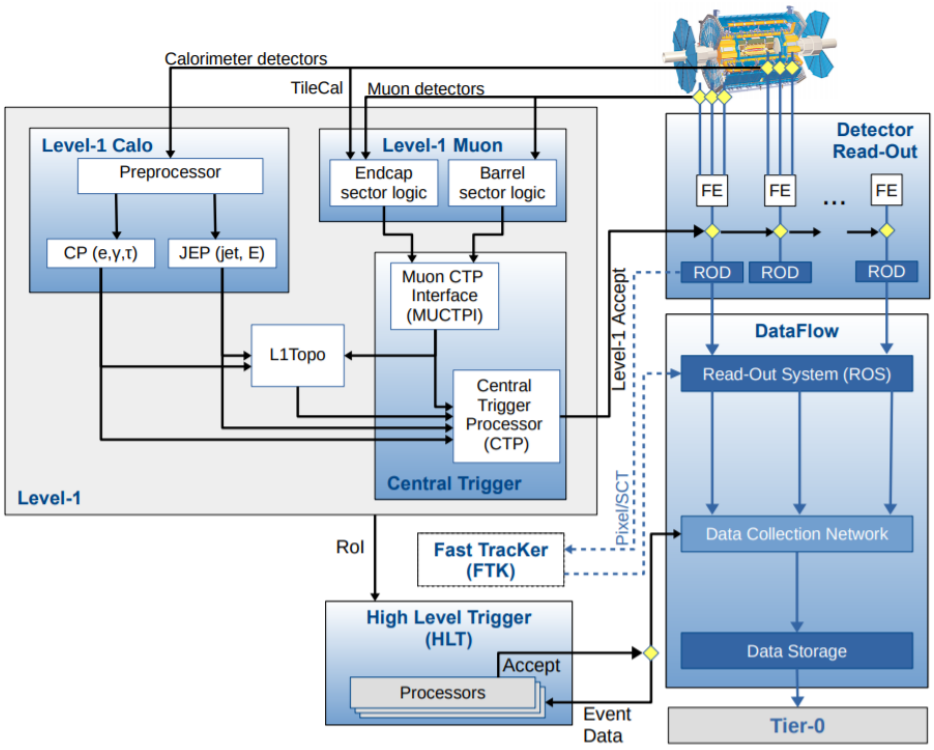

Figure 3.15: Schematic view of the Run 2 ATLAS trigger system and data flow. Taken from Ref. [98].

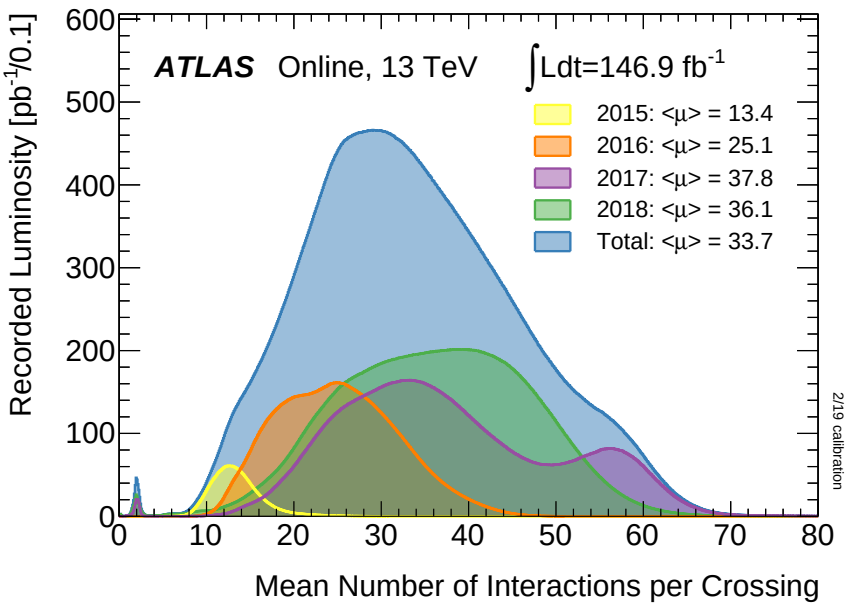

Figure 3.16: Mean number of interactions per bunch crossing $< \mu >$ for the data recorded by ATLAS during the separate years of data taking throughout the LHC Run 2 period. Figure taken from Ref [97].

3.5 Event and detector simulation at ATLAS

Monte Carlo event generators (MCEGs), in combination with detector simulations, are used in order to compare theoretical predictions with experimental observations. The analysis presented in this thesis is "blinded" - the selection and fitting strategy is determined entirely by event yields extracted from MC simulation, with the same procedure duplicated later using data gathered by the ATLAS experiment.

The factorisation theorem (as described in Section 2.4.2) allows for the computation of inclusive QCD cross-sections by the use of parton distribution functions (PDFs) $f^H(x, \mu_F)$ and the hard scattering cross-section $\hat{\sigma}_{ij\to X}$ (usually computed at next to leading order - NLO):

$$\sigma_{H_1H_2\to X} = \sum_{i,j} \int_0^1 dx_i f_i^{H_1}(x_i, \mu_F) \int_0^1 dx_j f_j^{H_2}(x_j, \mu_F) \times \hat{\sigma}_{ij\to X}(\mu_F, \mu_R). \tag{3.5.1}$$

The resulting cross-section is the inclusive cross-section of collisions of hadrons H_1 and H_2 resulting in X, which contains any number of final state particles and having any kinematic configuration. Gluon radiation as well as gluon splitting into quark pairs is simulated through Markov processes, with each new particle generation conserving four momentum and probability [101]. This radiation of particles can be categorised as initial state radiation (ISR) or final state radiation (FSR), depending on whether these particles are generated from the initial or the final state particles of the hard scatter. As the products of these gluon and quark pair emissions can initiate new such radiation, the process is called parton showering. The probability of such splitting is governed by the DGLAP [38] splitting function, linking the ensemble of particles at the (higher) energy scale before splitting to the resulting ensemble of particles at the (lower) energy scale after splitting. In order to avoid double counting or mismatching between particles from the hard scatter and from the parton shower, the particles are matched between the two using methods like CKKW [102] or MLM [103][101]. As the parton shower and the matrix element generation can be separated, they are often handled by different MCEGs. As perturbation theory is only applicable down to the energy scale of ~ 1 GeV, the parton showers are evolved to this energy, leaving coloured partons as final states. As only colourless particles are observed in nature, and since the phenomenon of colour confinement is non-perturbative, model approximations are used in order to group the coloured partons into colourless hadrons. Different hadronisation models include the Lund string model [104] and the cluster-hadronisation model [105]. The resulting generated events are then used as inputs for the GEANT4 toolkit [106], which simulates the paths of the particles through the

Year	peak L ($\times 10^{34}$ cm^{-1}s^{-1})	$\int Ldt$ (fb^{-1})	$< \mu >$	Monte Carlo subcampaign
2015	0.5	3.2	13.4	MC16a
2016	1.4	33.0	25.1	
2017	2.1	44.3	37.8	MC16d
2018	2.1	59.9	36.1	MC16e

Table 3.1: Summary of peak instantaneous luminosity, integrated luminosity, mean interactions per bunch crossing and corresponding Monte Carlo subcampaign for each year of data-taking at ATLAS.

entire ATLAS detector, including any sources of inefficiency (e.g. dead cells and misalignments) present. The output of the toolkit are digital signals, equivalent to the ones gathered by the ATLAS detector.

In the analysis presented in this thesis, ATLAS Top working group derivations (TOPQ1) of MC samples from the mc16 simulation campaign were used to define the event selection criteria and estimate the contributions stemming from the signal and the background processes. The campaign is divided into three sub-sets of events which simulate the detector conditions during the different years of data taking, Table 3.1. The values given for the integrated luminosity correspond to the ATLAS recorded events which also satisfy the selection for physics analyses by the "Good Runs List" (GRL). The samples used in the analysis presented in this thesis are the nominal samples used by the Top working group and are summarised in Table 3.2. The NonAllHad $t\bar{t}$ sample contains events which were generated with both W bosons decaying leptonically (referred to as LepLep and including any pairs containing electrons, muons and taus) and events with one hadronically and the other leptonically decaying W (referred to as LepHad and including ℓ+jets). A fully hadronically decaying $t\bar{t}$ sample was found to have negligible contribution and was not included in the analysis presented in this thesis. The NonAllHad sample's hadronic W decays contain only quark pairs which were generated through the Cabibbo angle (ud,cs, us, cd) and do not contain events with W decaying into b-quarks. The events are generated by utilising the Powheg-Box-v2 [107], an next-to-leading order (NLO) QCD matrix element (ME) generator interfaced with Pythia8 [108], which is responsible for the simulation of the parton shower, hadronisation and fragmentation. In order to include the signal process of the analysis presented in this thesis, a separate sample containing only LepHad events in which $W_{\text{had}} \to cb$ is used and denoted as the $|V_{cb}| = 1$ sample. The single top sample contains the processes discussed in Section 2.4.3 (t-channel, s-channel and Wt). The W+jets contains events in which $W \to e/\mu/\tau + \nu$, Z+jets contains events with $Z \to ee/\mu\mu/\tau\tau$, and the Diboson sample (ZZ,ZW, WW) contains all possible decay channels apart from those

Process	generator
NonAllHad $t\bar{t}$	POWHEG+PYTHIA8
$t\bar{t}$ $\|V_{cb}\| = 1$	POWHEG+PYTHIA8
Single top	POWHEG+PYTHIA8
W+jets	SHERPA
Z+jets	SHERPA
Diboson	SHERPA

Table 3.2: The nominal samples used to estimate the background contributions to the analysis.

resulting in 4 quarks or 4 neutrinos.

Chapter 4

ATLAS authorship task

4.1 Introduction

The increase of the instantaneous luminosity during the High Luminosity Large Hadron Collider (HL-LHC) era ($5-7\times$ the LHC design luminosity of 10^{34} $\mathrm{cm}^{-2}\mathrm{s}^{-1}$) will result in the increase of the average number of interactions per bunch crossing to $<\mu>=200$ ($\sim 6\times$ average LHC Run 2 value), leading to the requirement of a tracking detector with higher granularity and shorter readout times than the current ATLAS Inner Detector (ID). As the radiation fluence around the nominal interaction point (IP) is expected to accumulate to $\sim 2\times10^{16}$ 1 MeV $n_{eq}/$ cm^{-2} ($\sim$ 20 times the predicted current detector value at end of Run 3 [109]) by the end of HL-LHC operation, the detector is required to be constructed from more radiation resistant materials compared to the ID [110]. In order to prepare the ATLAS detector for HL-LHC operation, the ID is scheduled to be replaced by a new all-silicon tracker, the Inner Tracker (ITk), during LS3. It will consist of an inner pixel subsystem ($|\eta|<4$), surrounded by an outer strip subsystem ($|\eta|<2.7$), Figure 4.1. The strip modules are mounted on staves in the barrel region and on petals in the end-cap regions and are composed of a silicon sensor, one or two printer circuit boards glued on it which host the ABCStar application specific integrated circuits (ASICs), a controller and a power board [110].

The aim of the qualification task project was to attempt to quantify the effects of thermal variation on the ABC130 strip ITk modules. A set of 3 thermomechanical prototype modules (TMs) were used, which are shown in Figure 4.2. They were subjected to repeated thermal cycling, with visual inspections and height measurements of the sensor and hybrid components were performed using a smartscope after each set of 10 thermal cycles.

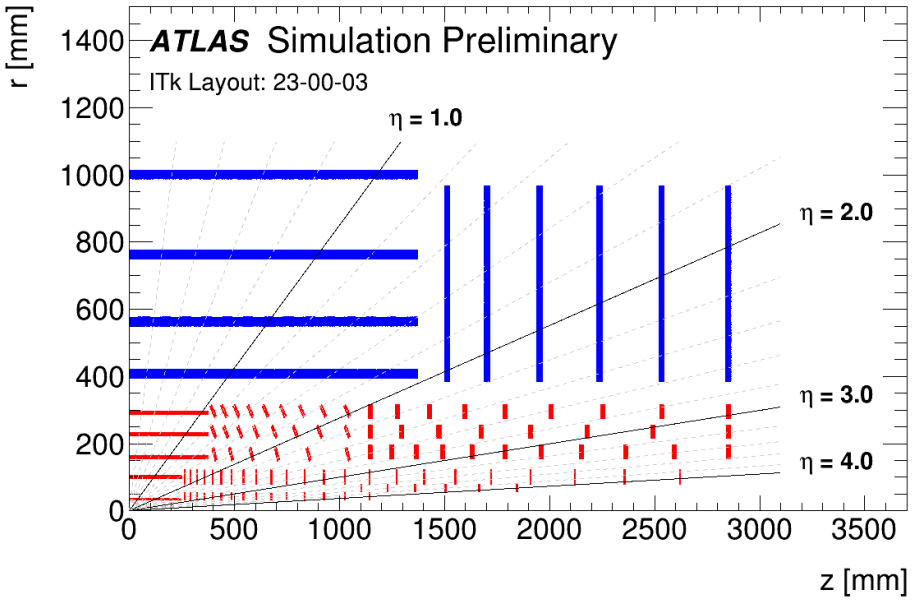

Figure 4.1: Schematic view of the active detector elements of one quadrant of the ITk. The blue outer layers represent the strip subsystem, while the red inner layers - the pixel subsystem. Taken from [111].

4.2 Experimental setup

4.2.1 Thermal cycling

The thermal cycling of the modules was performed using a Warwick prototype coldbox, a schematic of which can be seen in Figure 4.3. A Grant R5 chiller with a Grant TXF200 heating circulator [112] was used in combination with Peltier electric heat pumps in forward/reverse polarity to vary the temperature of vacuum chucks placed above them between -30 and 30°C. The vacuum provided by the vacuum chucks was used in order to achieve good thermal contact between them and the modules placed on top. The thermal cycling was repeated 100 times for each module, during which the box was constantly flushed with dry nitrogen in order to prevent condensation. The humidity inside the box was monitored using two Honeywell HIH-4000 humidity sensors [113], while the temperature of each vacuum chuck, the ethylene glycol/water cooling liquid, as well as the box's ambient temperature were monitored by a set of thermocouples.

4.2.2 Smartscope measurements

Table 4.1 shows the number of repeated measurements ("runs") after each cycling period, which usually consisted of 10 thermal cycles each. The measurements were initially done using an OGP CNC 500 smartscope [114] at the

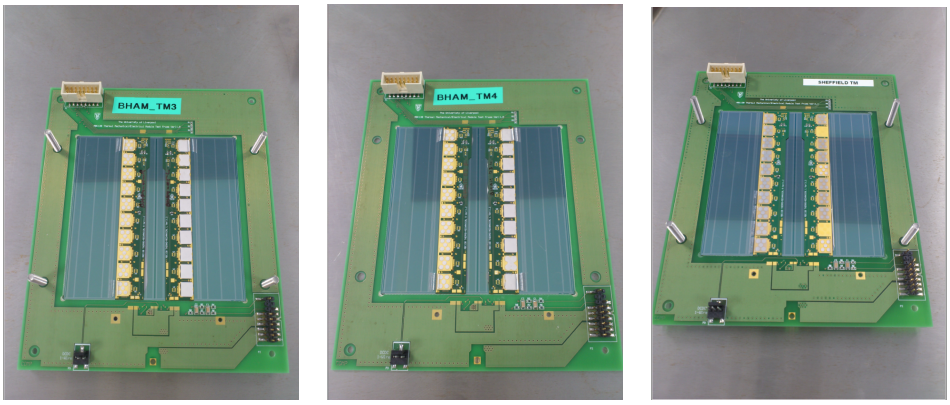

(a) Birmingham TM3 (b) Birmingham TM4 (c) Sheffield TM

Figure 4.2: Photographs of the test modules used in the study.

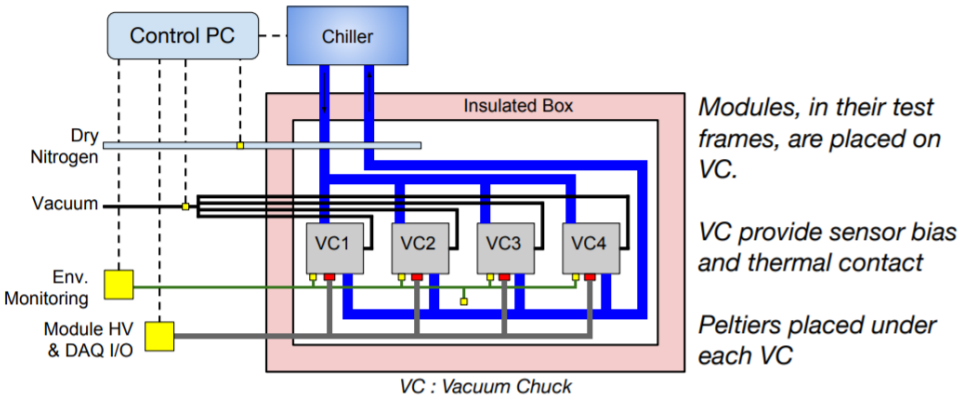

Figure 4.3: Schematic of the coldbox setup used to cycle the TMs.

University of Birmingham, and later using an identical one at the University of Warwick. Data acquisition was started both with and without the TMs being held down by a vacuum chuck. As at an early stage data involving vacuum was no longer recorded, the measurements shown in this thesis use no vacuum. For the measurements at Birmingham, the modules were being removed from their carrier frame and put on top of a vacuum chuck during the measurements. At Warwick, the modules (with their carrier frames) were placed on top of a vacuum chuck similar to the ones used in the thermal cycling coldbox (without the use of vacuum).

The smartscope was used to measure the heights (z coordinate) of points on the sensor as well as the hybrid parts of the modules. Eight points were chosen along the y coordinate of the modules (Figure 4.4), with four measuring points on the hybrids - HLABC, HLINN, HRINN, HRABC - and 4 on the sensor - SLABC, SLINN, SRINN, SRABC, where H stands for hybrid, S - sensor, ABC - chip side, INN - inner side. These 8 points were copied along the length of the hybrids (x coordinate) for a total of 11 points along each row.

Cycle	0	1	5	10	20	30	40	50	60	70	80	90	100
Sheff.	1	1	1	1	1	1	5	3	6	8	6	3	3
TM3	1	1	1	1	9	3	4	10	3	3	3	3	4
TM4	1	1	1	1	1	9	3	8	3	3	3	3	4

Table 4.1: Number of individual measurements after each cycling period of the Sheffield (Sheff.) and Birmingham TMs. The numbers in blue indicate the first measurements performed by me, while the numbers in red indicate the measurements first performed using the smartscope at the University of Warwick.

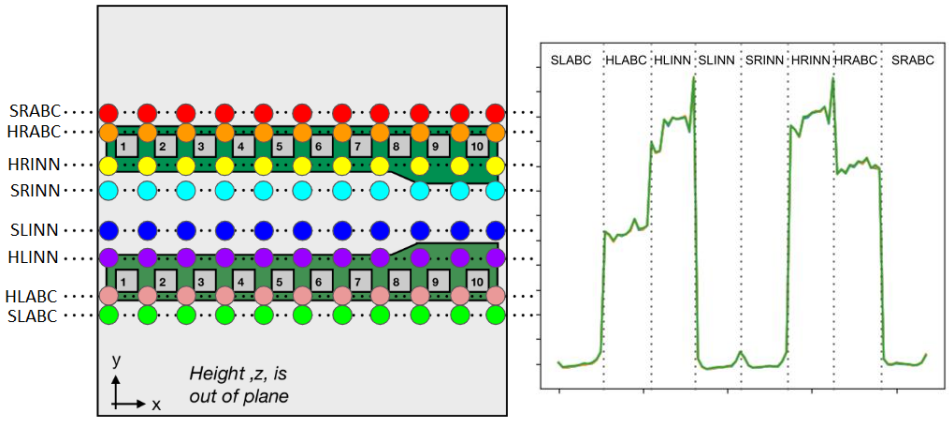

Figure 4.4: Measurement points on the hybrid and sensor components of the test modules. Each of the points along the y-axis is repeated 11 times along the x-axis. The measurements are summarised in 2-dimensional plots like the one on the right, with each row of 11 measurements being grouped together in order.

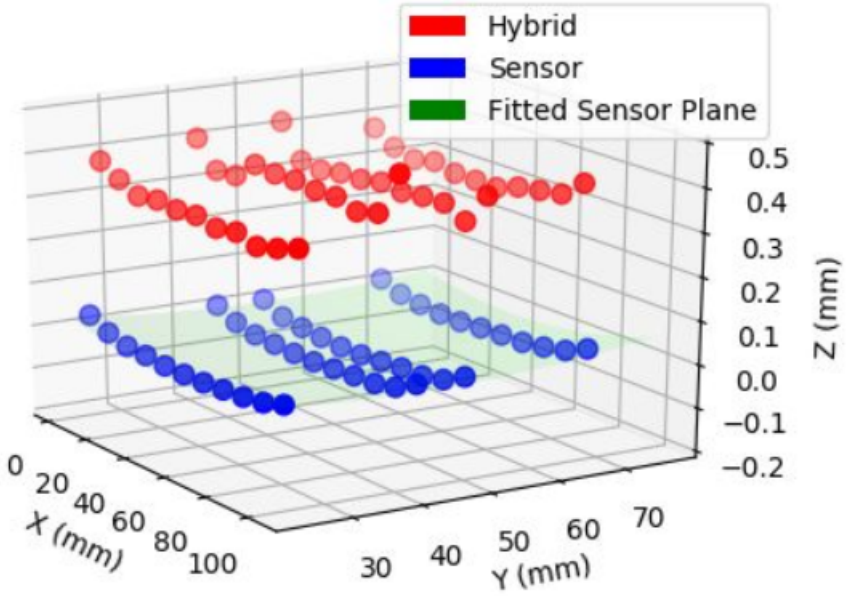

Figure 4.5: An example of a surface fit (green) to the sensor measurements (blue) of a module.

4.3 Methodology

4.3.1 Sensor shape

Studies of the shape of the sensor show variations between measurements even without thermal cycling, indicating that changes to the general shape of the sensor can be caused by transportation or displacement of the module alone [115]. Since the effects of thermal cycling on the sensor could not be isolated from the above causes, the height differences between the hybrid point measurements and the sensor plane were studied instead. For measurements from each run, the height of the sensor at the (x,y) coordinates corresponding to the hybrid (h) point measurements was estimated by fitting a polynomial function $f(x, y)$ to the sensor (s) point measurements :

$$f(x, y) = c_{ij} x^i y^j, \tag{4.3.1}$$

where $i \in [0, 6]$, $j \in [0, 2]$. An example of one such fit is shown in Figure 4.5. The value of the fit was then subtracted from all (both hybrid and sensor) measured points:

$$z^{s(h)}_{i,corr} = z^{s(h)}_{i,0} - f(x_i, y_i), \tag{4.3.2}$$

where $z^{s(h)}_{i,corr}$ are the corrected sensor and hybrid point measurements, $z^{s(h)}_{i,0}$ are the raw measurements, and $f(x_i, y_i)$ is the value of the sensor fitted function at that point, with the index i running over the number of measured points.

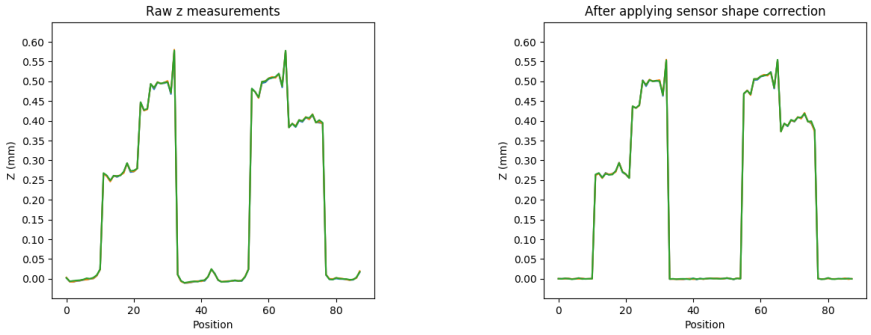

(a) Raw Sheffield measurements (b) Corrected Sheffield measurements

Figure 4.6: Example height corrections for one set of Sheffield TM measurement runs.

An example result of one such subtraction is shown in Figure 4.6.

4.3.2 Sources of uncertainty

Two sources of uncertainty in the measurements were identified - one connected to the surface function fit to the sensor points, and the other from the repeatability of the measurements.

Sensor surface subtraction

The sensor surface subtraction uncertainty at each point on the hybrids $(x_i, y_i)^h$ was estimated using the residuals of the fit to the sensor points ($z^s_{i,corr} = z^s_{i,0} - f(x_i, y_i)$) for each smartscope separately. The uncertainty was approximated by a Gaussian function fit over the residuals $z^s_{i,corr}$ from each run of each cycle period for each module. The resulting uncertainty estimations are shown in Table 4.2.

Repeatability of measurements

The uncertainty from the repeatabality of the measurements was estimated using cycles with multiple measurement runs (i.e. measurements with 1 run in the cycle period, e.g. Sheffield TM cycle period 0 was not used). For each point, the now corrected hybrid measurement $z^h_{i,corr}$ from each run was subtracted from the mean value of the corrected measurements at that point from the

smartscope	TM3 (μm)	TM4 (μm)	Sheffied TM (μm)
Birmingham	0.68	0.67	0.61
Warwick	0.76	0.86	0.67

Table 4.2: Estimation of the uncertainty due to sensor surface subtraction for all modules and both smartscope datasets.

module	smartscope	HLABC	HLINN	HRINN	HRABC
Sheffield TM	Birmingham	1.80	1.05	1.10	1.60
	Warwick	0.76	0.95	1.00	0.90
TM3	Birmingham	0.91	0.86	0.81	0.76
	Warwick	0.91	0.95	0.89	0.76
TM4	Birmingham	0.90	0.80	0.79	0.78
	Warwick	0.90	0.96	0.95	0.92

Table 4.3: Estimated uncertainties from hybrid measurement repeatability in μm.

module	smartscope	HLABC	HLINN	HRINN	HRABC
Sheffield TM	Birmingham	1.90	1.21	1.26	1.71
	Warwick	1.01	1.16	1.20	1.12
TM3	Birmingham	1.14	1.10	1.06	1.02
	Warwick	1.19	1.22	1.17	1.07
TM4	Birmingham	1.12	1.04	1.04	1.03
	Warwick	1.24	1.29	1.28	1.26

Table 4.4: Estimated total uncertainty of each hybrid row in μm.

same cycle period consisting of N runs:

$$\Delta z^{h,k}_{i,corr} = z^{h,k}_{i,corr} - \frac{\sum^{\mathrm{N}}_{j,1} z^{h,j}_{i,corr}}{N}, \tag{4.3.3}$$

where $k = 1, .., N$. The individual hybrid differences are grouped depending on which hybrid row they belong to (HLABC, HLINN, HRINN or HRABC) for both smartscopes separately. The results are shown in Table 4.3.

The errors derived from the two sources above are added in quadrature to produce the total error for each row shown in Table 4.4.

4.3.3 Investigating changes at each point

The average height value of each cycle period for each point was taken as the value of the hybrid-sensor height difference for that cycle period. The difference between each cycle period average and the first measurement was plotted, an example of which is shown in Figure 4.7. The simplest (linear) evolution was assumed and fitted to the data for three periods independently: data collected only at Birmingham, data collected only at Warwick, and a total/combined fit. The uncertainties for each point are extracted from Table 4.4 depending on which row the point belongs to.

The gradients obtained from these plots are taken and arranged into a grid in order, analogous to the physical location of the points (following SLABC, HLABC,... order), an example is shown in Figure 4.8.

Module	Outlier points
TM3	31, 32, 64, 65, 25
TM4	31, 32, 64, 65, 26, 29
Sheffield TM	11-21, 24, 31, 32, 64, 65, 57

Table 4.5: Identified outlier points for each module.

fit region	minima	maxima
	Sheff. hybrid rows (μm)	
BHAM	-9.5(-3.5)	11.4(5.4)
WW	-3.8(-3.5)	11.7(5.3)
total	-6.7(-1.3)	10.3(6.2)
	TM3 hybrid rows (μm)	
BHAM	-6.6(-6.6)	7.2(7.2)
WW	-4.4(-4.4)	2.1(2.1)
total	-2.2(-2.2)	7.5(3.9)
	TM4 hybrid rows (μm)	
BHAM	-19.1(-4.0)	10.2(6.4)
WW	-2.2(-2.2)	8.2(3.0)
total	-8.0(-3.2)	11.3(4.6)

Table 4.6: Minima and maxima of expected hybrid height change (gradient $\times$ 100 cycles) with (without) outlier points.

4.4 Results

Certain points were observed to have an unusually large gradient compared to neighbouring points, e.g. common points at one end of the hybrid rows, Figures 4.9-4.11.

A cause for this could be electrical components in the vicinity affecting the measurements. In addition, the entire Sheffield TM HLABC row has negative gradients for all of its points, in combination with its higher uncertainty seen in Table 4.4, and a discontinuity between the Birmingham and Warwick measurements. This could be caused by the different light levels used during the Birmingham and Warwick data taking due to focusing issues. Example plots of these effects are shown in Figure 4.12.

As there are discrepancies between the Birmingham and Warwick measurements and the uncertainties are not well understood at these module points, we consider results including those points and excluding them. All of the outlier points for each module are listed in Table 4.5. The minima and maxima of the expected change after 100 cycles for each row of each module are shown in Table 4.6, while the means and the standard deviations of the distributions of expected changes in hybrid point height for each module are shown in Table 4.7.

Quantity	TM3 (μm)			TM4 (μm)			Sheffield (μm)		
data	Bham	Ww	total	Bham	Ww	total	Bham	Ww	total
mean	2.5	-0.3	1.5	0.5	0.8	1.4	3×10^{-6}	0.3	1.3
σ	2.7	1.6	2.0	4.0	2.0	2.4	4.8	3.0	3.1

Table 4.7: Combined expected change in hybrid-to-sensor height after 100 cycles.

4.5 Conclusions

Three ABC130 TMs were used to investigate possible effects of repeated temperature variation. While undergoing 100 thermal cycles between -30 and 30°C, no effects (cracks, distortions, breaks, peel off of the hybrid from the sensor) were observed by eye. With estimated smartscope measurement sensitivity of 1-2 μm, the changes measured in the difference between the sensor surface and the hybrids do not exceed 10 μm over 100 thermal cycles when excluding the outlier points listed in Table 4.5. These conclusions are expected to be applicable to the newer ABC130Star modules as well.

4.6 Caveats

The following caveats in the above analysis are identified:

- The first entry for the determination of the gradients is the measurement performed after the first cycle. The measurements before any cycling ("precycle") are discarded as they are suspected to have been performed with the modules vacuumed down during the measurements.
- The Warwick smartscope camera could not focus on some of the points using the same routine options used by the Birmingham smartscope - in order to remedy this, a correction to the light levels in measurements of whole rows was introduced.
- The coordinate system used by the smartscope routine is determined by the selection of 3 points by the user (example shown in Figure 4.13), introducing an uncertainty not taken into account in this analysis directly. For future independent studies, it is possible to program the smartscope to locate shapes, like the intersection of two lines or the corners of the module components, automatically, thus reducing this uncertainty.

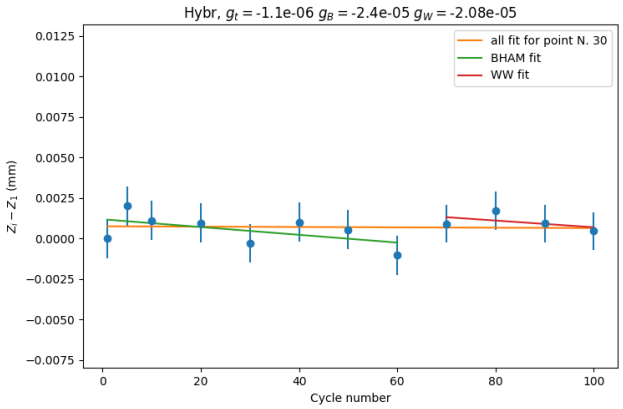

Figure 4.7: Example plot of the hybrid-sensor height "evolution" as a function of number of thermal cycles.

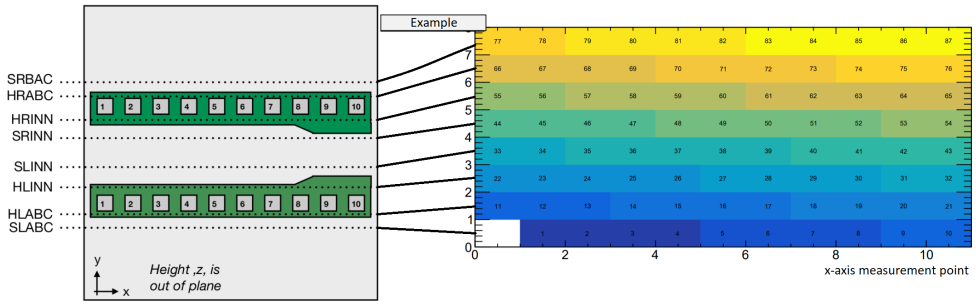

Figure 4.8: Example mapping of measurement points onto gradient grid figure. The z represents the gradient at that point (point number on this plot).

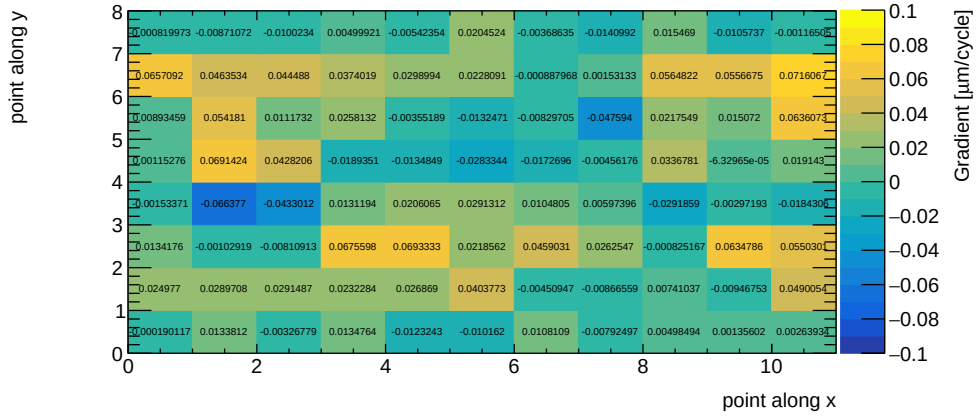

(a) TM3

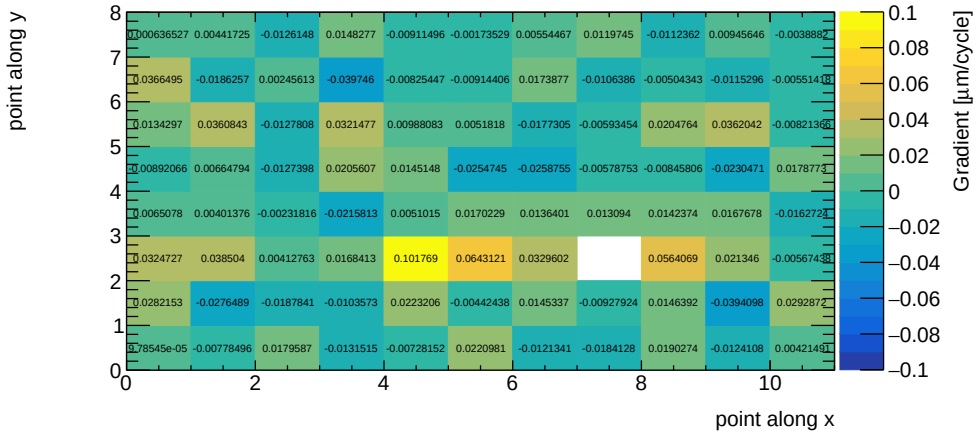

(b) TM4

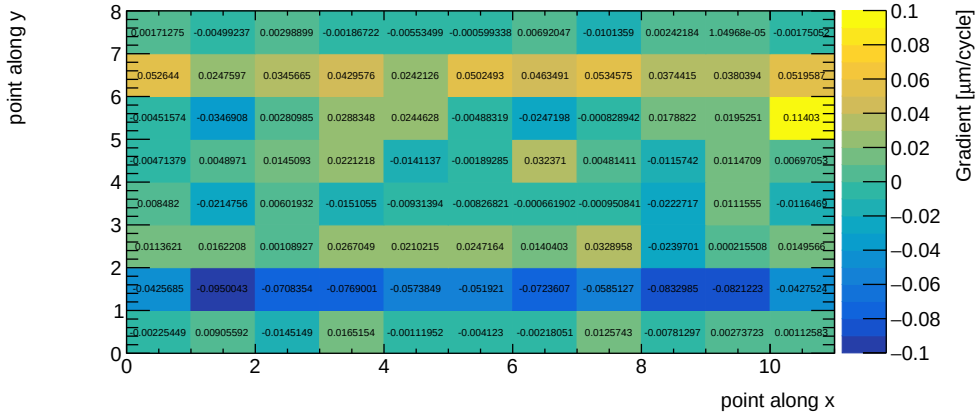

(c) Sheffield

Figure 4.9: Gradients of fitted linear models to the evolution on each point of (a) - TM3, (b) - TM4, (c) - Sheffield TMs using the Birmingham measurements only.

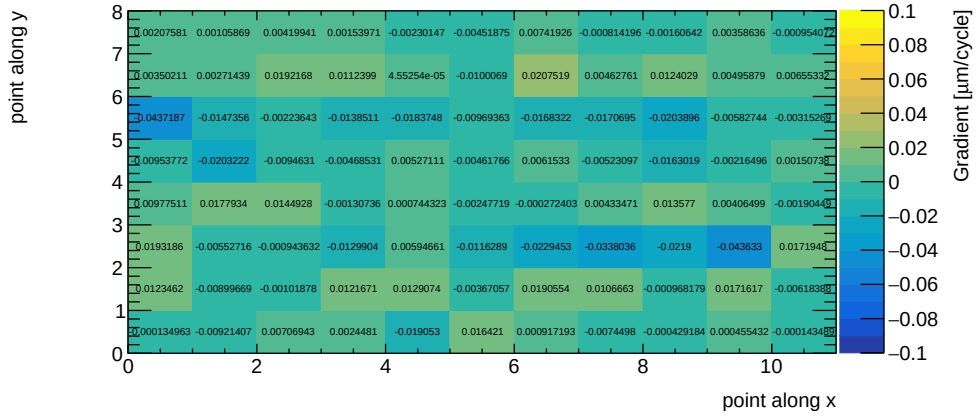

(a) TM3

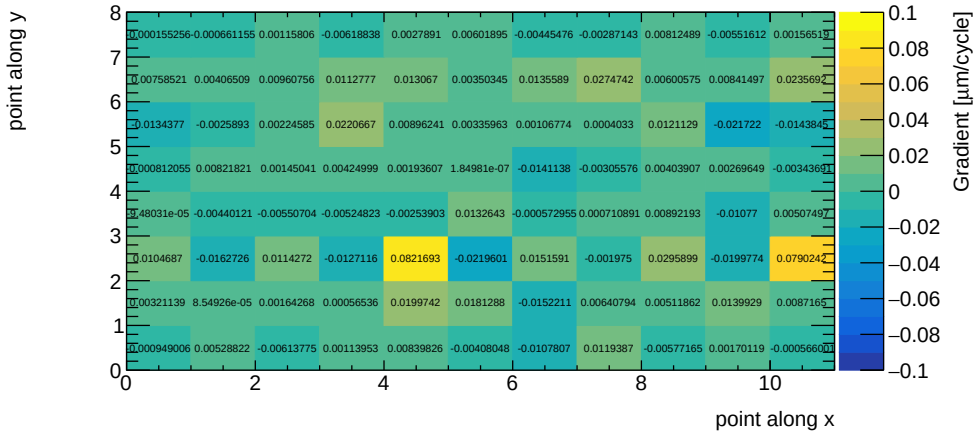

(b) TM4

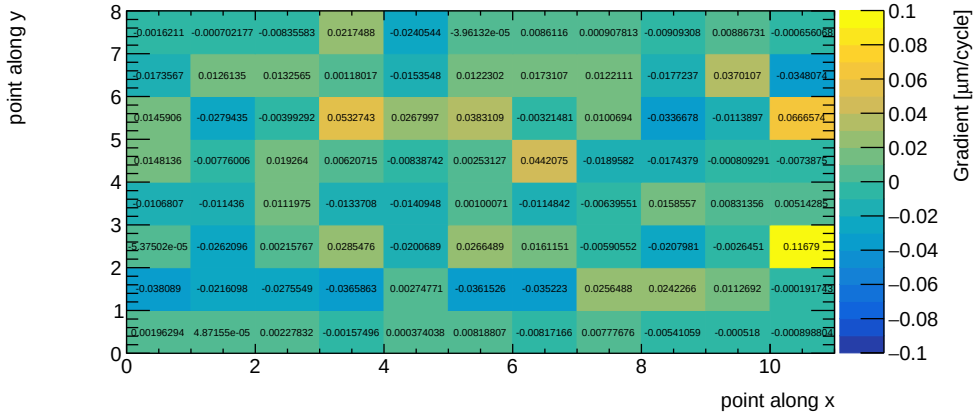

(c) Sheffield

Figure 4.10: Gradients of fitted linear models to the evolution on each point of (a) - TM3, (b) - TM4, (c) - Sheffield TMs using the Warwick measurements only.

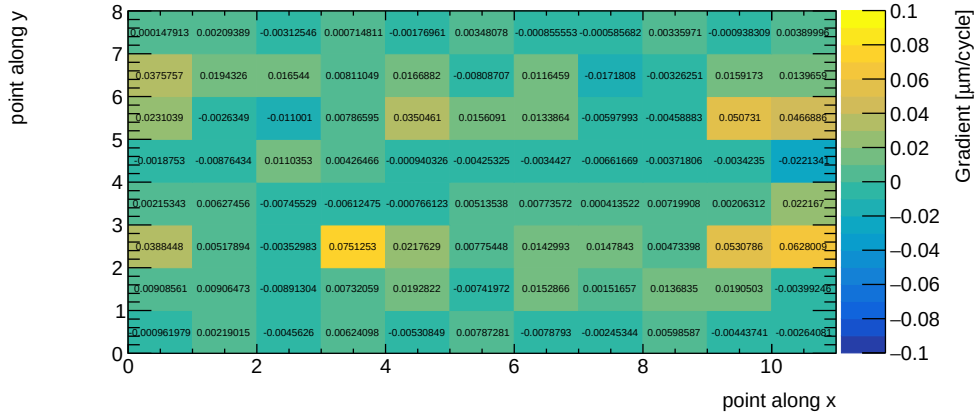

(a) TM3

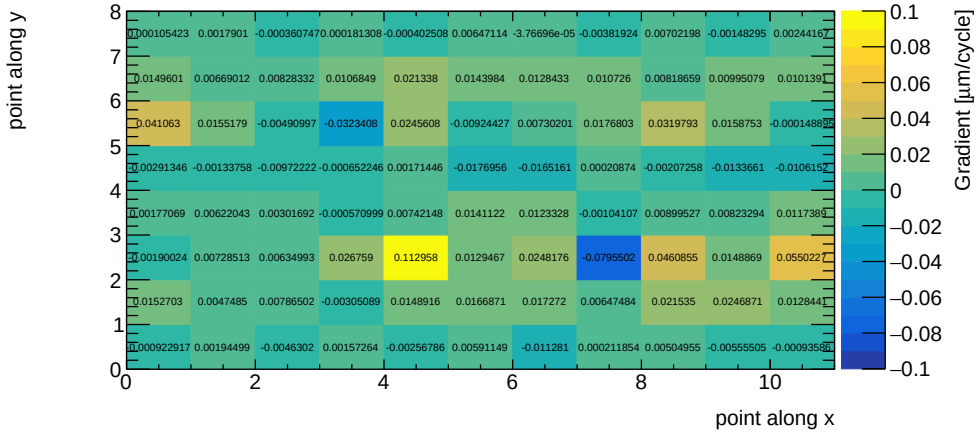

(b) TM4

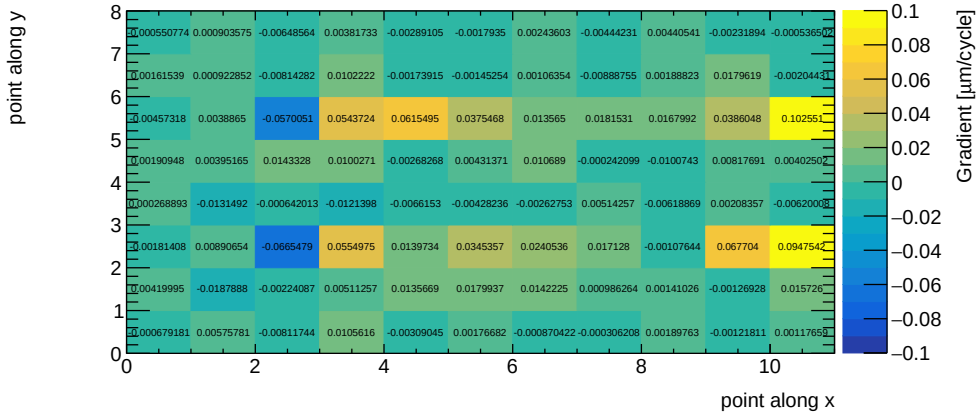

(c) Sheffield

Figure 4.11: Gradients of fitted linear models to the evolution on each point of (a) - TM3, (b) - TM4, (c) - Sheffield TMs using all measurements.

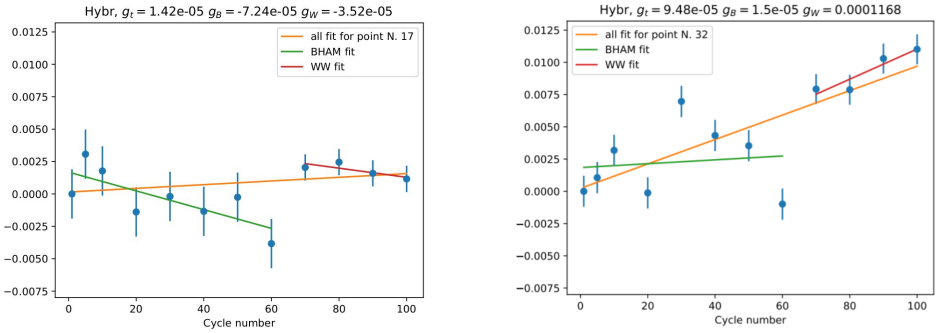

(a) HLABC example

(b) HLINN endpoint

Figure 4.12: Example height "evolution" plots of outlier Sheffield TM hybrid points; (a) - example point from HLABC row; (b) - endpoint of HLINN row.

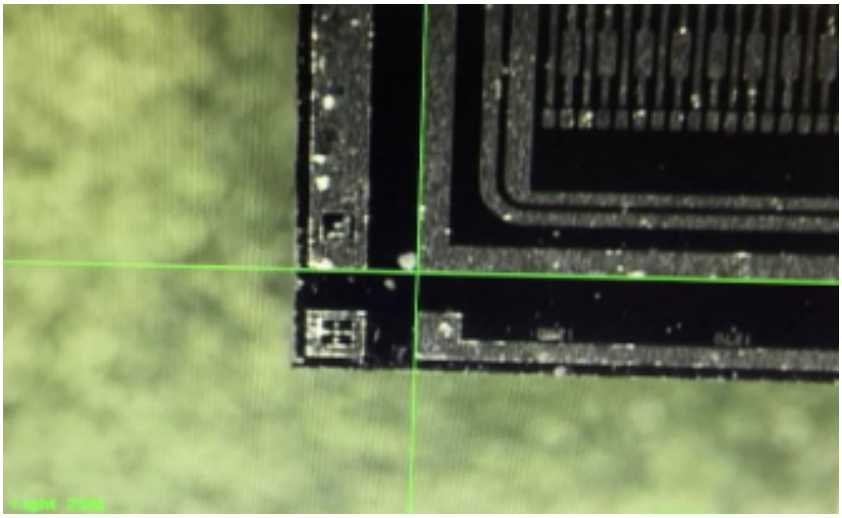

Figure 4.13: Selection of the coordinate system for the smartscope routine.

Chapter 5

Analysis feasibility study and sensitivity estimate

This section summarises the feasibility study [1] carried out prior to the analysis as part of the ATLAS collaboration. The study used only resources available publicly at the time to estimate the sensitivity of the measurement of $|V_{cb}|$.

5.1 Event selection

The aim of the analysis is the use of top pair decays, in which one top decays semi-leptonically ($t \to bW^+ \to b\ell^+\nu$) with the reconstructed lepton (e or μ) serving as the tag of the event, and the other top decays hadronically ($\bar{t} \to \bar{b}W^- \to \bar{b}q_i\bar{q}_j$, with $q_i = d, s, b$ and $q_j = u, c$), Figure 5.1. The charge conjugate processes are also included, unless otherwise stated. In order to suppress non-$t\bar{t}$ backgrounds, requirements on the semi-leptonic and hadronic sides of the event are enforced. On the hadronic side, two jets are required to reconstruct the W boson mass, which, combined with a third, b-tagged jet, reconstructs the top quark mass. On the semi-leptonic top side, the neutrino four-momentum is reconstructed using the missing transverse momentum (MET) of the event and required to reconstruct the W boson mass when combined with the charged lepton. The four-momenta of the reconstructed leptonically decaying W and that of the last, b-tagged jet of the event is required to reconstruct another top quark mass. The value of $|V_{cb}|^2$ is then extracted from the ratio of the branching fractions of the events in which the hadronically decaying W produces quark flavours cb and cq:

$$|V_{cb}|^2 = \frac{\Gamma(t\bar{t} \to (b\ell^+\nu, \bar{b}\bar{c}b)}{\Gamma(t\bar{t} \to (b\ell^+\nu, \bar{b}\bar{c}q)} = \frac{\mathcal{BF}(t\bar{t} \to (b\ell^+\nu, \bar{b}\bar{c}b)}{\mathcal{BF}(t\bar{t} \to (b\ell^+\nu, \bar{b}\bar{c}q)}, \tag{5.1.1}$$

where q includes all down-type quarks (d, s, b). Since the approach requires all jets originating from the $t\bar{t}$ system to be flavour-tagged, it is required that

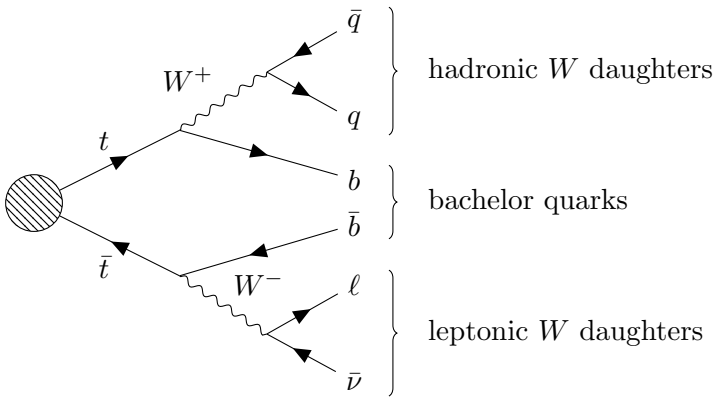

Figure 5.1: Feynman diagram of the $t\bar{t}$ topology of interest in the analysis presented in this thesis. The CKM matrix element V_{cb} is involved in the specific decay $W^+ \to c\bar{b}$ of the hadronic side W boson. The jets assigned to be stemming from the top quark decays are labeled as bachelor jets. The charge conjugate process is also included.

Quantity	Symbol	Origin of value	Approx. value
$t\bar{t}$ cross-sec.	$\sigma_{t\bar{t}}$	[116, 117]	8.5×10^5 fb
Integrated lum.	$\mathcal{L}$	Time-variable	140 fb^{-1}
Branching frac.	$\mathcal{BF}$	$2 \times (\frac{2}{9}) \times (\frac{2}{3}) \times \frac{1}{2}$	0.15
Lepton tag eff.	ϵ_{lep}	-	-
Preselection eff.	ϵ_0	[117, 118] Incl. ϵ_{lep}, not ϵ_B^2	0.10
Preselected cross-sec.	-	$\sigma_{t\bar{t}} \times \mathcal{BF} \times \epsilon_0$	1.3×10^4 fb
b-tagging eff.	ϵ_B	t daughter b-jet	tunable
c-tagging eff.	ϵ_c	W daughter c-jet	tunable
b-tagging eff.	ϵ_b	W daughter b-jet	tunable

Table 5.1: Input quantities for estimation of sample magnitudes for LHC Run 2. The b-jets originating from the top quark decays and the subsequent W boson decays are kept as separate quantities to allow for variation due to different kinematics and in order to tune them separately for the sensitivity optimisation.

all jets are resolved - large jets (with jet parameter $R = 1.0$) which are likely a result of multiple merged jets are not considered. Using the ratio given in Equation 5.1.1 allows for the cancellation of the dependence of the result on some of the leading tagging uncertainties.

5.2 Estimate of event yields

The event yield corresponding to the full LHC Run 2 conditions is estimated using the quantities summarised in Table 5.1. The preselection efficiencies quoted by the ATLAS experiment at 8 TeV [118] and by the Compact Muon Spectrometer (CMS) experiment at 13 TeV [117] are 0.17 and 0.13 respectively. Since the selection regions are slightly different, the value in this feasibility

study is set to a more conservative value of 0.10. Different b-tagging working points (WPs) exist, corresponding to different cuts on the b-tagger outputs (see Section 3.3.7) and thus resulting in different efficiencies and mistag rates for identifying a jet as b-tagged. The tagging efficiencies are left as tunable free parameters, the values of which are determined by the pair of b-tagging and c-tagging WPs which minimise the uncertainty of the $|V_{cb}|$ measurement. The quantities of Table 5.1 are used to define half the number of the reconstructed semi-leptonic $t\bar{t}$ events (in which the W boson decays into charm) with both b-jets originating from the top quark decays (the bachelor jets) being b-tagged:

$$\mathcal{D}_0 = \sigma_{t\bar{t}}\ \mathcal{B}\mathcal{F}\epsilon_0\mathcal{L}\epsilon_B^2 = 1.3 \times 10^4 \mathcal{L}\epsilon_B^2, \tag{5.2.1}$$

and the number of reconstructed signal ($W \to cb$) events:

$$S = \mathcal{D}_\prime\epsilon_c\epsilon_b|V_{cb}|^2\ \sim 23\mathcal{L}\epsilon_B^2\epsilon_c\epsilon_b. \tag{5.2.2}$$

The 2 b-tagged jet requirement suppresses poorly reconstructed events in which there is a kinematic coincidence in which a jet originating from the hadronic W boson decay is swapped with a jet directly produced by the top quark decay. In $t\bar{t}$ events with correctly assigned jets, a source of background originates from incorrectly flavour-tagged W daughter jets. The magnitude of this effect is dependent on the flavour tagging efficiencies and mistag rates. For example, the number of reconstructed events in which the W boson daughter jets are identified as (cb) receives contributions from the true $W \to cb$ events (the signal of the analysis, $\mathcal{S}$), but also from the background channel $W \to cl$, where l is mistagged as b (with probability f_{lb}), denoted by $\mathcal{B}_1$. There is also contribution from the double mistag of c to b and l to c (with probability $f_{cb}f_{lc}$), denoted by $\mathcal{B}_2$. The number of reconstructed (cb) channel events is then given by:

$$\mathcal{N}_{cb} = \mathcal{S} + \mathcal{B} = \mathcal{S} + \mathcal{B}_1 + \mathcal{B}_2 \simeq \mathcal{D}_0(\epsilon_c\epsilon_b|V_{cb}|^2\ + \epsilon_c f_{lb} + f_{lc}f_{cb}). \tag{5.2.3}$$

Contributions to $\mathcal{N}_{cb}$ from the true ll channel are suppressed by a factor of $2f_{lc}f_{lb}$. Jet flavour mistag rates also govern the magnitude of reconstructed channels such as (cc) or (bb), for which true decays ($W \to cc$, $W \to bb$) are not allowed in the Standard Model (SM). The remaining channels used in this feasibility study and their leading and subleading contributions are summarised in Equations 5.2.4 through 5.2.6.

$$\mathcal{N}_{lc} \simeq \mathcal{D}_0[\epsilon_c(1 - 2f_{lc}) + 3f_{lc}] \tag{5.2.4}$$

$$\mathcal{N}_{cc} \simeq \mathcal{D}_0\epsilon_c(f_{lc} + f_{bc}|V_{cb}|^2\ + \frac{f_{lc}^2}{\epsilon_c}) \tag{5.2.5}$$

$$\mathcal{N}_{lb} \simeq \mathcal{D}_0[f_{cb} + f_{lb}(3 - \epsilon_c)]. \tag{5.2.6}$$

5.3 Estimate of the measurement sensitivity

Measuring the number of events in the $\mathcal{N}_{ij}$ channels and rearranging Equations 5.2.3 to 5.2.6, the following quantities can be extracted from the system of equations, provided f_{lb}, ϵ_b and f_{bc} are introduced as external input from other flavour tagging studies:

$$\epsilon_c = \frac{\mathcal{N}_{lc} - 3f_{lc}\mathcal{D}_0}{\mathcal{D}_0(1 - 2f_{lc} - f_{lb})} \tag{5.3.1}$$

$$f_{lc} \simeq \mathcal{R}'_{cc}\left(1 - \frac{\mathcal{R}'_{cc}}{\epsilon_c}\right) \tag{5.3.2}$$

$$f_{cb} = \epsilon_c\left[\frac{\mathcal{N}_{lb}}{\mathcal{D}_0} - f_{lb}(3 - \epsilon_c)\right], \tag{5.3.3}$$

where

$$\tag{5.3.4}$$

$$\mathcal{R}'_{cc} = \frac{\mathcal{N}_{cc}}{\mathcal{D}_0\epsilon_c} - f_{bc}|V_{cb}|^2 \ , \tag{5.3.5}$$

and finally

$$|V_{cb}|^2 \ = \frac{\mathcal{N}_{cb} - \mathcal{D}_0 f_{lb}\epsilon_c - \mathcal{D}_0 f_{lc} f_{cb}}{\mathcal{D}_0\epsilon_b\epsilon_c}, \tag{5.3.6}$$

which can be represented as the expression

$$|V_{cb}|^2 \ \simeq \frac{(\mathcal{S} + \mathcal{B}) - \mathcal{B}_1 - \mathcal{B}_2}{\mathcal{D}_0\epsilon_b\epsilon_c}. \tag{5.3.7}$$

In addition to the "standard" statistical error evaluated before the background subtraction $\propto \sqrt{\mathcal{S} + \mathcal{B}} \sim \sqrt{\mathcal{N}_{cb}}$, the uncertainties due to the imperfect subtraction of the background components $\mathcal{B}_1$ and $\mathcal{B}_2$ are parameterised as fractional uncertainties in their magnitudes - $\delta_{\mathcal{B}_i}\mathcal{B}_i$. While statistical uncertainty of the denominator is found to be negligible compared to the others, a systematic contribution due to the uncertainty in the b-tagging efficiency is introduced by a fractional uncertainty on ϵ_b, δ_{ϵ_b}. The fractional error on the measurement is found to be given by Equation 8.5 in [1]:

$$\frac{\Delta|V_{cb}|^2}{|V_{cb}|^2} = \frac{1}{\epsilon_B\sqrt{23\mathcal{L}\epsilon_c\epsilon_b}} \oplus \frac{[f_{lb} + f_{lc}\widetilde{f}_{cb}(1 + f_{lc} + \widetilde{f}_{cb})]^{\frac{1}{2}}}{\epsilon_B\epsilon_b|V_{cb}|\sqrt{23\mathcal{L}\epsilon_c}} \oplus \delta_{\epsilon_b} \oplus \frac{f_{lb}}{\epsilon_b|V_{cb}|^2}\delta_{\mathcal{B}_1}, \tag{5.3.8}$$

Quantity	Approx. value	Approx. relative uncertainty
	b-tagging	
ϵ_b	0.55 [119]	$2-9\%$ [120]
f_{cb}	3×10^{-2} [119, 121]	17% [121]
f_{lb}	6×10^{-4} [119, 122]	$15-30\%$ [122]
	c-tagging	
ϵ_c	0.25 [123]	unavailable
f_{bc}	0.25 [123]	unavailable
f_{lc}	3×10^{-3} [123]	unavailable

Table 5.2: Approximate efficiencies and mistag rates of the tightest available regions in b-tagging and c-tagging receiver operating characteristic (ROC) curves published by the ATLAS experiment. The listed relative uncertainties do not necessarily correspond to the exact working point quoted, but to the closest one available. The ranges of values of the relative uncertainties reflect their dependence on the jet kinematics.

where the first two terms are statistical uncertainties, the last two terms are systematic uncertainties and $\widetilde{f}_{cb} = f_{cb}/\epsilon_c$. The uncertainty of the measurement was estimated using the tagging efficiencies and mistag rates published by the ATLAS experiment, shown in Table 5.2 and the assumption $\delta_{\mathcal{B}_1} = 3\delta_{\epsilon_b} = 3$ [1], yielding the result:

$$\frac{\Delta|V_{cb}|}{|V_{cb}|} \simeq \frac{1}{2}(0.086 \oplus 0.087 \oplus 0.033 \oplus 0.061) \simeq 0.07, \tag{5.3.9}$$

where the order of the terms in Equation 5.3.8 is preserved.

The major goal of the research presented in this thesis was to update this published approach using realistic analysis techniques, based in the first instance on full Monte Carlo simulation studies.

Chapter 6

Analysis methodology

The simple analysis approach outlined in the feasibility study (Chapter 5) did not take into account QCD effects or realistic background events stemming from non-$t\bar{t}$ and non-signal $t\bar{t}$ processes, with assumed efficiencies taken from previous $t\bar{t}$ cross-section measurements. Because of this, there was a need for the development of a bespoke analysis methodology to fully take into account the requirements of the measurement in the realistic ATLAS environment. This was performed using a full Monte Carlo simulated sample, corresponding to the data-taking conditions of ATLAS during LHC Run 2 operations.

This chapter describes the refined selection criteria and sensitivity extraction method used in the final form of the analysis. They were the conclusion of a series of tests and optimisation procedures of several methods, with only the latest selection configuration presented here. The analysis is kept "blinded" - the extraction of the value of $|V_{cb}|$ in data is not performed until the method is finalised.

6.1 Event preselection

This section details the object definition and the kinematic requirements imposed on them in order to produce the subset of the ATLAS Top dataset which was used in the analysis presented in this thesis.

6.1.1 Preselection criteria

As the only decay channel in the analysis presented in this thesis is the ℓ+jets channel (Figure 5.1), single lepton triggers are utilised, with the requirement that the reconstructed lepton has $|\eta| < 2.5$ and $p_T > 25$ GeV. Table 6.1 summarises the triggers employed during the different years of Run 2 data taking.

Muons are selected using the *Medium* identification working point (WP), which is satisfied only by IO and CB muons (Section 3.3.5) with the requirement

year	object	global triggers
2015	electrons	e24_lhmedium_L1EM20VH or e60_lhmedium or e120_lhloose
	muons	mu20_iloose_L1MU15 or mu50
2016-2018	electrons	e26_lhtight_nod0_ivarloose or e60_lhmedium_nod0 or e140_lhloose_nod0
	muons	mu26_ivarmedium or mu50

Table 6.1: Global triggers used for the different data taking periods of Run 2.

on the charge-momentum significance (defined in Equation 3.3.1) of $\varsigma_{q/p} < 7$. In addition, the muon is separated from nearby event activity by the *FCTight_FixedRad* isolation criterion (tight fixed cut isolation with fixed radius at high p_T), corresponding to

$$E_T^{\text{topocone20}}/p_T^{\mu} < 0.15 \text{ and } \begin{cases} p_T^{\text{varcone30}}/p_T^{\mu} < 0.04 & \text{if } p_T^{\mu} < 50 \text{ GeV} \\ p_T^{\text{cone20}}/p_T^{\mu} < 0.04 & \text{if } p_T^{\mu} \geq 50 \text{ GeV}. \end{cases} \tag{6.1.1}$$

Electrons are required to satisfy the *TightLH* cut on the likelihood discriminant, in addition to the electron requirements of $E/p < 10$ and the primary track should have $p_T > 2$ GeV [75]. They are required to be within the region $|\eta_{\text{cluster}}| < 2.47$, excluding the transition region between the barrel and end-cap calorimeters in $1.37 < |\eta_{\text{cluster}}| < 1.52$.

Jets are reconstructed using the anti-k_T particle flow (PFlow) algorithm with small radius parameter ($R = 0.4$). Since every individual jet originating from the quarks of the $t\bar{t}$ decay is required to be flavour tagged for the analysis, fully resolved events (no merged jets) are selected for. Events are thus required to have at least 4 jets in the preselection.

***b*-tagging** is implemented using the tightest available and calibrated WP (*FixedCutBEff 60*, $S_{DL1r} > 4.565$), corresponding to an efficiency of $\epsilon_b \sim 62\%$. Events are required to contain at least 1 b-tagged jet - a more loose requirement than the 2b-tagged jet requirement in the feasibility study, Chapter 5.

***c*-tagging** is implemented using the WP defined in Section 3.3.7. No restriction on the number of c-tagged jets is enforced.

Tau reconstruction is used only as a veto for events - the preselected samples are required to have 0 reconstructed taus using the *Medium* WP [95].

As the signal (and some background) events contain exactly one neutrino, its transverse momentum is equated to the missing transverse momentum (MET) of the event.

6.1.2 Preselection $t\bar{t}$ event yields

A summary of the jet multiplicity (N_j) in $t\bar{t}$ events passing the preselection criteria (Section 6.1) is shown in Figure 6.1. Since the origin of the additional

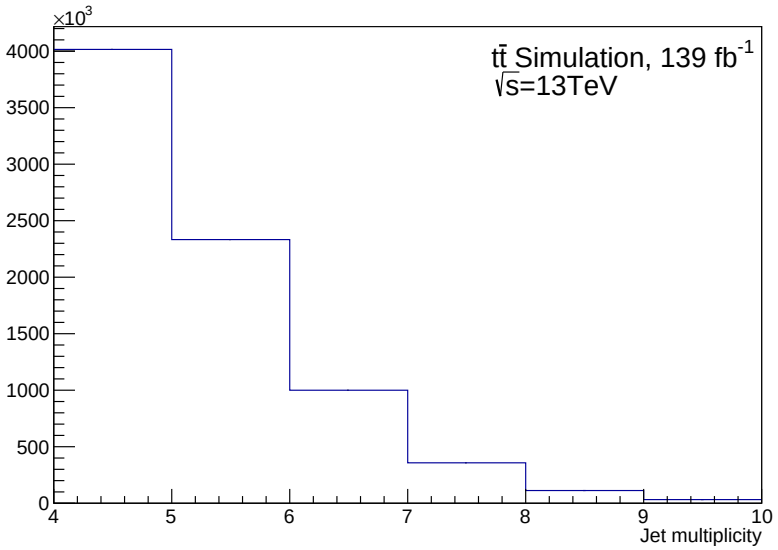

Figure 6.1: Distribution of the numbers of jets in the $t\bar{t}$ events satisfying the preselection criteria introduced in Section 6.1.

jets in $N_j > 4$ jet events (as well as $N_j = 4$ events in which a jet originating from the $t\bar{t}$ decay is not reconstructed in the presence of another jet) is unknown, reconstruction of the $t\bar{t}$ system is ambiguous - e.g. in an $N_j = 5$ event with the additional jet originating from pile-up, the extra jet should not be considered in the reconstruction of the $t\bar{t}$ system, as they arise independently of it. Meanwhile, final state radiation (FSR) jets contain a fraction of the energy of the $t\bar{t}$ system, and must be combined with other jets in order to accurately reconstruct elements of the $t\bar{t}$ system. Optimisation of event selection and reconstruction with $N_j > 4$ can lead to reduced statistical uncertainty of the $|V_{cb}|$ measurement, but they are not considered in this iteration of the analysis and are left to its future incarnations.

6.2 Additional event selection

The following section describes the additional requirements imposed on the events passing the basic preselection requirements listed above. These conditions were imposed in order to reduce background events arising from non-$t\bar{t}$ processes, non-signal $t\bar{t}$ decay modes, as well as poorly reconstructed events.

6.2.1 Kinematic χ^2 variable

Events satisfying the preselection criteria are also required to satisfy a cut on a kinematic χ^2 variable, generated using the Monte Carlo (MC) simulation sample for semi-leptonic $t\bar{t}$ events, and a cumulative distribution function (CDF) cut of the same χ^2, optimised by the background rejection in MC.

A subset of the semi-leptonic $t\bar{t}$ MC events was used to define the "true" semi-leptonic $t\bar{t}$ decay kinematics. This was achieved by developing a matching algorithm between the particle level (generated quarks and leptons) and the truth level (reconstructed objects without any detector effects), with the truth objects then matched with the reconstruction level objects (detector effects applied). The matching requires that for each event, a lower-level object (particle level for the first match, truth level for the second match) is matched with a higher-level object (truth level for the first match, reconstruction level for the second match) which has not been matched to any other lower-level object. For the leptons, the matching is successful if the angular distance between the lower-level lepton and the higher-level lepton satisfies $\Delta R < 0.1$. For jets, the permutation which results in the lowest $\Delta R = \sum \Delta R_{ij}$ is selected, where the sum is over the four pairs of a lower-level jet (or quark) and a higher-level jet with angular distance ΔR_{ij} between them. The ΔR_{ij}s are then sorted in ascending order, with values required to satisfy stricter requirements for the closest pairs - $\{0.07, 0.2, 1, 1\}$. The truth jets which are assigned to the b-quarks from the top decays are required to contain exactly 1 ghost B-hadron each. The events which are parton→truth→reconstruction matched (or truth-matched sample) are used to define the kinematic χ^2 construction described in the following subsections.

Leptonic side contribution to χ^2 variable

The leptonic side of the event contributes to the χ^2 variable with the reconstructed semi-leptonically decaying top quark, as well as the reconstructed W mass.

The neutrino is the only expected particle from the hard scatter to not be detected and its transverse momentum is equated to the missing transverse momentum of the event. Figure 6.2 shows the difference between the absolute magnitudes of the reconstructed $\vec{p}_T^{\,\text{miss}}$ and the parton level (generator level) neutrino momentum, p_T^{neutrino}, as a function of the event's reconstructed charged lepton momentum, $p_{T,\ell}^{\text{reco}}$, for each event in the truth-matched sample. A correction to the reconstructed $\vec{p}_T^{\,\text{miss}}$ is applied as a function of $|p_{T,\ell}^{\text{reco}}|$. The effect of it is shown in Figure 6.3, which is a profile onto the x-axis of Figure 6.2.

In order to reconstruct the longitudinal momentum of the neutrino, p_z, the

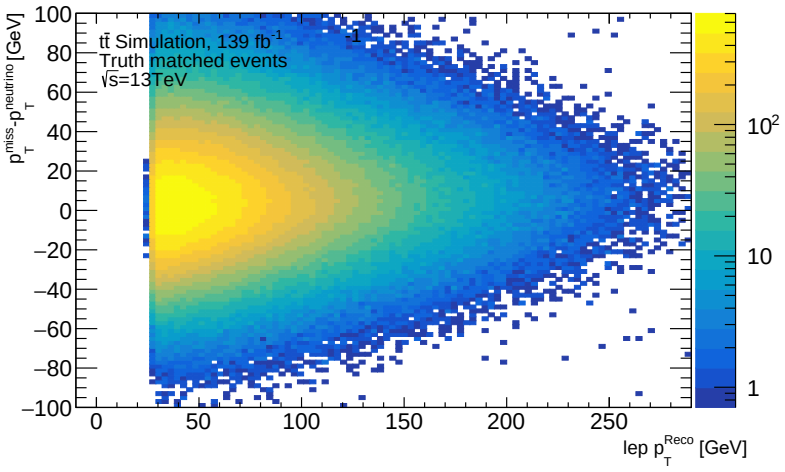

(a) Reconstructed and generated $|\vec{p}_T^{\,\text{miss}}|$ difference as a function of $|p_{T,\ell}^{\text{reco}}|$

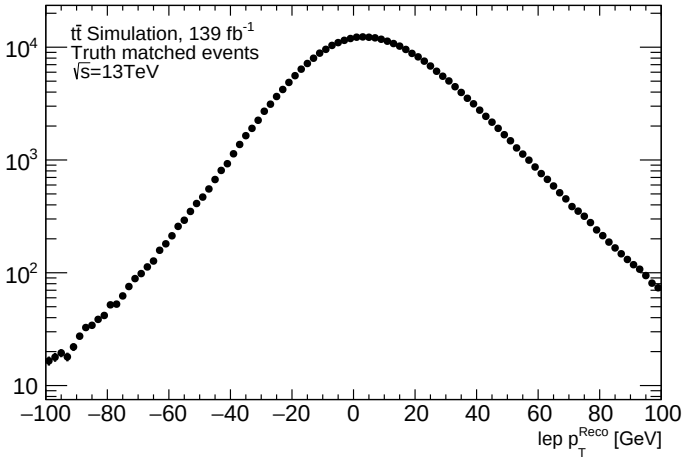

(b) Projection of (a) onto the y-axis

Figure 6.2: (a) - two-dimensional scatter histogram of $|\vec{p}_T^{\,\text{miss}}| - |\vec{p}_{T,\nu}^{\,\text{ptn}}|$ against reconstructed charged lepton transverse momentum $|p_{T,\ell}^{\text{reco}}|$ and (b) - its projection onto the y-axis - (b).

requirement of the sum of the neutrino and charged lepton 4-momenta, p^μ and q^μ, to reconstruct the W mass ($m_W = 80.379$ [9]) is enforced:

$$(p^\mu + q^\mu)^2 = m_W^2. \tag{6.2.1}$$

$$\Rightarrow 2p^\mu q_\mu = m_W^2 - m_\ell^2 \tag{6.2.2}$$

$$\Rightarrow PQ - \vec{p}\cdot\vec{q} = \frac{m_W^2 - m_\ell^2}{2}. \tag{6.2.3}$$

With the assignment $A = (m_W^2 - m_\ell^2)/2 + p_x q_x + p_y q_y$ and the use of the transverse components of the energies P and Q, $P_T = \sqrt{P^2 - p_z^2}$ and $Q_T =$

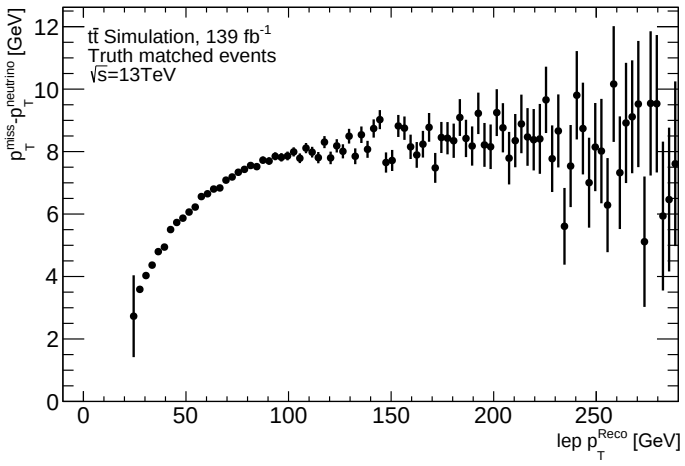

(a) Uncorrected profile

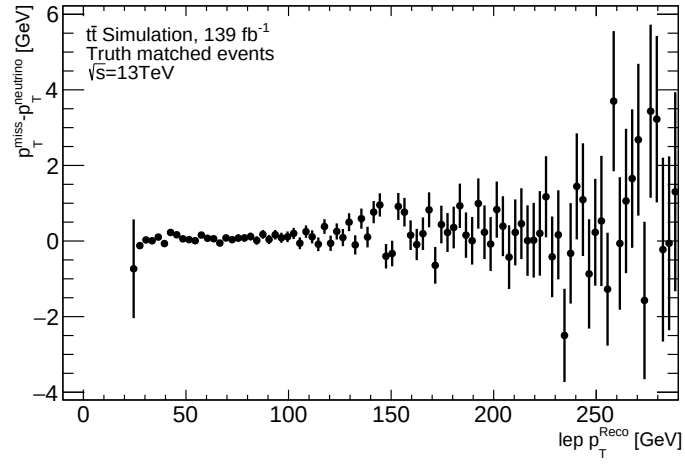

(b) Corrected profile

Figure 6.3: Profile along the x-axis of the uncorrected and corrected difference $|\vec{p}_T^{\,\text{miss}}| - |\vec{p}_{T,\nu}^{\,\text{ptn}}|$ against $|p_{T,\ell}|$.

$\sqrt{Q^2 - q_z^2}$, the equation takes the form

$$p_z^2 P_{0,T}^2 - 2q_z p_z A - A^2 + P^2 Q_T^2 = 0, \tag{6.2.4}$$

with the two solutions for the z-component of the neutrino momentum:

$$p_z = \frac{A}{P_T^2}\left[q_z \pm P\sqrt{1 - (P_T Q_T/A)^2}\right]. \tag{6.2.5}$$

When the equation has two different solutions (discriminant D of the quadratic equation is positive for $|A| > P_T Q_T$), the one with the smallest absolute value is chosen. In the cases where there are no real solutions ($|A| < P_T Q_T$), the

discriminant is forced to equal zero by modifying A to satisfy:

$$A = P_T Q_T. \tag{6.2.6}$$

Since $A = A(p_x, p_y, q_x, q_y, m_\ell, m_W)$, the only parameter which is not directly measured and can absorb the modification of A is m_W, resulting in an increased mass of the boson. In the cases where a shift of the boson mass is necessary, its new value is used to extract a contribution to the kinematic χ^2 variable, generated by comparing the candidate m_W value to a Gaussian distribution extracted from the truth-matched sample events, Figure 6.4 (a).

The leptonic side top mass is reconstructed by combining the leptonically decaying W boson and a candidate leptonic bachelor (originating from the semi-leptonic top decay) jet. The CDF contribution is determined by the truth-matched events' distribution of reconstructed top mass as a function of the leptonic bachelor jet energy, $E_{b_{\text{lep}}}$, Figure 6.4 (b). Projections of the top mass are made in bands of $E_{b_{\text{lep}}}$, with CrystalBall functions being fit to the resulting distributions. The parameters of the CrystalBall function[1] are then smoothed as a function of $E_{b_{\text{lep}}}$ by fitting polynomial functions to the values extracted from each band, Figure 6.5. This allows for the interpolation of a CrystalBall function for any measured energy of the jet assigned to be the bachelor, to which the reconstructed top mass can be compared to extract the contribution towards the kinematic χ^2 variable. An example of an interpolated CrystalBall function for a given energy of a jet assigned to be the leptonic bachelor is shown in Figure 6.6.

Hadronic side contribution to χ^2 variable

The template for the hadronic side was generated from the scatter plot of the reconstructed hadronic top quark and hadronic W boson masses using the truth-matched sample. The plot was centered (means along x- and y-axes set to 0) and rotated, aligning the axis which minimises the variance with the new y-axis (y'), Figure 6.7. Gaussian functions were fit to the projections onto the x' axis of different bands in y'. Similar to the leptonic side, the extracted Gaussian parameters were smoothed by polynomial fits, Figure 6.8. A total projection along y' was also fit by a Gaussian function. The Gaussian y' distribution and an example interpolated Gaussian x' distribution from the value of an event's y' are shown in Figure 6.9.

[1]The value of the parameter N, regulating the speed of the CrystalBall tail decay, is fixed to $N = 5$.

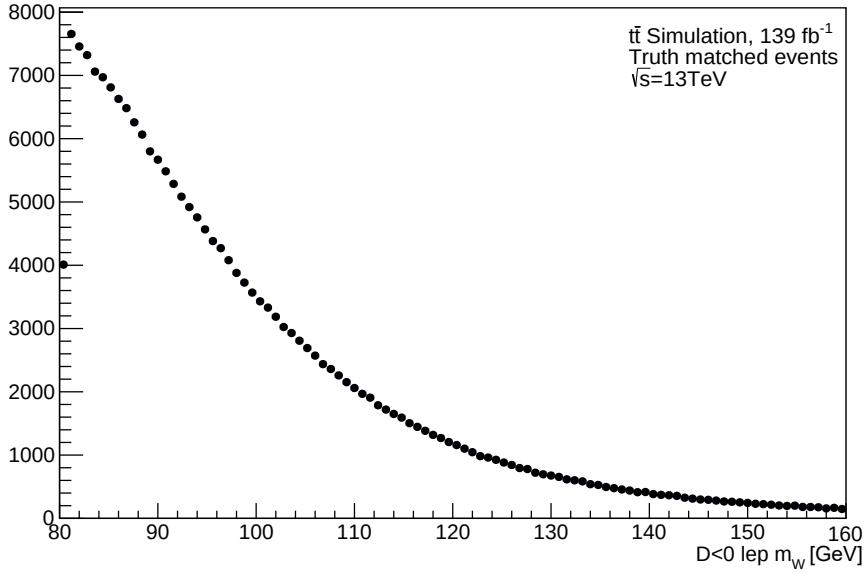

(a) $D < 0$ W mass

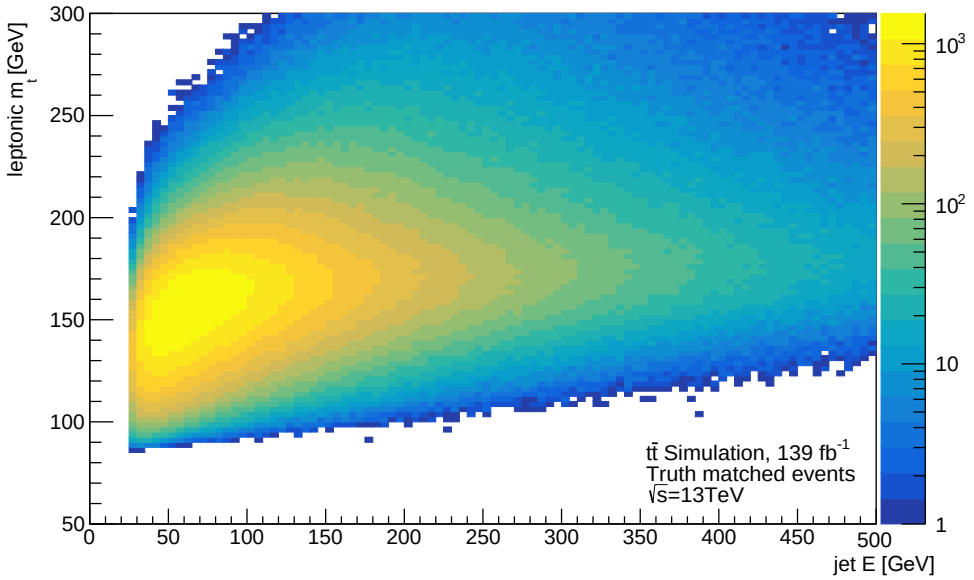

(b) reconstructed top mass against true bachelor jet energy

Figure 6.4: Leptonic side (a) - distribution of W boson mass for the cases where a correction to it is required in order to obtain a solution for the longitudinal component of the neutrino momentum. (b) - scatter plot of the reconstructed top mass and the leptonic bachelor b-jet energy of the truth-matched events. Values are in units of GeV.

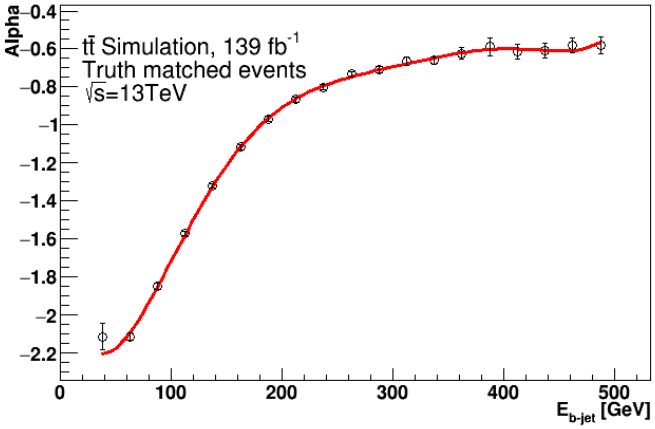

(a) alpha variation

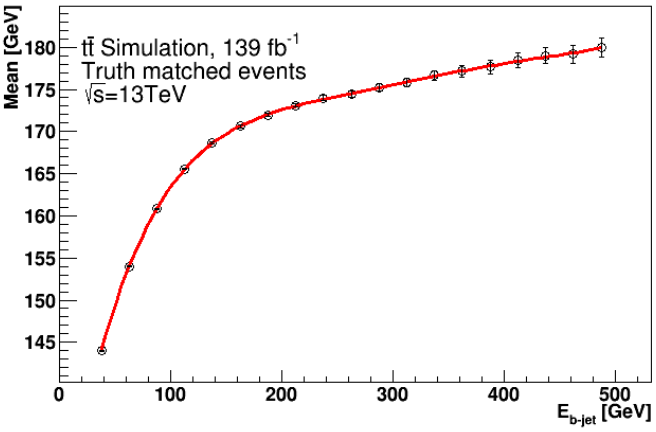

(b) mean variation

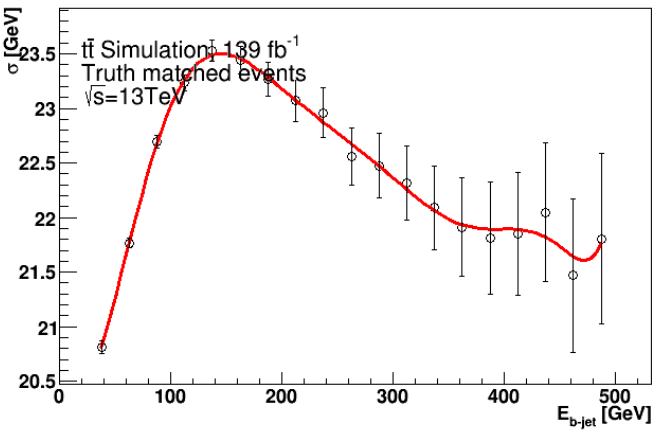

(c) standard deviation variation

Figure 6.5: Smoothing of the (a) - alpha, (b) - mean and (c) - standard deviation parameters, of the CrystalBall function fits over bands of different leptonic b-jet candidate energy in Figure 6.4 (b).

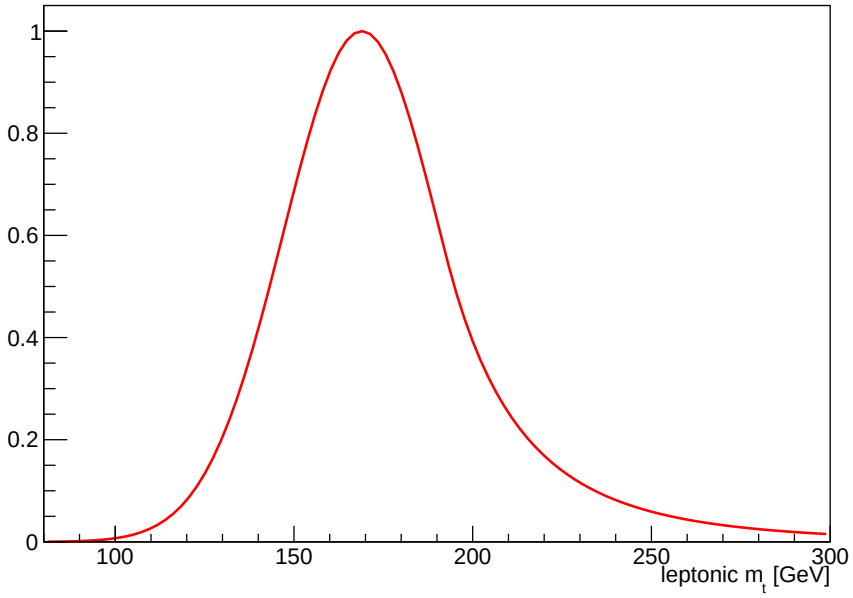

Figure 6.6: Example of an interpolated CrystalBall function corresponding to the energy of the jet assigned to be the leptonic bachelor jet of $E_{\text{bach. jet}} = 150$ GeV.

Overall form of the kinematic χ^2 variable

In total, 3 variables (x', y' from the hadronic side, and m_t from the leptonic side) contribute to the kinematic χ^2 variable in the case there are solutions for the longitudinal component of the neutrino momentum, and an additional variable ($m_{W_{\text{lep}}}$) is included in the case there are no real solutions:

$$\chi^2_{\text{total}} = \chi^2_{m_t^{\text{lep}}}(E_{\text{bach. jet}}) + \chi^2_{y'} + \chi^2_{x'}(y') \left(+ \chi^2_{m_W^{\text{lep}}} \right). \tag{6.2.7}$$

The $\chi^2_{m_t^{\text{lep}}}(E_{\text{bach. jet}})$ contribution is computed from the double-sided CDF (CDF = 0 at both ends of the distribution shown in Figure 6.6) of the event's reconstructed leptonic top mass. All other contributions are extracted from the general expression

$$\chi^2_x = \left(\frac{x - \bar{x}}{\sigma_x} \right)^2, \tag{6.2.8}$$

where x is the observed value of the event, while $\bar{x}$ and σ_x are the mean and the standard deviation of the Gaussian distributions shown in Figures 6.9 and 6.4 (a). In the cases of $\chi^2_{m_t^{\text{lep}}}$ and $\chi^2_{x'}$, the parameters of the distributions are functions of the measured event quantities $E_{\text{bach. jet}}$ and y' respectively. Candidate events are finally required to satisfy a cut on the CDF (CDF $>$ 0.1) in order to reduce contributions from background processes and poorly reconstructed signal events (e.g. not all of the 4 reconstructed jets originate

from the hard-scatter). The CDF distributions of the signal and background samples after the additional selection criteria listed below are shown in Figure 6.10.

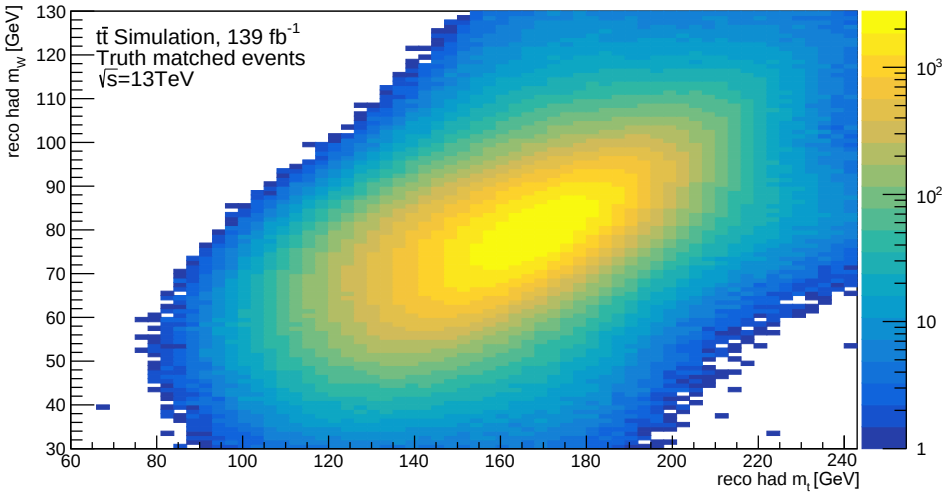

(a) hadronic side masses

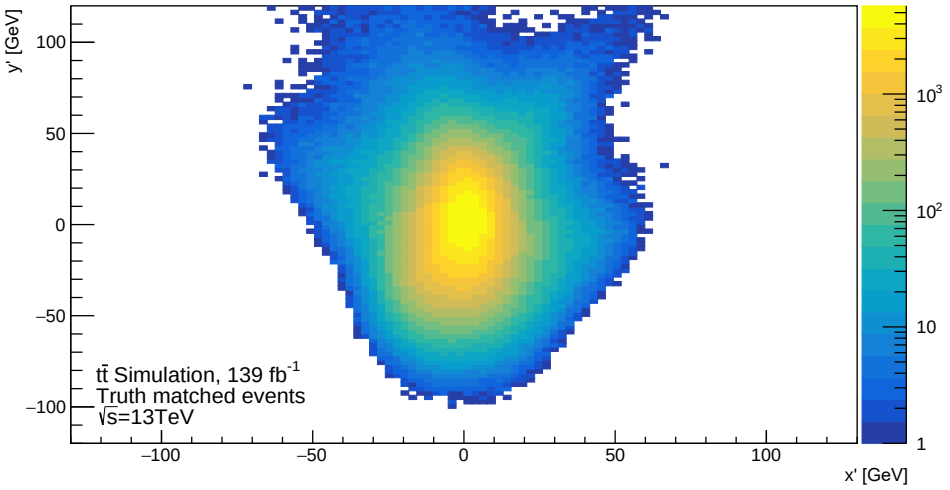

(b) rotated masses

Figure 6.7: Scatter plots of (a) the template hadronic top and hadronic W masses, and (b) the centered and rotated scatter aligning the axis minimising the variance with the new y-axis.

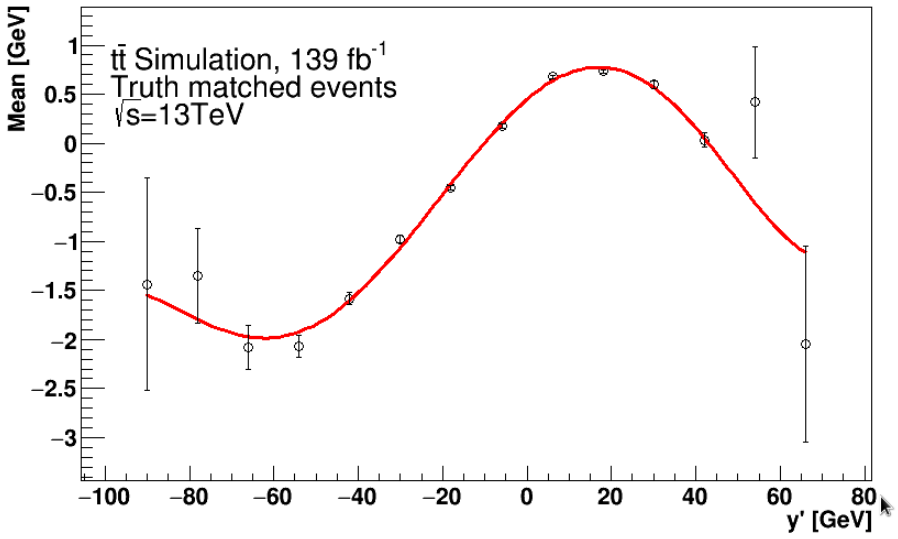

(a) Means

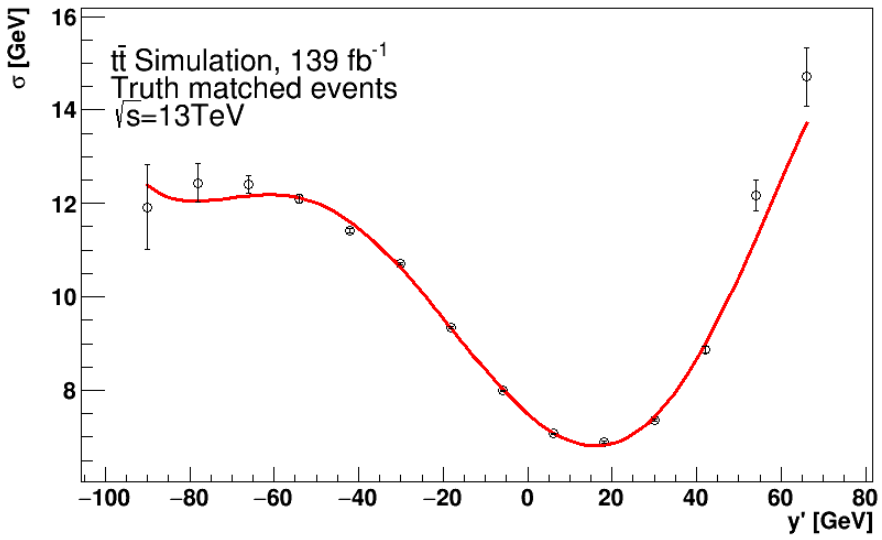

(b) Standard deviations

Figure 6.8: Smoothing of (a) - the means, and (b) - the standard deviations, of the Gaussian function fits over bands of different y' in Figure 6.7.

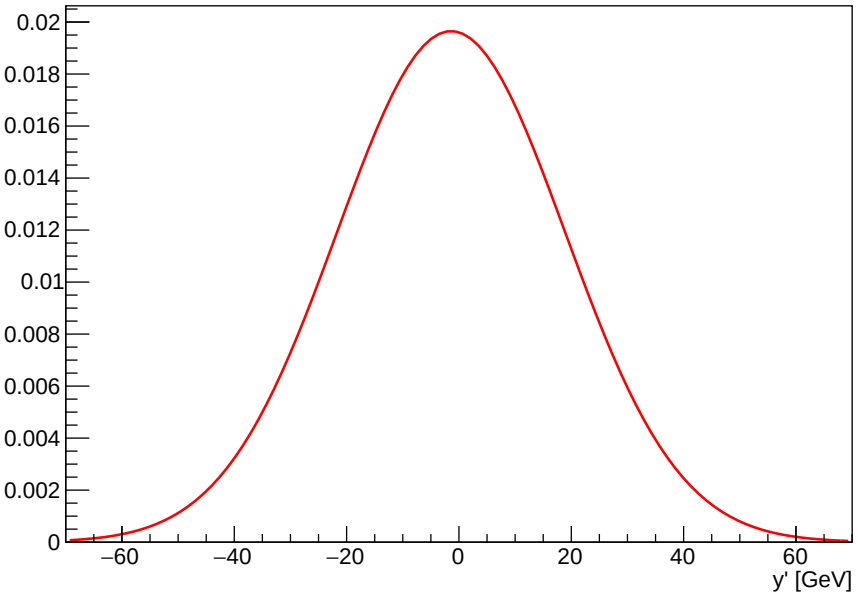

(a) y' distribution

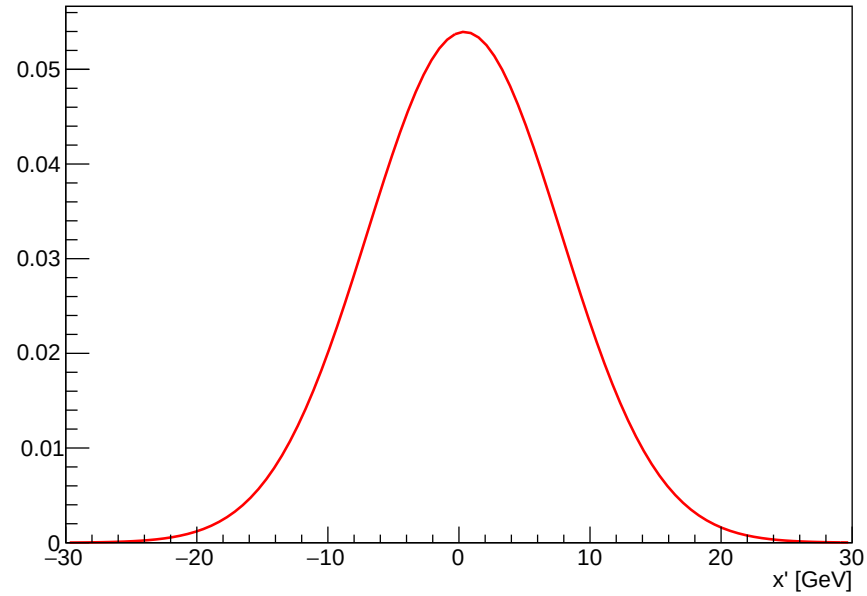

(b) x' distribution

Figure 6.9: Distributions used in determining the contribution towards the kinematic χ^2 of (a) - y', and (b) - example of an interpolated Gaussian distribution of x', generated for an event with reconstructed hadronic side masses of $m_t = 180$ GeV and $m_W = 90$ GeV. These values correspond to $x' = -11.9$ and $y' = 0.27$.

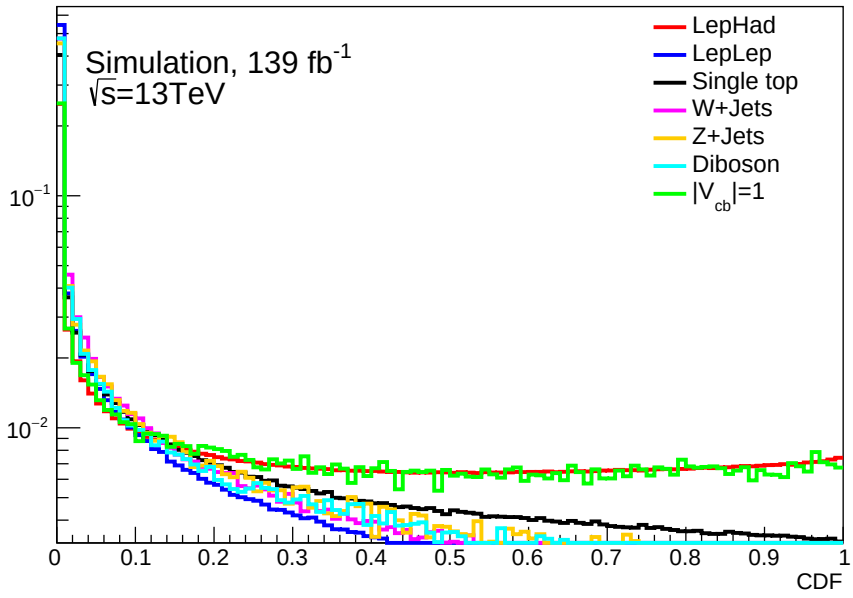

Figure 6.10: Distributions of CDF values corresponding to the best χ^2 value for each event of the samples considered. The distributions are normalised to unity for presentational purposes. Events are rejected if their CDF is below the value of 0.1.

6.2.2 Background $t\bar{t}$ decay mode suppression

In order to reduce background contribution from the fully leptonic $t\bar{t}$ decay mode, two separate lists of criteria for each event are defined, with one having stricter requirements for physical objects (defined in Section 6.1), referred to as tight cuts, and the other having looser requirements - loose cuts. The kinematic requirements for both sets of object definitions are identical. The definitions used in the tight cuts are used throughout the analysis, with the loose cuts only used as additional information for the acceptance or rejection of an event. The differences in the tight and loose object definitions are summarised in Table 6.2. A requirement is enforced on both selections on the number of leptons -

Configuration option	Tight selection	Loose selection
Electron ID	*TightLH*	*LooseAndBLayerLH*
Electron Isolation	*Gradient*	*None*
Muon Quality	*Medium*	*Loose*
Muon Isolation	*FCTight_FixedRad*	*None*
TauJetIDWP	*RNNMedium*	*RNNLoose*

Table 6.2: Differences in the definitions of reconstructed objects between the tight selection and loose selection.

there must be no additional leptons in the range $10 < p_T < 25$ GeV.

Events with handronicly decaying τ leptons are partially removed by requiring events to have exactly 0 τ-tagged jets. The dilepton mode ($\ell + \ell$, $\ell + \tau(\rightarrow \ell\nu\nu)$) is reduced by requiring no additional reconstructed leptons in the range $10 < p_T < 25$ GeV and by requiring no jets present in the kinematic region $1.37 < |\eta| < 1.52$ and $p_T < 140$ GeV. This pseudorapidity region corresponds to the transition region of the Electromagnetic Calorimeter (ECal), leading to misidentification of electrons as jets. The partial reduction of the background events listed below is shown in Appendix A.2.

$\ell + \tau$ mode

Contribution due to this decay mode arises due to hadronic decays of the τ lepton, which are not flagged by the τ-tagger used, with additional jets present in the event due to pile-up or initial state radiation (ISR)/FSR. Another contribution from this mode is due to the reconstructed lepton coinciding with a leptonically decaying τ parton instead, while the parton level ℓ is lost either due to detector inefficiency, or due to it coinciding with a jet, and thus lost due to overlap removal (OR).

$\tau + \tau$ mode

The contribution of the $\tau + \tau$ mode arises through the leptonic decay of at least one of the taus and the presence of additional jets in the event.

$\ell + \ell$ mode

Generated $t\bar{t}$ events with both W bosons decaying leptonically satisfy the analysis' selection criteria in cases in which additional reconstructed jets are present and one of the leptons is either misidentified by the detector, coincides with another physical object and is removed by the OR procedure, or is misreconstructed.

6.2.3 Gluon jet suppression

The number of quarks produced by the semi-leptonic $t\bar{t}$ decay is four. However, it is possible for jets initiated by the partons of the $t\bar{t}$ decay to be missed due to detector inefficiencies, while the event satisfies the 4 jet requirement due to pile-up jets or jets arising from gluon radiation. In order to reduce the occurrence of the latter, each pair of jets in an event has to satisfy an additional set of requirements on the combined mass and angle between the jets. The combined mass against the opening angle between each pair of jets in $t\bar{t}$ events (each event contributes with 6 data points in the scatter plots) are shown in Figure 6.11 and Figure 6.12, with the χ^2 requirement not implemented and the plots being separated depending on the *jet_truth_partonLabel* of the two quarks. From the figures, the following interpretations can be made:

- The di-gluon pairs are mainly confined to the top left (low mass, low angle) region and correspond to Quantum Chromodynamics (QCD) radiation - $g \to gg$.
- The three qg pair plots are similar in shape and are not as concentrated as the di-gluon plot. The more concentrated region is interpreted as corresponding to $q \to qg$ processes. A contribution to these plots stems also from the combination of such a gluon with a random jet from the $t\bar{t}$ decay, yielding a ratio of $b : c : l$ jets approximately matching the expected $4 : 1 : 3$ of pure semi-leptonic $t\bar{t}$ events.
- The bb and cc jet pairs consist of contributions from the $g \to q\bar{q}$ channel. Moreover, bb is also enhanced by pairs formed by an additional b quark (e.g. a $g \to b\bar{b}$ has both jets merged, or one fails the reconstruction step) and a b quark from the $t\bar{t}$ decays.
- The plots containing bc and bl pairs and are suppressed in the low mass, low angle region as they are not a product of a QCD process.

- The cl and ll channels are dominated by the W boson peak, while ll also contains pairs from $g \to ll$. Both also show a low mass tail in the pair mass, which could be events in which energy has been radiated by the W daughter system.

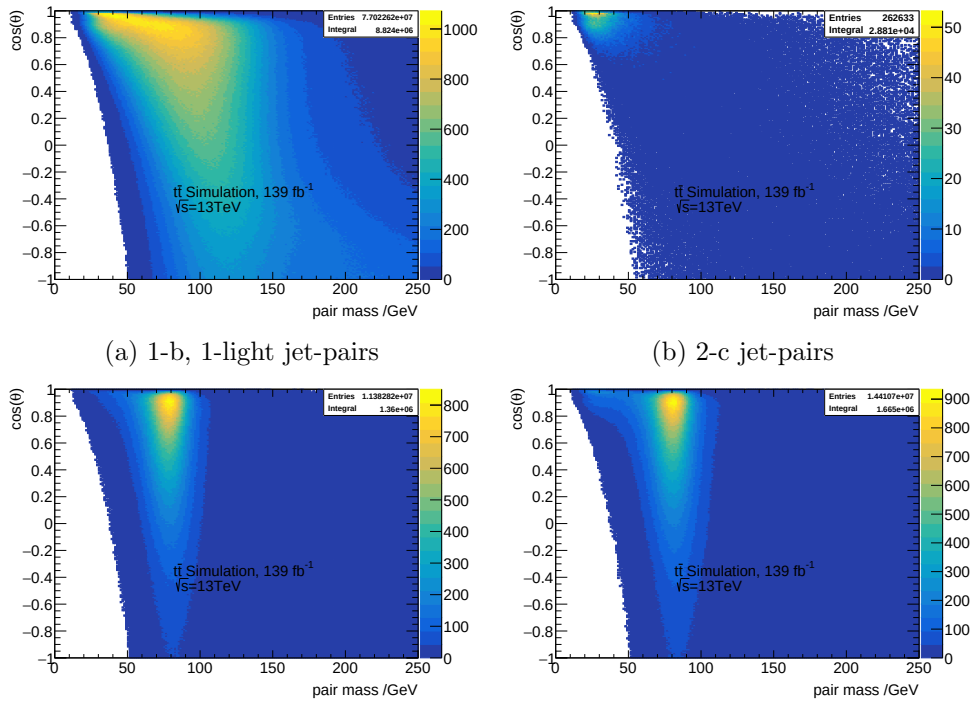

(a) 1-b, 1-light jet-pairs

(b) 2-c jet-pairs

(c) 1-c, 1-light jet-pairs

(d) 2-light jet-pairs

Figure 6.11: Pair mass vs cosine of angle between all pairs of jets of a particular flavour in 4 jet events with exactly 1 electron or muon (no χ^2 cut).

An ellipse cut was introduced in order to reduce the QCD effects observed in the low mass, low angle region, with each event having to satisfy the requirement:

$$\frac{(m_{ij} - 35)^2}{15^2} + \frac{(cos(\theta_{ij}) - 0.99)^2}{0.065^2} > 1 \tag{6.2.9}$$

for each pair of jets. The result of applying the ellipse cut (together with the χ^2 requirement) on $t\bar{t}$ events is shown in Figure 6.13 .

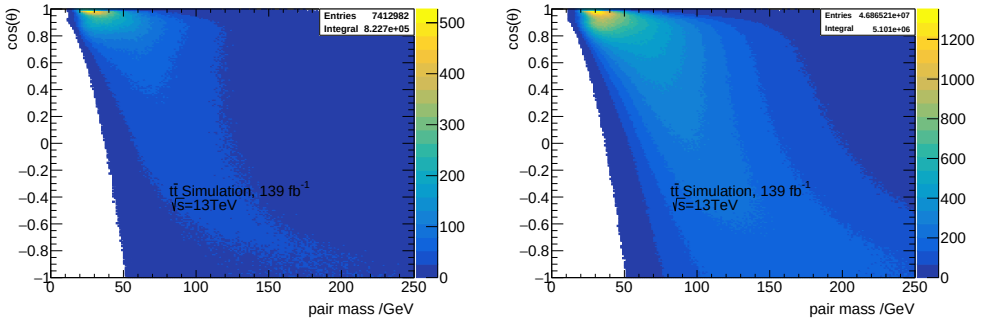

(a) 2-gluon jet-pairs

(b) 1-gluon, 1-b jet-pairs

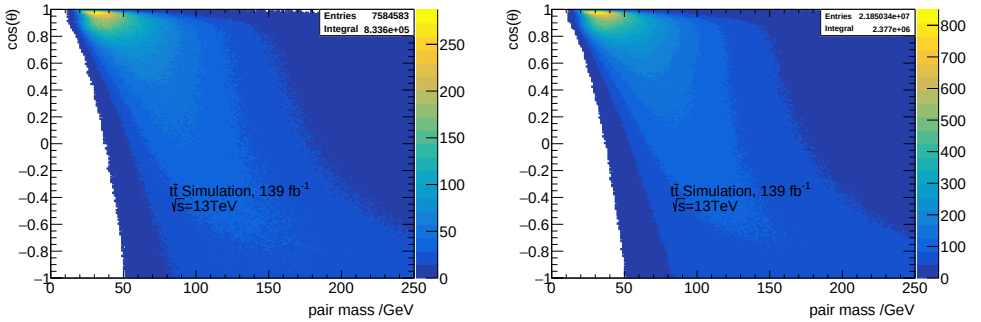

(c) 1-gluon, 1-c jet-pairs

(d) 1-gluon, 1-light jet-pairs

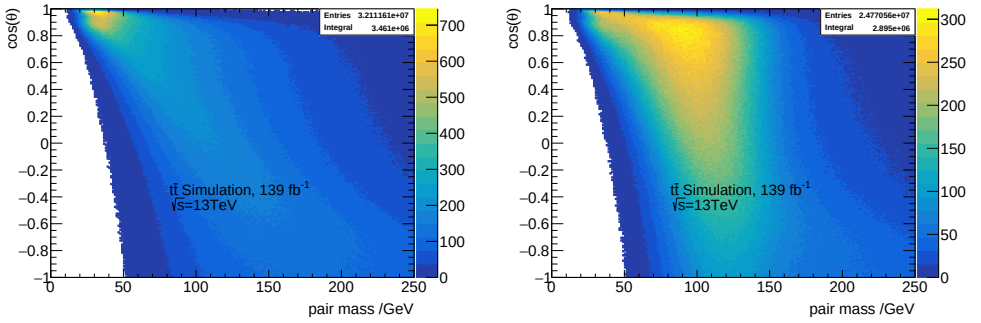

(e) 2-b jet-pairs

(f) 1-b, 1-c jet-pairs

Figure 6.12: Pair mass vs cosine of angle between all pairs of jets of a particular flavour in 4 jet events with exactly 1 electron or muon (no χ^2 cut).

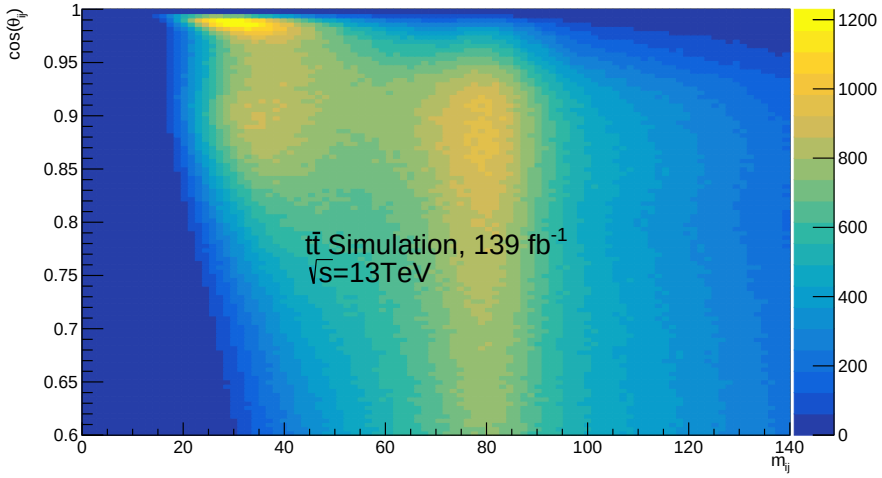

(a) before ellipse cut

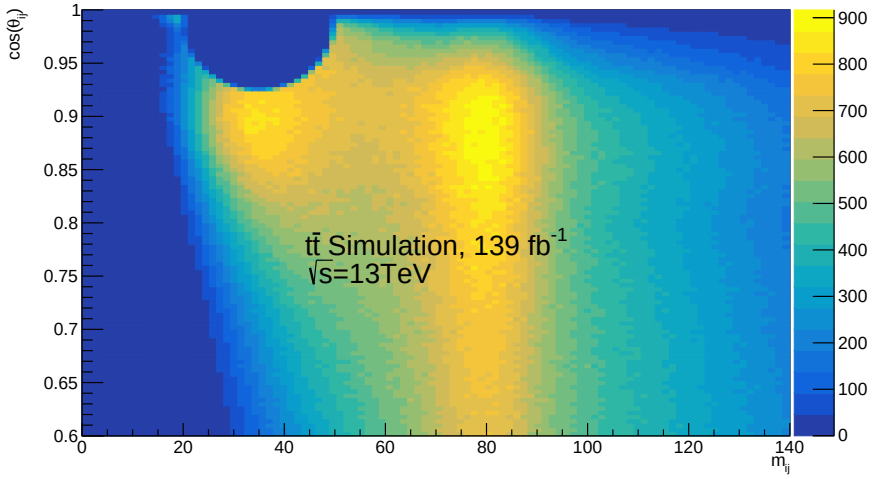

(b) after ellipse cut

Figure 6.13: Result of applying the low mass, low angle ellipse cut on jet pairs in $t\bar{t}$ events.

6.3 Tagging efficiencies

The truth-matched $|V_{cb}| = 1$ dataset was employed in order to compare the tagging efficiency and mistag rates of bachelor beauty jets compared to the one for beauty jets originating from the W decay according to the truth-matched sub-sample of events. The results are presented in Table 6.3, with the efficiency not strongly affected by the difference between the kinematics due to their different origin. The results for the b-tagging efficiency of both bachelor and W daughter b-jets (using the *jet_truth_partonLabel* definition) are compatible with the value of ~ 0.62 which is measured by the ATLAS flavour tagging group in $t\bar{t}$ events (using the *jet_truthflav* definition).

Parameter	$\|V_{cb}\|^2 = 1$ sample	$\|V_{cb}\|^2 = 0$ sample
ϵ_B	0.623 ± 0.006	0.6232 ± 0.0003
f_{Bc}	0.159 ± 0.002	0.1565 ± 0.0001
ϵ_b	0.607 ± 0.009	-
f_{bc}	0.157 ± 0.003	-
ϵ_c	0.3111 ± 0.0003	0.311 ± 0.005
f_{cb}	$(2.80 \pm 0.10) \times 10^{-2}$	$(2.75 \pm 0.01) \times 10^{-2}$
f_{lc}	-	$(9.45 \pm 0.03) \times 10^{-3}$
f_{lb}	-	$(8.4 \pm 0.8) \times 10^{-4}$

Table 6.3: Tagging efficiencies and mistag rates extracted from matched events in the $|V_{cb}|^2 = 1$ and LepHad $t\bar{t}$ samples using the parton flavour identities. Subscript B represents bachelor b-jets, while b represents b-jets from W decays.

6.4 Event yields

The number of events satisfying the separate selection criteria are presented in Table 6.4.

Selection	Samples						
	LepHad (10^6)	LepLep (10^5)	$\|V_{cb}\| = 1$ (10^3)	ST (10^5)	DB (10^4)	W+Jets (10^5)	Z+Jets (10^4)
Preselection	7.0	9.0	6.6	4.9	2.3	5.4	15
$N_j = 4$	3.5	5.5	3.4	3.1	1.3	3.4	9.6
Loose selection	3.4	4.3	3.2	2.9	1.1	3.4	6.3
τ-veto	3.3	3.9	3.2	2.9	1.1	3.4	6.2
"Soft" leptons	3.3	3.4	3.2	2.9	1.1	3.4	5.1
Lepton-jet fakes	2.7	2.6	2.6	2.4	0.9	2.7	3.6
Jet-pair ellipse	2.5	2.3	2.4	2.1	0.8	2.3	3.1
χ^2	1.6	0.6	1.5	0.9	0.3	0.8	1.1

Table 6.4: Effect of the analysis selection cuts on the number of events of the separate samples, where DB stands for Diboson and ST - for single top.

The number of events satisfying the complete set of analysis selection

criteria are shown in Table 6.5 for events stemming from $t\bar{t}$ decays and in Table 6.6 for the non-$t\bar{t}$ backgrounds, split into 10 flavour combination regions which are used in the analysis fitting procedure (apart from the $4b$ channel, see Section 7.4).

	$3l$	$2l$	$1l$	$0l$
LepHad	(10^5)	(10^5)	(10^4)	
$1b$	5.84	3.48	4.36	458
$2b$	-	4.79	8.50	979
$3b$	-	-	0.894	321
$4b$	-	-	-	33.8
LepLep	(10^4)	(10^4)		
$1b$	2.52	1.45	1450	30.3
$2b$	-	2.22	2880	67.9
$3b$	-	-	507	59.5
$4b$	-	-	-	20.2
$\|V_{cb}\| = 1$				
$1b$	215	260	101	13.1
$2b$	-	339	260	48.0
$3b$	-	-	170	63.4
$4b$	-	-	-	5.9

Table 6.5: Numbers of different $t\bar{t}$ channel events passing the cuts, classified according to their total numbers of flavour tags.

6.5 Statistical methods

In this section, a brief summary of the statistical concepts and tools used in the analysis presented in this thesis is given.

6.5.1 Parameter estimation

One of the primary tasks in experimental particle physics is the determination of the properties of the probability distribution function (PrDF) of a random variable x, $f(x)$, through the use of a sample of independent measurements of the variable - $\boldsymbol{x} = \{x_1, x_2, ..., x_n\}$ with size n. The functional form of the PrDF can be defined by a set of m unknown parameters, $\boldsymbol{\theta} = \theta_1, \theta_2, ..., \theta_m$, $f(x) = f(x; \boldsymbol{\theta})$. The parameters which are measured in the experiment are also called the parameters of interest (PoIs) and are usually denoted by $\boldsymbol{\mu}$. They are sometimes separated from the rest, sometimes called nuisance parameters (NPs), in the PrDF: $f(x; \boldsymbol{\mu}, \boldsymbol{\theta})$.

The process of deriving an estimation of the values of the parameters $\boldsymbol{\theta}$, $\hat{\boldsymbol{\theta}}$, and of their corresponding uncertainties, $\delta\hat{\boldsymbol{\theta}}$, from the available experimental

	$3l$	$2l$	$1l$	$0l$
Single top	(10^4)	(10^4)	(10^3)	
$1b$	5.01	1.70	1.29	15.2
$2b$	-	1.72	2.22	33.2
$3b$	-	-	0.313	16.6
$4b$	-	-	-	6.47
Diboson	(10^3)			
$1b$	1.84	445	25.2	0.470
$2b$	-	463	38.6	1.10
$3b$	-	-	11.5	1.04
$4b$	-	-	-	0.867
W+Jets	(10^4)	(10^3)		
$1b$	5.97	8.40	386	3.42
$2b$	-	7.65	496	9.23
$3b$	-	-	122	2.51
$4b$	-	-	-	1.65
Z+Jets	(10^3)	(10^3)		
$1b$	7.83	1.32	67.5	0.792
$2b$	-	1.32	90.6	2.77
$3b$	-	-	34.4	1.52
$4b$	-	-	-	0.573

Table 6.6: Numbers of events of various background modes passing the cuts, classified according to their total numbers of flavour tags and background source.

data is called inference, while the function of the data sample which provides the estimates as an output is called an estimator. Sometimes, both the estimator and the estimate are denoted with $\hat{\boldsymbol{\theta}}$. There is no unique way of defining an estimator for each case, so a suitable choice is made by requiring that it satisfies the following criteria:

- Consistency criteria - an estimator is consistent if its estimates $\hat{\boldsymbol{\theta}}$ converge to the true values of $\boldsymbol{\theta}$ as the number of independent measurements n increases: $\lim_{n\to\infty} \hat{\boldsymbol{\theta}} = \boldsymbol{\theta}$.

- Bias criteria - The bias b of an estimator producing the estimates $\hat{\boldsymbol{\theta}}$ is defined as:

$$b(\hat{\boldsymbol{\theta}}) = \mathbb{E}(\hat{\boldsymbol{\theta}}) - \boldsymbol{\theta}, \tag{6.5.1}$$

  where $\mathbb{E}$ is the expectation value operator. Estimators are labeled as unbiased if $b(\hat{\boldsymbol{\theta}}) = 0$. If an estimator has a known bias, a new, unbiased estimator can be defined as $\hat{\boldsymbol{\theta}}' = \hat{\boldsymbol{\theta}} - b(\hat{\boldsymbol{\theta}})$.

- Efficiency criteria - the efficiency of an estimator is given by the expression

$$\epsilon(\hat{\boldsymbol{\theta}}) = \frac{\mathbb{V}_{\mathrm{CR}}(\hat{\boldsymbol{\theta}})}{\mathbb{V}[\hat{\boldsymbol{\theta}}]}, \tag{6.5.2}$$

where $\mathbb{V}(\hat{\boldsymbol{\theta}})$ is the variance of the estimator and $\mathbb{V}_{\mathrm{CR}}$ is its Cramér-Rao lower bound. For each parameter $\hat{\theta}_i$, it is given by:

$$\mathbb{V}_{\mathrm{CR}}(\hat{\theta}_i) = \frac{\left(1 + \frac{\partial b(\hat{\theta}_i)}{\partial \boldsymbol{\theta}}\right)^2}{\mathbb{E}\left(\left(\frac{\partial (lnL)}{\partial \theta_i}\right)^2\right)}. \tag{6.5.3}$$

The quantity L in Equation 6.5.3 is the likelihood $L(\boldsymbol{x}; \boldsymbol{\theta})$, which is given by:

$$L(\boldsymbol{x}; \boldsymbol{\theta}) = \prod_i^n f(x_i; \boldsymbol{\theta}) \tag{6.5.4}$$

and can be interpreted as the probability density function for the observed values of $\boldsymbol{x}$ given the parameters $\boldsymbol{\theta}$. The likelihood is constructed by normalised PrDFs:

$$\int f(x; \boldsymbol{\theta}) dx = 1. \tag{6.5.5}$$

The product of PrDFs is also normalised:

$$\int L(\boldsymbol{x}; \boldsymbol{\theta}) dx_1 dx_2 ... dx_n = 1, \tag{6.5.6}$$

meaning the integral of the likelihood function is independent of the parameters $\boldsymbol{\theta}$ [124, 125].

6.5.2 Maximum likelihood fit

One of the methods for parameter estimation is the maximum likelihood (ML) method, which chooses the values of $\hat{\boldsymbol{\theta}}$ which maximise the value of $L(\boldsymbol{x}; \boldsymbol{\theta})$:

$$\hat{\boldsymbol{\theta}} = \underset{\boldsymbol{\theta}}{\operatorname{argmax}}\, L(\boldsymbol{x}; \boldsymbol{\theta}). \tag{6.5.7}$$

The procedure is often called best fit, because it finds the best parameters for which the theoretical PrDF model matches the experimental data. It is often more convenient to minimise the negative logarithm of the likelihood function, as the product transforms into a sum:

$$-lnL(\boldsymbol{x}; \boldsymbol{\theta}) = -ln\Big(\prod_i^n f(x_i; \boldsymbol{\theta})\Big) = -\sum_i^n lnf(x_i; \boldsymbol{\theta}). \tag{6.5.8}$$

The change into computing the sum of logarithms does not affect the result, as the position of the extremum is the same. Provided $-lnL$ is differentiable with

respect to each θ_i and the minima do not occur at the boundary of the allowed ranges for θ_i, a necessary condition for the minimum are the equations:

$$-\frac{\partial lnL(\boldsymbol{x};\hat{\boldsymbol{\theta}})}{\partial\theta_i} = 0, \tag{6.5.9}$$

for $i = 1, 2, ..., m$.

In the asymptotic limit, when the number of measurements $n \to \infty$, the ML estimator is consistent, unbiased and reaches the minimum variance bound. The estimator is also invariant under parameter transformations, e.g $\psi = g(\theta)$. In such cases, the ML estimate $\hat{\psi}$ will be $\hat{\psi} = g(\hat{\theta})$ [125]. The shape of the likelihood function can have any form for small sample sizes, but it converges into a Gaussian function in the asymptotic limit, leading to lnL assuming a parabolic shape [124].

The confidence intervals of the estimated parameters $\hat{\boldsymbol{\theta}}$, usually corresponding to a coverage of 68.27% (or 1σ) can be derived by different methods. A widely used one is the likelihood scan, in which the behaviour of $-lnL$ around its minimum, $(-lnL)_{\min} = -lnL(\boldsymbol{x};\hat{\boldsymbol{\theta}})$, is studied. The uncertainties of each estimated parameter are determined by the amount each parameter is shifted in order for the likelihood function to change by 1/2:

$$-lnL(\boldsymbol{x};\hat{\boldsymbol{\theta}} \pm \delta\hat{\boldsymbol{\theta}}) = (-lnL)_{\min} + \frac{1}{2}. \tag{6.5.10}$$

In particle physics, an observed random variable x, e.g. mass or momentum of a reconstructed physical object, is presented in histograms with N number of bins. Often, the size of the data sample is large and the computation of the likelihood using the bin entries of the histogram becomes more efficient than using individual events. A requirement for making use of a binned likelihood fit is that the information on $\boldsymbol{\theta}$ from the variation of $f(x;\boldsymbol{\theta})$ inside the bounds of each bin is negligible compared to the variation over the whole range of bins. The expectation value of the events recorded in each bin B_i is given by:

$$\mathbb{E}(B_i) = \mu s_i + \sum_j^K \nu^j b_i^j, \tag{6.5.11}$$

where μ is the signal strength of the signal of interest of the study, and the sum is over K number of background processes with strengths ν^j. The case $\mu = 0$ corresponds to the background-only hypothesis, while $\mu \neq 0$ corresponds to the signal+background hypothesis, with the cross-section of the signal sample ($|V_{cb}| = 1$ in the case of the analysis presented in this thesis) being regulated by μ. The quantities s_i and b_i^j are the expected number of signal (with PrDF

f_s) and background (with PrDFs f_b^j) events inside bin B_i:

$$s_i = s_{total} \int_{B_i} f_s(x; \boldsymbol{\theta}_s) dx \tag{6.5.12}$$

$$b_i^j = b_{total}^j \int_{B_i} f_b^j(x; \boldsymbol{\theta}_b^j) dx, \tag{6.5.13}$$

where s_{total} and b_{total}^j are the total number of signal and background events, which are usually extracted from MC. Each bin entry can be described by Poisson statistics, leading to the likelihood of each bin B_i being measured to contain C_i number of events to be the product of the individual bin distributions:

$$L_{\mathrm{P}}(\boldsymbol{x}; \boldsymbol{\theta}) = \prod_{B_i}^{N} \frac{\mathbb{E}(B_i)^{C_i}}{C_i!} e^{-\mathbb{E}(B_i)}, \tag{6.5.14}$$

$$-lnL_{\mathrm{P}}(\boldsymbol{x}; \boldsymbol{\theta}) = -C_i ln\mathbb{E}(B_i) + \sum_{B_i}^{N} \mathbb{E}(B_i) + const. \tag{6.5.15}$$

Equation 6.5.14 is also known as the extended binned likelihood function [124, 125].

6.5.3 Nuisance parameters

The NPs include both statistical uncertainties due to data fluctuations, as well as systematic uncertainties. The latter can stem from both experimental effects, such as efficiency and calibration of the detector, as well as from the theoretical model used in creating the PrDFs. Prior knowledge of the systematic uncertainties' effects on the reconstructed physical objects are provided by the appropriate ATLAS combined performance groups. The effects are separated into terms affecting only the normalisation, only the shape, or both normalisation and shape of the reconstructed variables. MC distributions of particle variables are available with all systematic NPs set to their central (nominal) value, as well as independent variations of each parameter by $\pm 1\sigma_\theta$. The values of the NPs' estimates and their variations provided by ATLAS are not necessarily the estimated by the likelihood method values for each physics analysis - for example, additional constraints may be introduced by the event selection. A list of theoretical and experimental sources of uncertainty considered in the analysis presented in this thesis is provided below.

Luminosity

The luminosity measurement is performed based on an absolute calibration of a collection of luminosity-sensitive sub-detectors during yearly special low-

luminosity runs using the van der Meer method [126]. The calibration is then transferred into the high-luminosity regime in which physics data-taking occurs. The total uncertainty of the luminosity measurement is 1.7% for the full Run 2 of pp collisions [127]. Since V_{cb} is determined as a ratio, the error in the luminosity is not expected to contribute to the error of V_{cb} at leading order.

Flavour tagging scale factors

The efficiency of correctly flavour tagging a b-jet as a b-tagged jet (probability ϵ_b) and the charm and light mistag rate (probability f_{cb} and f_{lb}) need to be calibrated in MC to match the measured tagger performance on data events. These corrections are applied by scale factors (SFs), which are defined for the efficiency (mistag) of flavour i as flavour j as:

$$\mathrm{SF}_{ij} = \frac{f_{ij}^{\mathrm{data}}}{f_{ij}^{\mathrm{MC}}}. \tag{6.5.16}$$

The SFs (and the uncertainties related to them) are expected to be a continuous function of jet kinematics and they are presented as functions of jet p_T. The uncertainties result in 17 decorrelated NPs - 9 are connected to ϵ_b, 4 - to f_{cb} and 4 - to f_{lb}.

Jet energy scale and resolution

Corrections to the four-momenta of reconstructed jets are applied in 2 steps, with each contributing different uncertainties to the final calibration:

- simulation-based calibration - corrections to the reconstructed jet four-momentum in MC events in order to match the kinematics of the truth level jets (no detector effects applied). These changes include terms for in-time and out-of-time pile-up effect corrections, terms correcting for energy losses in passive detector material and terms connected with different detector responses to jets of different flavour.

- in situ calibration - corrections added to balance jet response in data and MC, which is measured by balancing the p_T of the jet with the p_T of a more accurately reconstructed object - samples containing $Z(Z \to \ell\ell)$+jet, γ+jet events are used. Dijet events are used to calibrate jets in the forward regions ($0.8 < |\eta| < 4.5$) using jets in the central region ($|\eta| < 0.8$). Multijet events are used to calibrate high p_T jets [128].

The uncertainties connected to the jet energy scale (JES) are presented as 30 decorrelated NP which depend on the jet kinematics (η and p_T). They are divided into: 15 originating from the in situ calibration uncertainties, 6 NPs

are connected to the $|\eta|$ intercalibration, 4 stem from the uncertainty of the pile-up components, one NP corresponds to the uncertainty of jet energy due to jets not depositing their whole energy inside the calorimeter (punch-through), one NP representing uncertainties in high p_T jets and 3 NPs characterise the detector response depending on the jet flavour.

A preliminary study (discussed in Section 7.1) of the measurement sensitivity revealed the leading contribution to the measurement's systematic uncertainty to be due to the JES flavour response and flavour composition. The flavour composition and flavour response systematic uncertainties on jets are connected with different detector signatures depending on the nature of physics object (gluon or quark) which initiated the reconstructed jet. The JES uncertainty contributions from the flavour response and flavour composition components can be represented by the first and second term in the following expression respectively:

$$\Delta R_s = f_g \times (\mathcal{R}_g^{G_1} - \mathcal{R}_g^{G_2}) \oplus \Delta f_g \times \frac{|\mathcal{R}_q - \mathcal{R}_g|}{f_g \mathcal{R}_g + (1 - f_g)\mathcal{R}_q}. \tag{6.5.17}$$

The fraction of jets which are initiated by gluons and its uncertainty are denoted as f_g and Δf_g respectively, $\mathcal{R}_q$ and $\mathcal{R}_g$ are the detector response to light quark and gluon initiated jets, and $\mathcal{R}_g^{G_1} - \mathcal{R}_g^{G_2}$ is the difference in detector response to gluon jets in samples generated by two different Monte Carlo event generators (MCEGs). The response $\mathcal{R}$ is defined as the ratio of the reconstructed and truth level energies of a jet [128]. The default for ATLAS values of $f_g \pm \Delta f_g$ are set to be (0.5 ± 0.5) [129]. However, since the fraction is analysis dependent, improvements on the values can be reached by extracting them using the MCEG truth information. The *jet_truth_partonLabel* container, defined as the flavour of the generator truth parton with the highest energy inside the jet, is used to extract f_g and Δf_g from the subset of sample events satisfying the analysis selection criteria. For the analysis presented in this thesis, in addition to the nominal POWHEG+PYTHIA8 $t\bar{t}$ sample, variations of both the matrix element generator and the parton shower was included in the estimation of f_g, Table 6.7.

As the kinematics of jets of different origin are different, the values of $f_g \pm \Delta f_g$ were determined in separate regions in the $|\eta| - p_T$ plane. For the analysis presented in this thesis, the boundaries of the regions were defined by the collection of lines at $\{0, 25, 30, 35, 40, 45, 50, 55, 60, 65, 75, 85, 100, 150, 250, 500\}$ GeV in p_T and at $\{0, 0.3, 0.8, 1.2, 2.1, 2.5\}$ in $|\eta|$. The extracted values f_g and Δf_g in the $p_T - |\eta|$ plane, as well as the effect of these custom values on the uncertainties due to the jet flavour response and composition are shown in the figures of Appendix A.3. Events generated by a different MCEG for the $|V_{cb}| = 1$ sample do not exist, but since the difference between this sample and the nominal $t\bar{t}$ sample is the b-jet W daughter and the strong interaction is not

Generator Parameters	Variation
POWHEG+PYTHIA8	Nominal
POWHEG+HERWIG7	Parton shower
aMCatNLO+HERWIG7	Matrix element
POWHEG+PYTHIA8 HDAMP=517	h_{damp}

Table 6.7: Alternative samples used in order to estimate the effects of jet flavour response. The parameter h_{damp} controls the matrix element and parton shower matching in POWHEG, controling the high-p_T radiation. The nominal POWHEG+PYTHIA8 sample has the parameter set to 1.5 times the mass of the top quark, $h_{\text{damp}} = 1.5 \times m_t = 258$ GeV ($h_{\text{damp}} = 517$ corresponds to $3m_t$).

dependent on flavour, the values for f_g and Δf_g extracted from the $t\bar{t}$ sample were carried over to the $|V_{cb}| = 1$ sample.

Jet energy resolution

The jet energy resolution (JER) uncertainties are connected to the smearing procedure applied to MC events in order to equate the resolution in simulation to the one determined by data-driven methods in events containing well defined di-jet systems or jets recoiling against $Z/\gamma \to \ell^+\ell^-$.

Jet vertex tagger

The uncertainties connected to the jet vertex tagger (JVT) are extracted from the variations of the MC scale factor.

Electrons, muons and taus

Uncertainties connected to the leptons and hadronically decaying taus arise from utilising the reconstruction, identification and isolation algorithms. Additional NPs are included to account for the uncertainties connected to the lepton triggers used. Differences between the performance on data and on MC samples are corrected by scale factors. In addition, energy scale and resolution uncertainties derived from $Z \to \ell^+\ell^-$ or $J/\psi \to \ell^+\ell^-$ are also introduced. Since the reconstructed taus do not participate in the analysis, variations of the scale factors and energy resolution connected to them are not expected to contribute to the total uncertainty.

Pile-up reweighting

To include pile-up interactions in simulation, a set of minimum-bias events are inserted onto the simulated hard-scattering processes and events are reweighted in order to match the pile-up profile of the detector. The variations of these weights are included as a nuisance parameter in the fit.

Background modelling

Values for the uncertainties in the estimation of the background processes' cross-sections were taken from an analysis with similar selection criteria [130]. The uncertainties were set to the conservative values of 5.4% for the single top sample, 45% for the W+jets sample, and 50% for the diboson and Z+jets samples.

Chapter 7

Fit results and conclusions

A simplified preliminary fit for the sensitivity of the $|V_{cb}|$ measurement was performed in order to approximate the statistical contribution to the uncertainty of the measurement. The samples used in the fit were the $|V_{cb}| = 1$, LepLep and LepHad samples. Another fit was performed using the TRExFitter [131] framework, which makes use of the HistFactory package [132] to create statistical models and then utilises the statistical tools RooFit [133] and RooStats [134] of the ROOT [2] software framework. In this second fit, all non-$t\bar{t}$ background samples and all nuisance parameters (NPs) from Section 6.5.3 were included.

7.1 Preliminary extraction of $|V_{cb}|$ uncertainty

The fractional contribution from signal ($|V_{cb}| = 1$) events to the total sample of $|V_{cb}| = 1$, LepHad and LepLep events was estimated by a binned maximum likelihood fit. The first stage was separating the total $\ell+jets$ events, TotLepHad (the combination of $|V_{cb}| = 1$ and LepHad from the nominal sample), from the LepLep distribution. The variable used was the scalar sum of the transverse momentum of the jets assigned to be the daughters of the hadronically decaying W boson - $\sum p_T^{W-\text{daughter}}$, presented in a histogram of 100 bins in the range $50 - 300$ GeV. The distributions of the variable for the two channels (summed over all tagging regions) is shown in Figure 7.1, where the distribution peaks were equalised for presentational reasons. The differences between the two distributions provide the separation power between the LepLep and TotLepHad sub-samples in the analysis. The distributions of $\sum p_T^{W-\text{daughter}}$ were divided into the 10 flavour combination regions of Table 6.5, each contributing to the likelihood.

The separation of the $|V_{cb}| = 1$ and LepHad samples was performed by fitting the number of events within each tagging region. A template of the kinematic and number distribution of the data was taken from full Monte Carlo using a high statistics sample. This template was used to generate

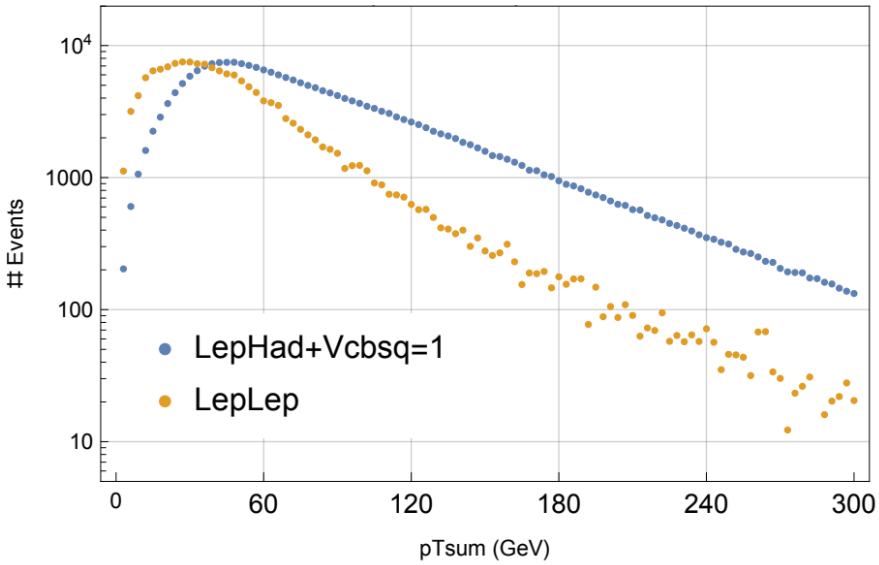

Figure 7.1: Distributions of the scalar sum of the transverse momentum of hadronic W boson daughters, $(\sum p_T^{W-\text{daughter}})$, shifted by -50 GeV. The blue dots represent the LepHad and $|V_{cb}| = 1$ channel, while the orange - the LepLep channel. The number of events are scaled in order to match the heights of the peaks for presentational purposes.

1000 toy Monte Carlo samples with the appropriate statistics for the actual measurement, which were each then fitted with the high-statistics template itself to estimate the statistical uncertainties from the fit:

$$\frac{\delta|V_{cb}|^2}{|V_{cb}|^2} \sim \pm 0.25(\text{stat.}). \tag{7.1.1}$$

7.2 Extraction of the sensitivity using the TRExFitter framework

A more advanced, profile likelihood fit was performed using the TRExFitter framework [131] on an Asimov dataset (the dataset in which all observed quantities are set to their estimated values) primarily to determine the systematic uncertainties but also confirming the statistical uncertainty extracted from the preliminary fit. In this approach, the extraction of the normalisation of LepLep, LepHad and $|V_{cb}| = 1$ samples from background is performed at once using the Minuit package in combination with the MIGRAD minimisation approach. The parameter error estimation is implemented by the MINOS error analysis routine, which takes into consideration correlations between the parameters and does not rely on the parabolic shape of $-lnL$ [135, 136].

In addition to the extended binned likelihood function (Equation 6.5.14), a Gaussian distribution term for each NP for which there is prior knowledge is

included:

$$\mathcal{G}(\theta) = \frac{1}{\sqrt{2\pi}\sigma_\theta}\exp\Big[-\frac{(\theta-\theta_0)^2}{2\sigma_\theta^2}\Big], \tag{7.2.1}$$

where θ_0 and σ_θ are defined respectively as the prediction of the nominal value and its standard deviation provided by the ATLAS combined performance groups (Section 6.5.3). The fitting algorithm then extrapolates and interpolates parameter values using the three values provided. $\mathcal{G}(\theta)$ is often called the constraining term or penalty term, because it is constraining the range of the parameter values by increasing the $-lnL$ for values away from the nominal one determined by the prior knowledge. As reparameterisation does not affect the position of the extremum of the likelihood, the transformation $g(\theta) = (\theta-\theta_0)/\sigma$ is made in order to shift the mean to zero and the standard deviation to unity. The likelihood is then given by the expression:

$$L_{\mathrm{TRF}}(\boldsymbol{x};\boldsymbol{\theta}) = \prod_{B_i}^{N}\frac{\mathbb{E}(B_i)^{C_i}}{C_i!}e^{-\mathbb{E}(B_i)}\prod_{i}^{G}\frac{1}{\sqrt{2\pi}}\exp\Big[-\frac{g(\theta_k)^2}{2}\Big], \tag{7.2.2}$$

where the last product is over the complete set of nuisance parameters G for which information external to the measurement is used.

As event generation and detector simulation are computationally intensive, Monte Carlo (MC) samples of some processes can have limited statistics in a region of phase-space of interest, which could lead to the imprecise estimation of the underlying distribution which is followed by the variable of interest. In order to compensate for this, additional parameters, the gamma (or γ) NPs are introduced for each bin in each region of the fit [132]. They correspond to a Poisson subsidiary measurement, leading to γ function priors. In principle, a separate γ NP would be introduced for each bin of each tagging region for each sample individually, but this would lead to a large number of NPs, leading to difficulties performing the minimisation procedure. Instead, a general procedure was adopted, in which an overall γ NP is introduced for each bin of each region of the combined samples.

Finally, in contrast with the preliminary estimation, the systematic uncertainties, as well as the uncertainties on the cross-sections of the background processes and luminosity were added to the fit. The $4b$ flavour region was not included in the fit due to it being dominated by $t\bar{t}b\bar{b}$ events. Strategies to approximate the contribution of this background are given in Section 7.4.2.

The post-fit mean and uncertainties of the NPs are presented in Figure 7.2. As the fit is performed on the Asimov dataset, the means are centered at zero. Some of the parameters (jet energy scale (JES) and b-tagging related) are constrained by the fit - they have uncertainty lower than the 1σ provided by the ALTAS combined performance groups. This is a result of either the

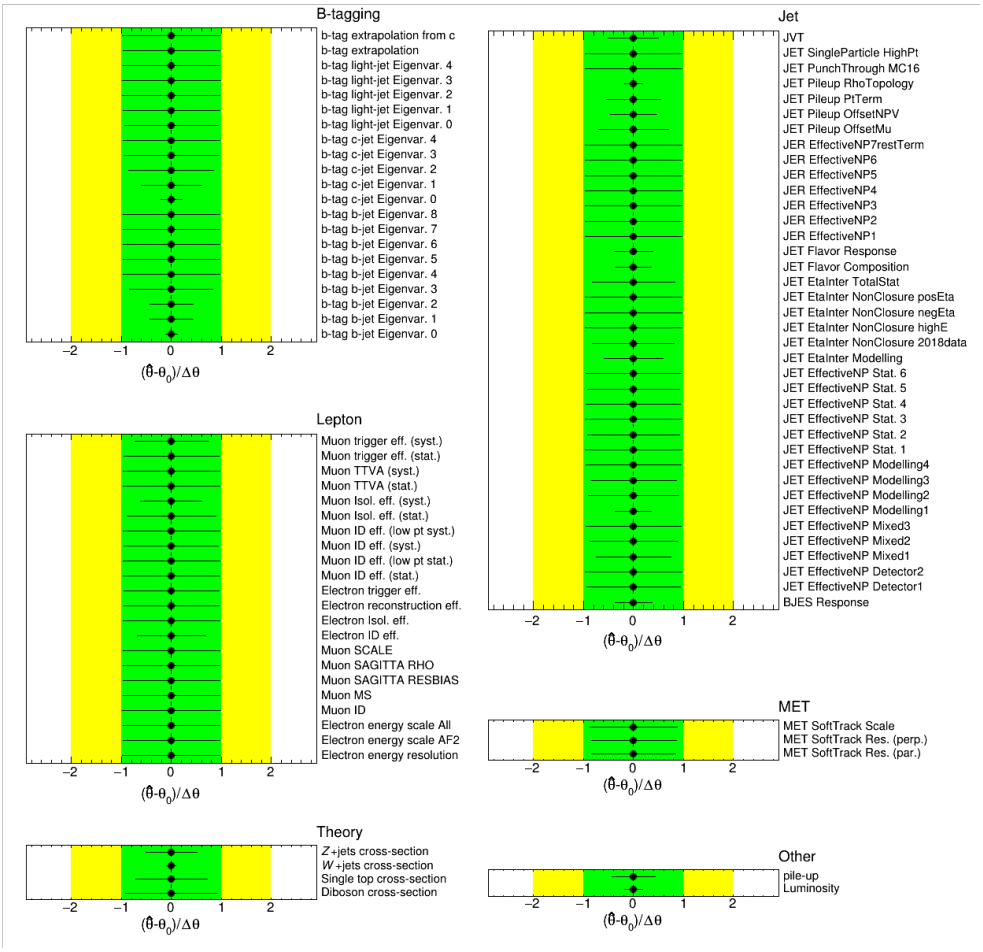

Figure 7.2: The post-fit means (black dots) and uncertainties (black lines) of the NPs imposed by the TRExFitter maximum likelihood fit. The green band corresponds to the pre-fit one standard deviation, while the yellow - two standard deviations.

prior estimation of the uncertainties being overly conservative, or the analysis being more sensitive than the procedures used to derive the prior uncertainties (e.g. the b-tag eigen-variables). The correlation matrix of the NPs obtained from the fit is shown in Figure A.13 of Appendix A.4, with only the NPs which have at least 20% correlation with another being shown.

The systematic uncertainties are ranked by their impact ($\Delta\mu$) on the value of the parameter of interest (PoI) of the study (μ), which regulates the signal sample ($|V_{cb}| = 1$) cross-section. The impact is calculated as the shift in the value of μ between the nominal fit in which all NPs are fixed to their estimated by the maximum likelihood fit values $\hat{\boldsymbol{\theta}}$, and a fit in which the corresponding NP is varied. The 20 leading NPs by post-fit impact are presented in Figure 7.3. In the same figure, the pre-fit impact is defined as $\Delta\hat{\theta} = \hat{\theta} \pm \Delta\theta$, where

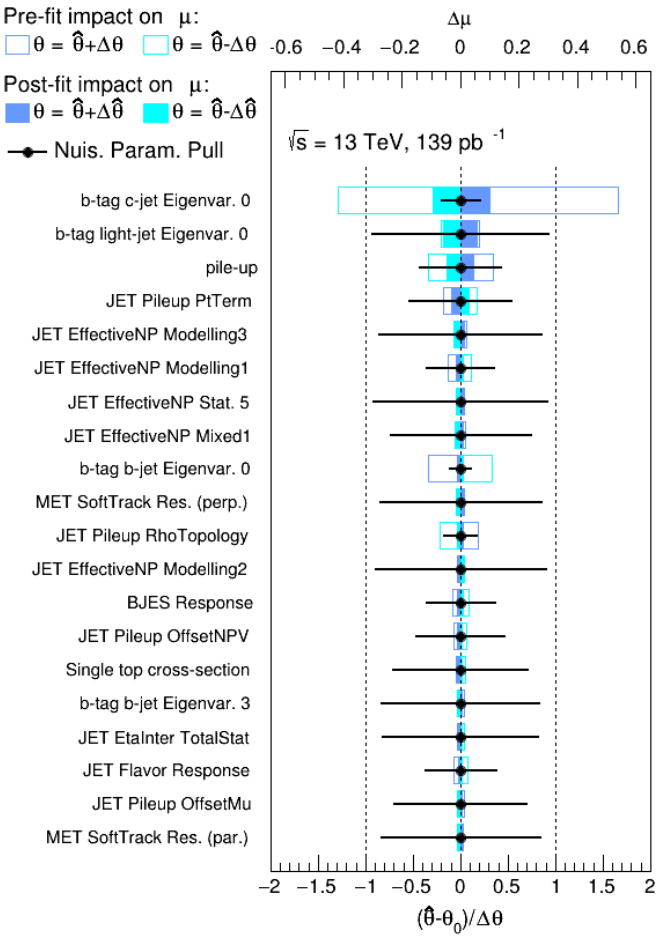

Figure 7.3: The 20 leading NPs (including gammas) in terms of PoI impact (top axis). The bottom axis represents the parameter pull, comparing the best fit value $\hat{\theta}$ to the nominal pre-fit value θ_0 in units of pre-fit uncertainty $\Delta\theta$ (the information contained in Figure 7.2).

$\Delta\theta = 1$ is the variation of the reparameterised NP with a Gaussian constraint. The post-fit impact is defined as $\Delta\hat{\theta} = \hat{\theta} \pm \Delta\hat{\theta}$, where $\Delta\hat{\theta}$ is the variation of

$\hat{\theta}$ determined by the fit. For constrained parameters, the value of $\Delta\hat{\theta}$ can be lower than the value of $\Delta\theta$. The sum in quadrature of all the post-fit impacts of the NPs (apart from the γ parameters) represents the systematic uncertainty of the measurement.

The uncertainty extracted from the fit is:

$$\frac{\Delta|V_{cb}|^2}{|V_{cb}|^2} = 0.28(\text{stat.}) \oplus 0.19(\text{syst.}) = 0.34, \tag{7.2.3}$$

or equivalently,

$$\frac{\Delta|V_{cb}|}{|V_{cb}|} = \frac{1}{2}\frac{\Delta|V_{cb}|^2}{|V_{cb}|^2} = 0.14(\text{stat.}) \oplus 0.10(\text{syst.}) = 0.17. \tag{7.2.4}$$

7.3 Result discussion

The result obtained using the TRExFitter framework (Equation 7.2.4) is ~ 2 times larger than the uncertainty estimated in the feasibility study [1] (Equation 5.3.9), which can be accounted for by the contamination of events by gluon-initiated jets or jets originating from pile-up. The presence of such jets affects the flavour tagging performance on light jets, with mistag rates (using the *jet_truthflav* definition) measured to be $f_{lb} = 2.4 \times 10^{-3}$ and $f_{lc} = 9 \times 10^{-3}$, compared to the values used in the feasibility study of $f_{lb} = 6 \times 10^{-4}$ and $f_{lc} = 3 \times 10^{-3}$ (Table 5.2). Moreover, the measured reconstruction efficiency of semi-leptonic $t\bar{t}$ events, ϵ_0, can be extracted from the number of LepLep events satisfying the analysis cuts given in Table 6.4, the rows of which can be expressed up to leading order in mistag rates by Equations 7.3.1-7.3.4:

$$\frac{N_{1b}}{2} = \mathcal{L}\sigma_{t\bar{t}}\mathcal{BF}\epsilon_0\big(2\epsilon_b(1-\epsilon_b)(2-3f_{lb}-f_{cb}) + (1-\epsilon_b)^2(3f_{lb}+f_{cb})\big) \tag{7.3.1}$$

$$\frac{N_{2b}}{2} = \mathcal{L}\sigma_{t\bar{t}}\mathcal{BF}\epsilon_0\big(\epsilon_b^2(2-3f_{lb}-f_{cb}) + 2\epsilon_b(1-\epsilon_b)(3f_{lb}+f_{cb})\big) \tag{7.3.2}$$

$$\frac{N_{3b}}{2} = \mathcal{L}\sigma_{t\bar{t}}\mathcal{BF}\epsilon_0\epsilon_b^2(3f_{lb}+f_{cb}) \tag{7.3.3}$$

$$\frac{N_{4b}}{2} = \mathcal{L}\sigma_{t\bar{t}}\mathcal{BF}\epsilon_0\epsilon_b^2 f_{lb}(f_{lb}+f_{cb}), \tag{7.3.4}$$

where the luminosity ($\mathcal{L}$), the $t\bar{t}$ cross-section ($\sigma_{t\bar{t}}$) and the branching fraction ($\mathcal{BF}$) are taken from Table 5.1 and the gluon-modified mistag rates are used. Performing a sum over the above equations yields the result $\epsilon_0 = 0.025$,

compared to the assumed by the feasibility study value of $\epsilon_0 = 0.1$ (Table 5.1). Substituting the modified mistag rates and the reconstruction efficiency into the expression for the statistical uncertainty of the feasibility study (Equation 5.3.8), its value is found to be $\Delta_{\text{stat.}}|V_{cb}|/|V_{cb}| = 0.14$, a value compatible with the total statistical error extracted using the TRExFitter framework (Equation 7.2.4). This result shows the discrepancy between the statistical uncertainty of the cut-and-count method of the feasibility study and the one of the binned likelihood fit using the full ATLAS MC event samples to be due to the presence of gluon jets and jets originating from pile-up. Therefore, an improvement to the statistical uncertainty of the measurement could be achieved by developing further techniques which identify and reject events containing such jets, in combination with the additional events recorded during Large Hadron Collider (LHC) Run-3 and the High Luminosity Large Hadron Collider (HL-LHC) operation period.

Figure 7.3 shows the leading contributions to the systematic uncertainty of Equation 7.2.4 to be related to jet flavour tagging. The contribution to the total systematic uncertainty of $|V_{cb}|$ by the group of b-tagging related systematics (Figure 7.2) is estimated to be $\Delta\mu_b = \sqrt{(\Delta\mu)^2 - (\Delta\mu')^2} = 0.08$, where $\Delta\mu$ is defined as the uncertainty of the PoI when considering all systematic uncertainties in the fit, and $\Delta\mu'$ - the uncertainty of the PoI when excluding the b-tagging related systematics. The contribution due to MC pile-up reweighting is estimated to be $\Delta\mu_{\text{pile-up}} = 0.02$, with the remainder of the systematic uncertainty originating mostly from jet reconstruction. Substituting the modified mistag rates into the systematic uncertainty in Equation 5.3.8 yields an overestimation of the result, $\Delta_{\text{syst.}}|V_{cb}|/|V_{cb}| = 0.12$. Moreover, the feasibility study only assumes flavour tagging systematics, while the binned likelihood fit includes most standard ATLAS sources of systematic uncertainty (additional sources of systematic uncertainties not yet included in the fit are discussed in Section 7.4.2). A reduction in $\Delta\mu_b$ can be achieved by improvements in the flavour tagging algorithm which are going to be introduced during LHC Run 3.

The total measurement uncertainty (Equation 7.2.4) is $\sim \mathcal{O}(10)$ times larger than the uncertainties in past measurements of $|V_{cb}|$ using inclusive and exclusive B-meson decays. Nevertheless, the strategy presented in this thesis provides an independent measurement of the CKM matrix element in top quark decays. In contrast to B-meson decay measurements in which the biggest sources of uncertainty originate from external inputs (e.g. [12, 137]), the above result is not dependent on theory.

7.4 Conclusion and future work

7.4.1 Conclusion

A preliminary estimation of the sensitivity of the measurement of the Cabibbo-Kobayashi-Maskawa (CKM) matrix element $|V_{cb}|$ was made using ATLAS MC samples of semi-leptonic $t\bar{t}$ decays. The MC samples correspond to the data recorded during the full LHC Run 2 (139 fb^{-1}) with centre-of-mass energy of $\sqrt{s} = 13$ TeV. The distribution of the scalar sum of the transverse momenta of the hadronically decaying W boson daughters was used to extract the uncertainty on the normalisation factor of $|V_{cb}|$ from a combined sample of signal, $t\bar{t}$ background and non-$t\bar{t}$ background events. The extracted value of the fractional uncertainty of the measurement using an extended binned profile likelihood fit in the ATLAS TRExFitter framework was evaluated to be $\Delta|V_{cb}|/|V_{cb}| = 0.14(\text{stat.}) \oplus 0.10(\text{syst.})$, which is not currently competitive with the uncertainties of past measurements in inclusive and exclusive B-meson decays.

7.4.2 Future work

An improvement of the measurement's statistical uncertainty can be achieved by the inclusion of higher jet multiplicity $t\bar{t}$ events, as well as single top MC events containing the $|V_{cb}|$ matrix element. In addition, data collected during LHC Run 3, as well as from the HL-LHC will also reduce the statistical uncertainty.

The extracted systematic error does not contain the complete set of sources of uncertainty. The analysis presented in this thesis used mutually exclusive b- and c-tagging working points (WPs), with the c-tagging WP being an unofficial one - additional systematic uncertainties connected to the scale factors (SFs) which correct the MC efficiencies and mistag rates could contribute to the total error of the measurement. The 4b-tag region was not used in the fit due to contamination by $t\bar{t}b\bar{b}$ events - $t\bar{t}$ events which have additional pairs of b-quarks generated by QCD processes. The fraction of events which contain such pairs are known to be underestimated in the nominal Powheg+Pythia8 ATLAS MC sample, requiring the use of alternative samples to estimate the effect. Alternative $t\bar{t}$ samples can also be utilised to estimate the uncertainty of the theoretical models employed by different matrix element and parton shower generators by comparing event yields and distributions in the samples listed in Table 6.7. Additional modelling uncertainties arise from the variation of the Monte Carlo event generator (MCEG) tune, as well as from the variation of the final state radiation (FSR) and initial state radiation (ISR).

Appendix A

Auxiliary figures and tables

A.1 LHC operation periods

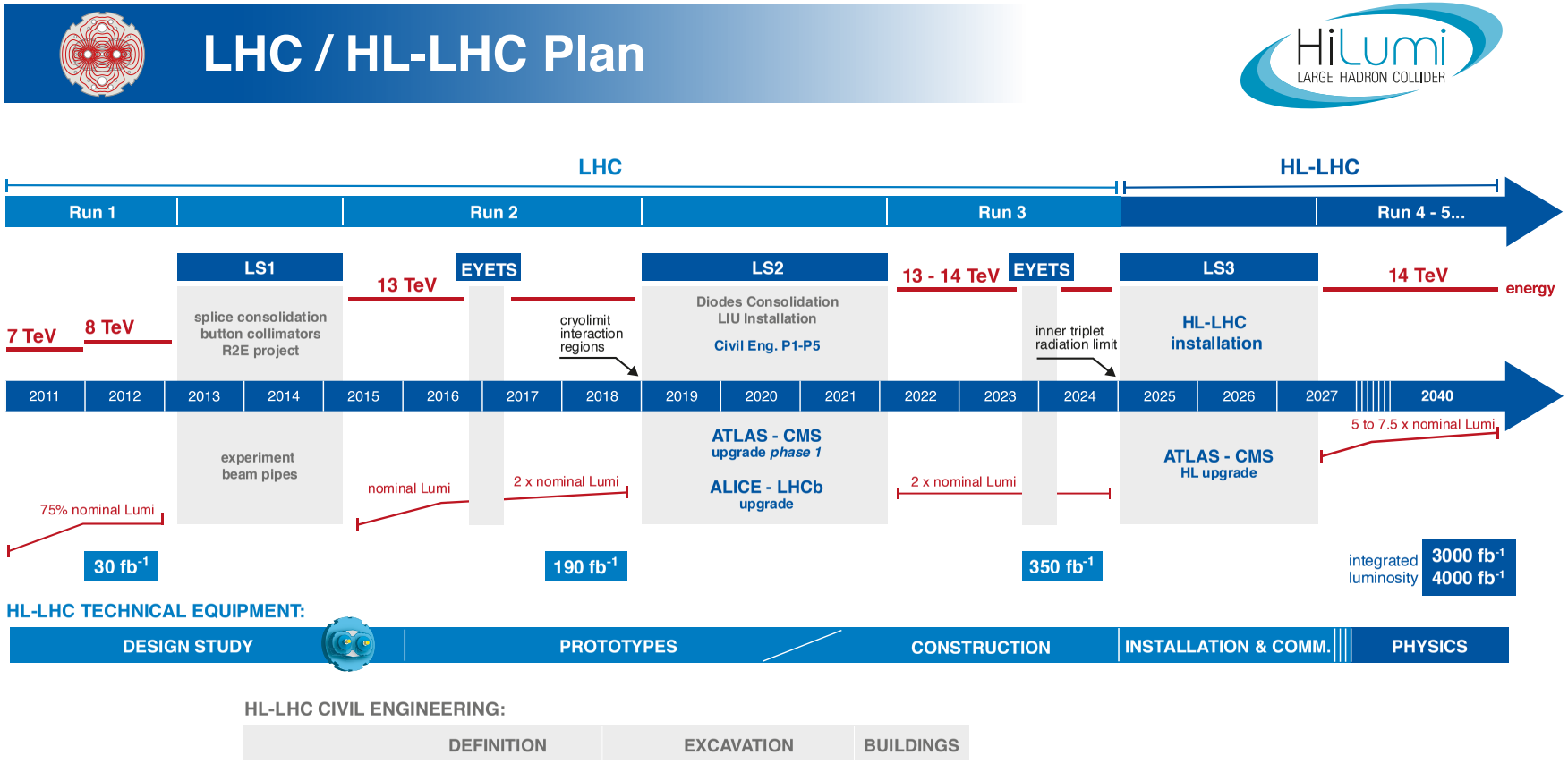

Figure A.1: Timeline of past and planned LHC operation periods. EYETS periods represent Extended Year-End Technical Stops. Taken from Ref. [54].

A.2 Non-LepHad $t\bar{t}$ backgrounds

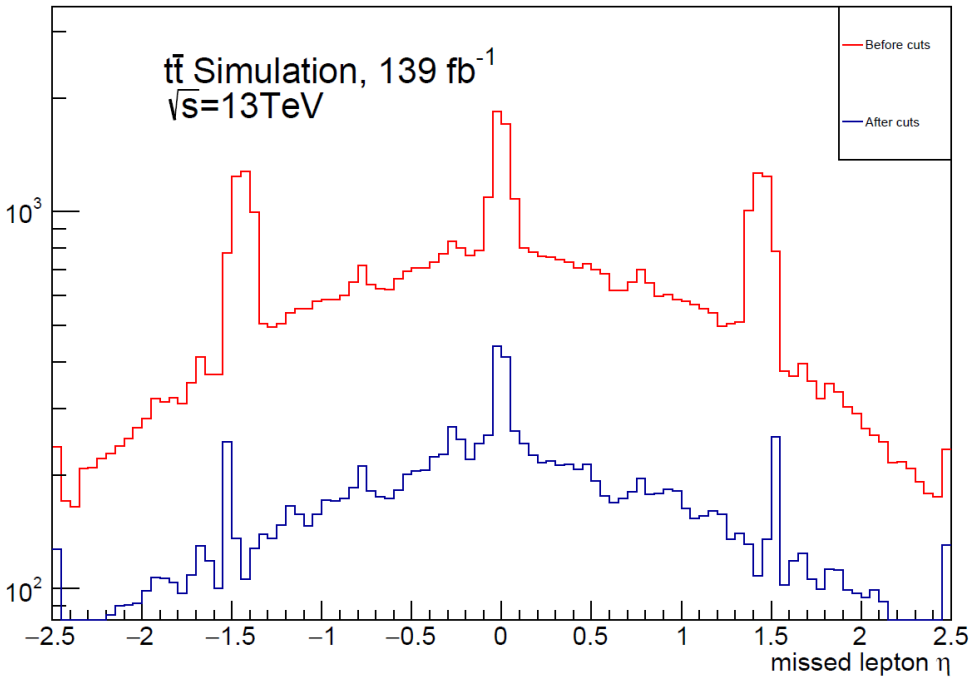

Figure A.2: Pseudorapidity of the missed lepton of truth $\ell + \ell$ $t\bar{t}$ events. The red (blue) curve represents the distribution before (after) the application of the cuts introduced in Section 6.2.2. The peaks correspond to a gap in the muon spectrometer around $|\eta| = 0$ and the gaps in the ECal at $1.37 < |\eta_{\text{cluster}}| < 1.52$.

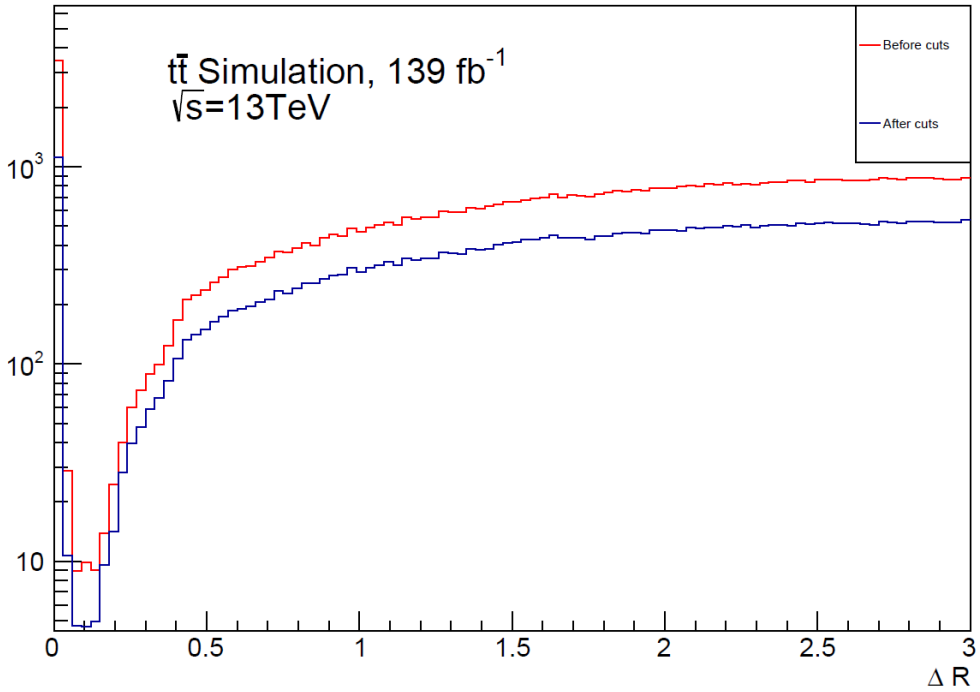

Figure A.3: Angular distance (ΔR) between the truth τ and the reconstructed lepton in truth $\ell + \tau$ $t\bar{t}$ events. The red (blue) curve represents the distribution before (after) the application of the cuts introduced in Section 6.2.2.

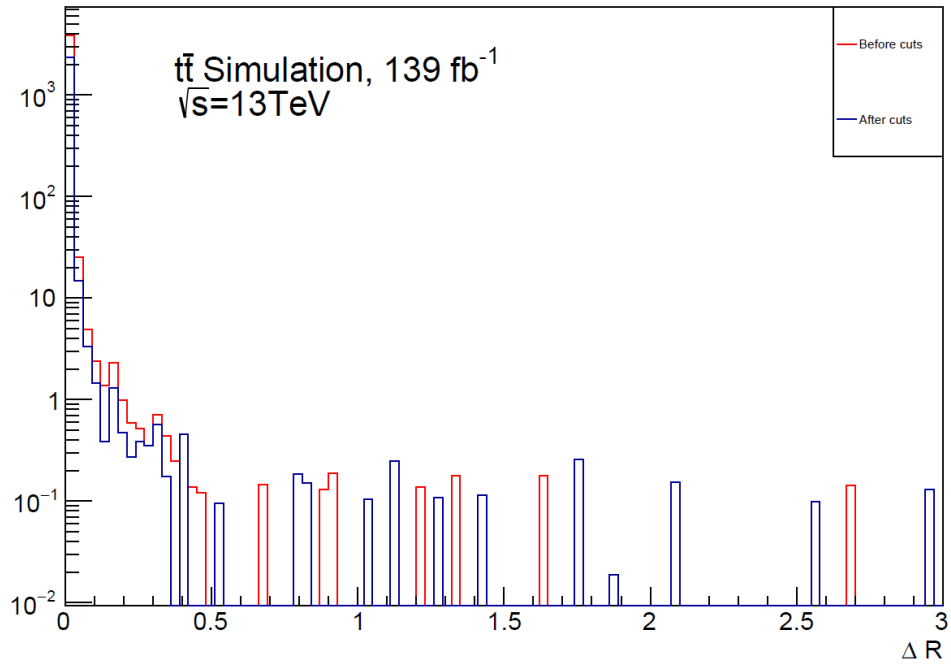

Figure A.4: Angular distance (ΔR) between the closest truth τ and the reconstructed lepton in truth $\tau + \tau$ $t\bar{t}$ events. The red (blue) curve represents the distribution before (after) the application of the cuts introduced in Section 6.2.2.

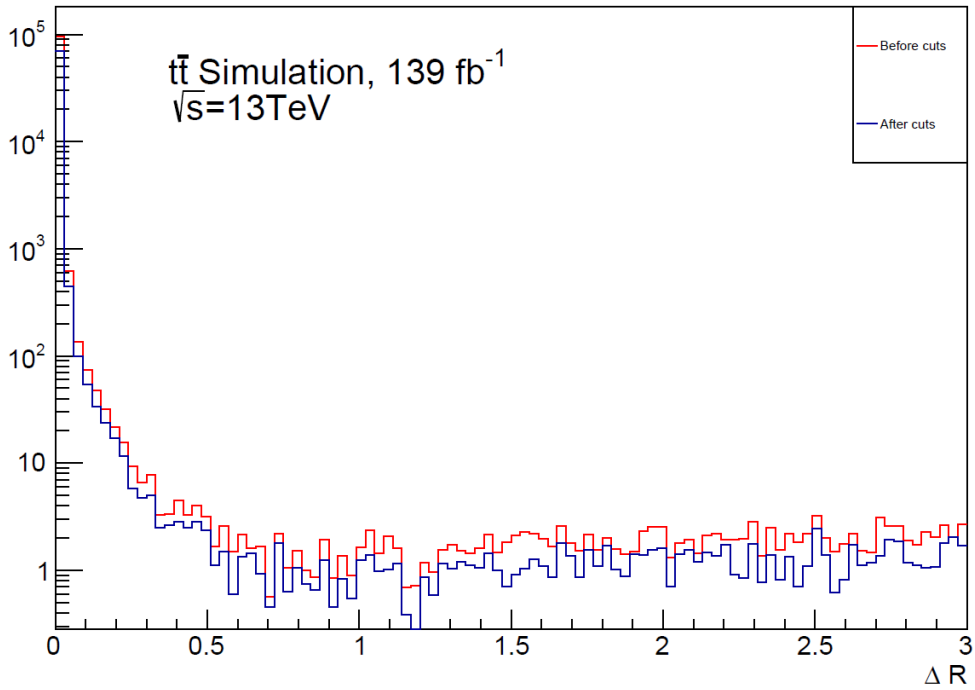

Figure A.5: Angular distance (ΔR) between the truth τ and the reconstructed lepton in truth τ+jets $t\bar{t}$ events. The red (blue) curve represents the distribution before (after) the application of the cuts introduced in Section 6.2.2.

A.3 Jet flavour composition and flavour response

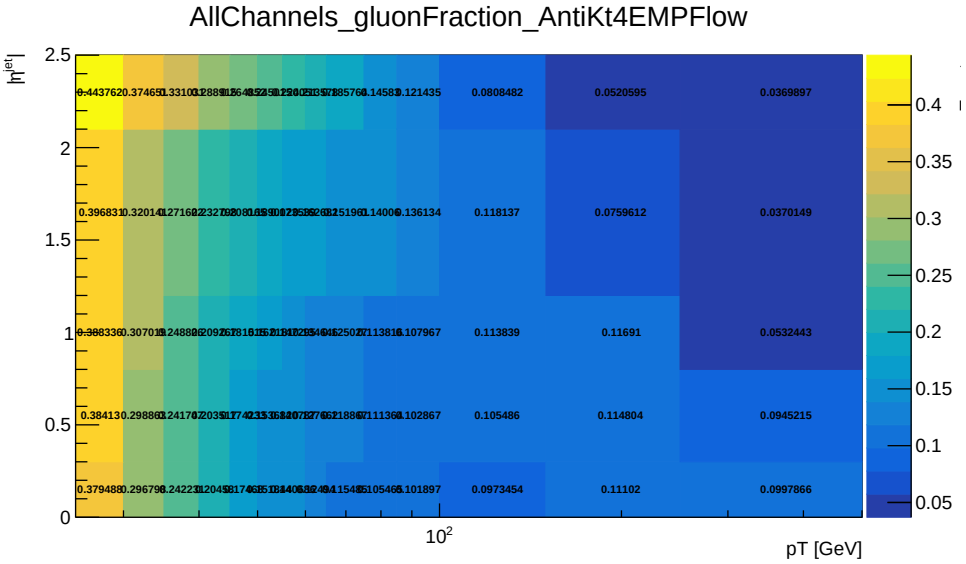

(a) gluon fraction

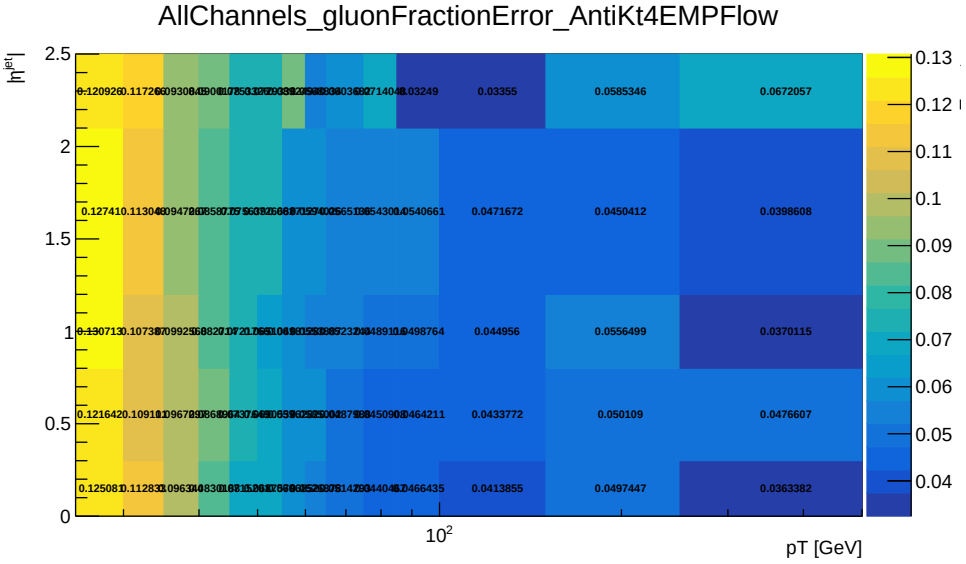

(b) gluon fraction uncertainty

Figure A.6: Gluon fraction (f_g) and its uncertainty (Δf_g) derived for $t\bar{t}$ events satisfying the analysis selection in MC16a Monte Carlo subcampaign sample.

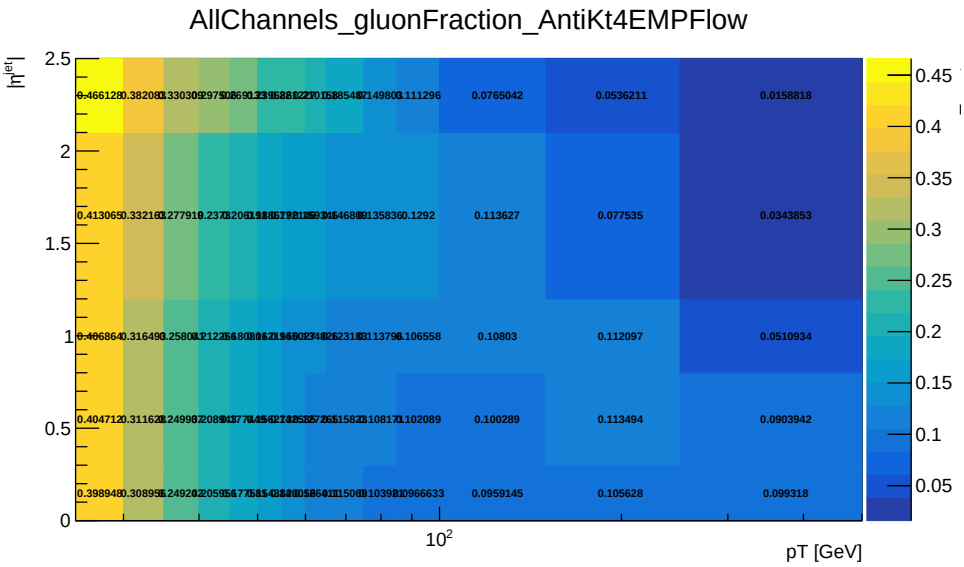

(a) gluon fraction

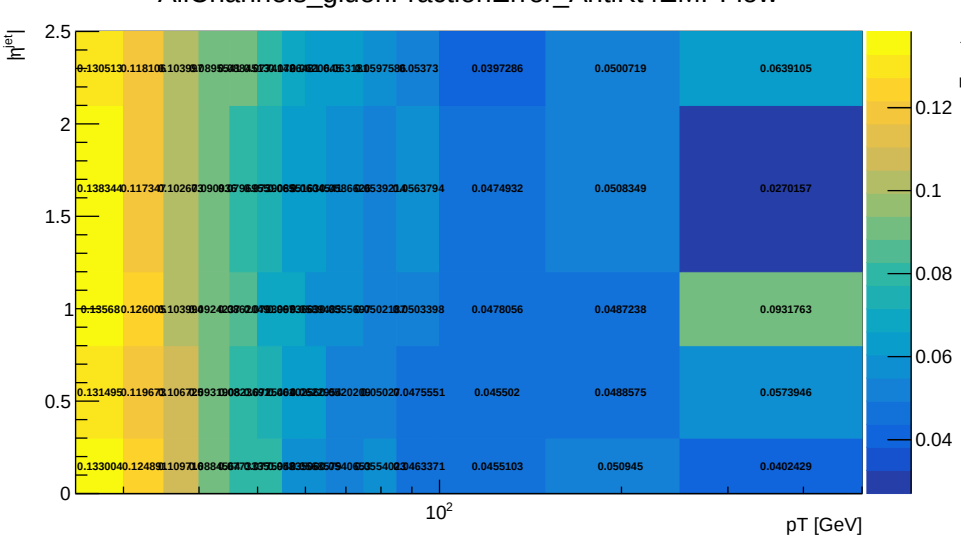

(b) gluon fraction uncertainty

Figure A.7: Gluon fraction (f_g) and its uncertainty (Δf_g) derived for $t\bar{t}$ events satisfying the analysis selection in MC16d Monte Carlo subcampaign sample.

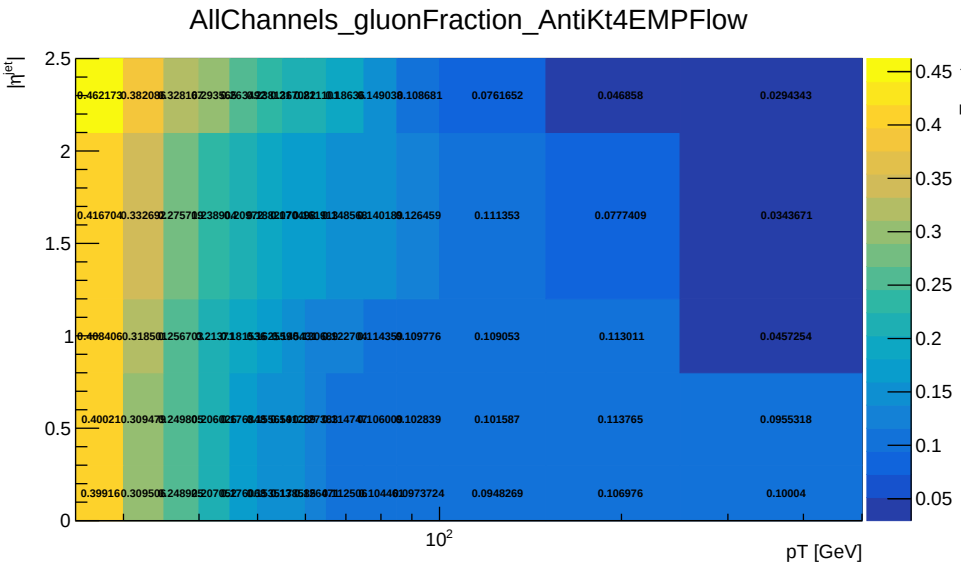

(a) gluon fraction

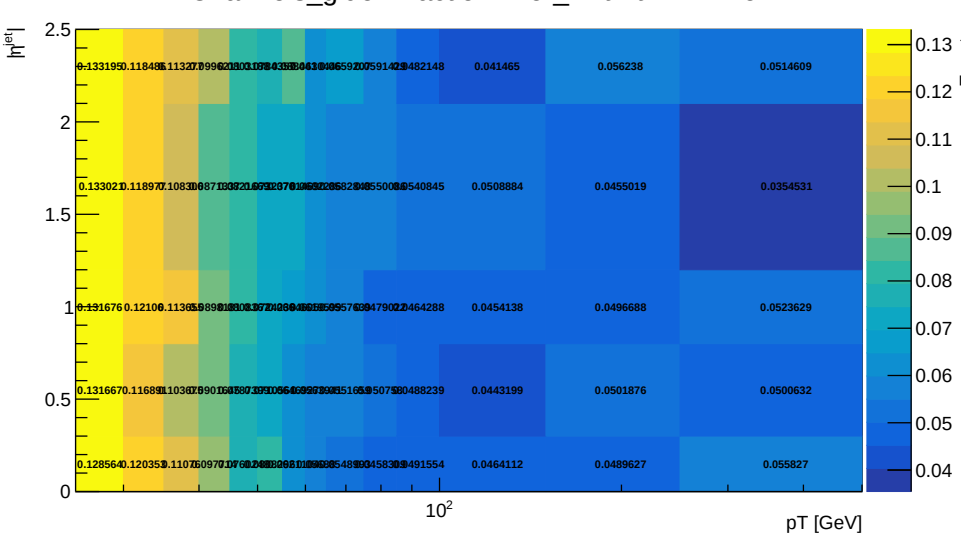

(b) gluon fraction uncertainty

Figure A.8: Gluon fraction (f_g) and its uncertainty (Δf_g) derived for $t\bar{t}$ events satisfying the analysis selection in MC16e Monte Carlo subcampaign sample.

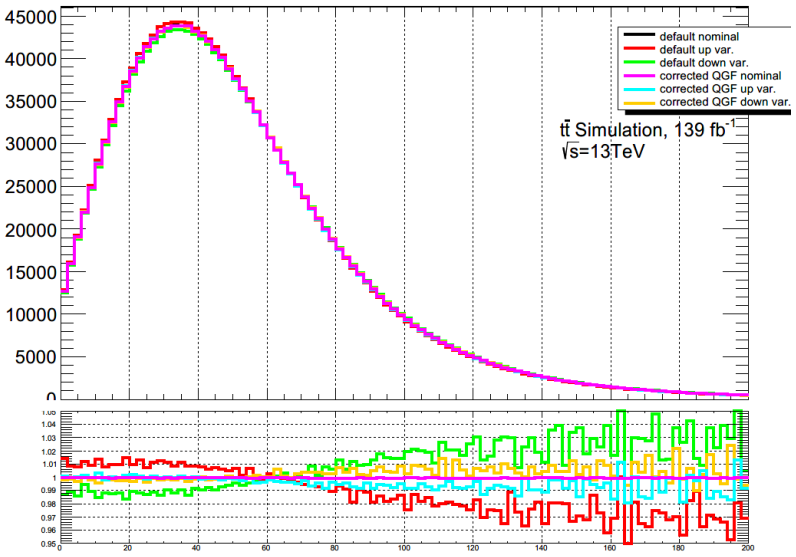

(a) jet flavour response

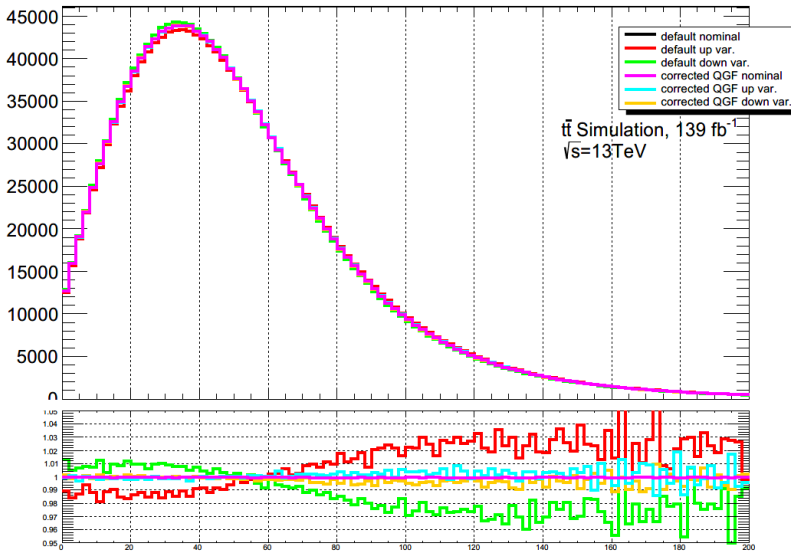

(b) jet flavour composition

Figure A.9: Comparison of uncertainties in event MET due to the default quark gluon fraction ($f_g \pm \Delta f_g = 0.5 \pm 0.5$) and the custom analysis values in the Non-AllHad $t\bar{t}$ events satisfying the analysis selection criteria. The difference in uncertainties are shown for jet flavour response (a) and jet flavour composition (b). The different colours represent the default nominal values (black), the default $+1\sigma$ variation (red), the default -1σ variation (green), the custom nominal (magenta) (no difference from the default nominal values expected), the custom $+1\sigma$ variation (blue) and the custom -1σ variation (yellow). The panels below the histograms show the ratio of each distribution to the default nominal values.

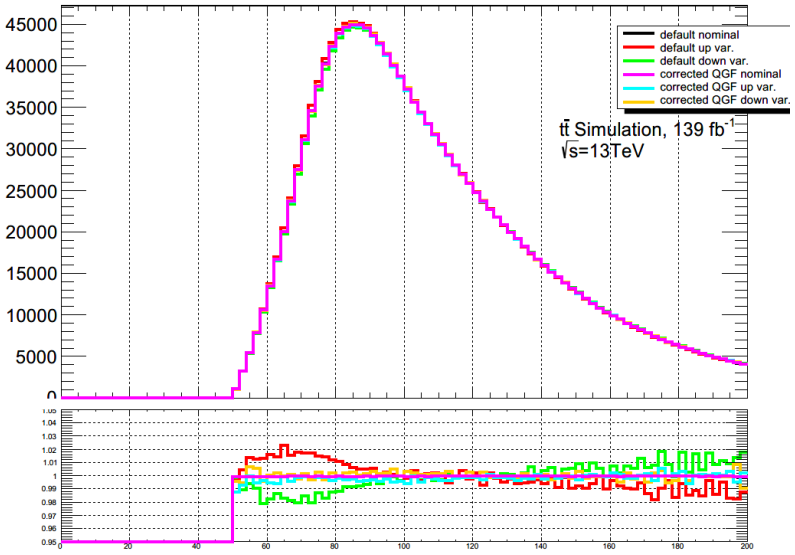

(a) jet flavour response

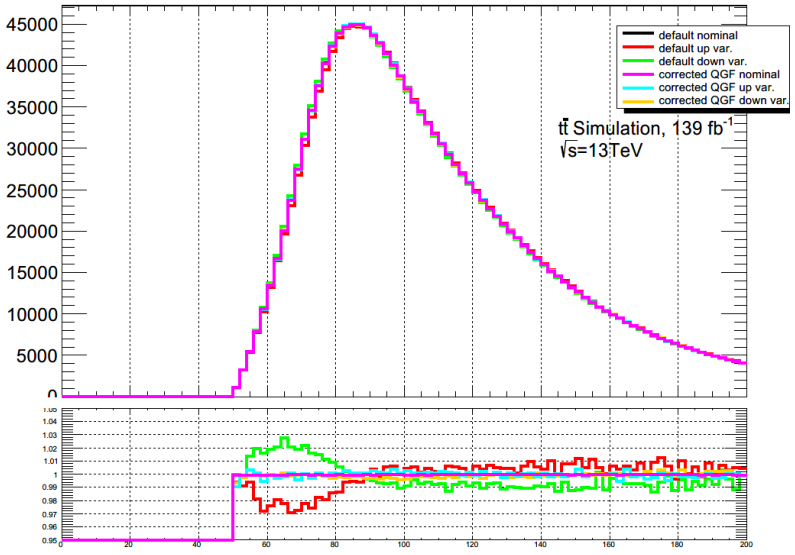

(b) jet flavour composition

Figure A.10: Comparison of uncertainties in the sum of hadronic W daughter p_T due to the default quark gluon fraction ($f_g \pm \Delta f_g = 0.5 \pm 0.5$) and the custom analysis values in the Non-AllHad $t\bar{t}$ events satisfying the analysis selection criteria. The difference in uncertainties are shown for jet flavour response (a) and jet flavour composition (b). The different colours represent the default nominal values (black), the default $+1\sigma$ variation (red), the default -1σ variation (green), the custom nominal (magenta) (no difference from the default nominal values expected), the custom $+1\sigma$ variation (blue) and the custom -1σ variation (yellow). The panels below the histograms show the ratio of each distribution to the default nominal values.

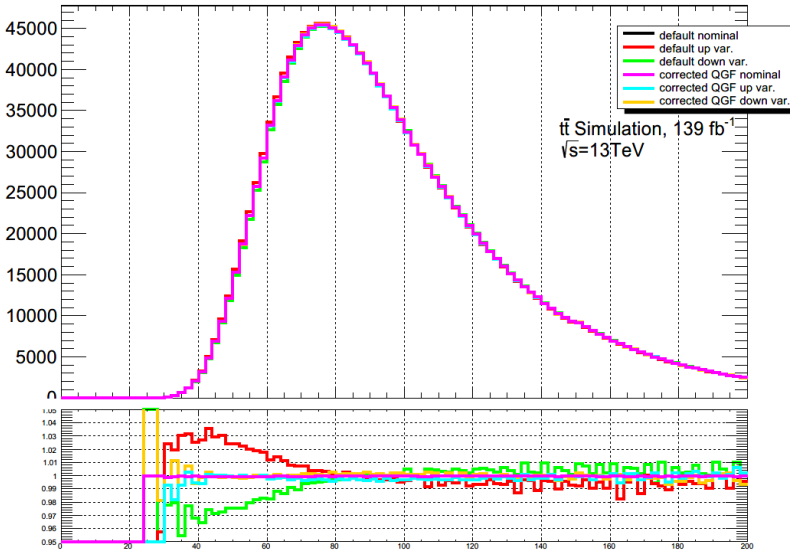

(a) jet flavour response

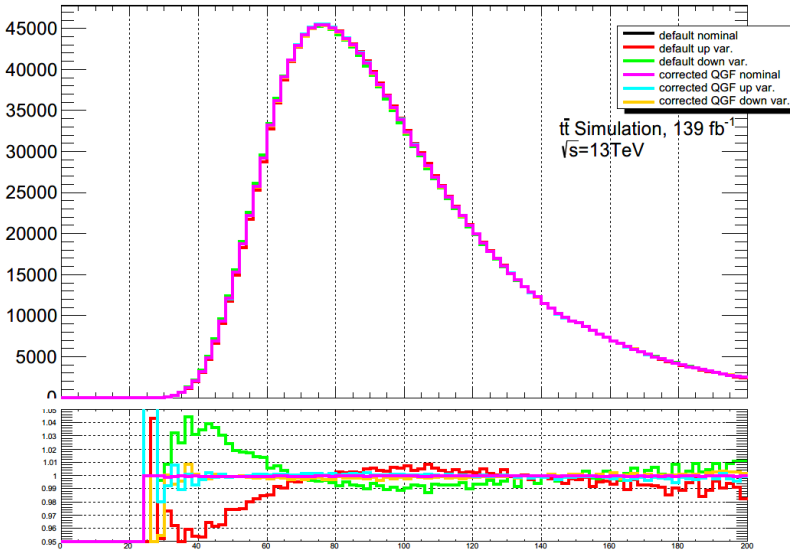

(b) jet flavour composition

Figure A.11: Comparison of uncertainties in the leading jet (highest p_T jet in event) p_T due to the default quark gluon fraction ($f_g \pm \Delta f_g = 0.5 \pm 0.5$) and the custom analysis values in the Non-AllHad $t\bar{t}$ events satisfying the analysis selection criteria. The difference in uncertainties are shown for jet flavour response (a) and jet flavour composition (b). The different colours represent the default nominal values (black), the default $+1\sigma$ variation (red), the default -1σ variation (green), the custom nominal (magenta) (no difference from the default nominal values expected), the custom $+1\sigma$ variation (blue) and the custom -1σ variation (yellow). The panels below the histograms show the ratio of each distribution to the default nominal values.

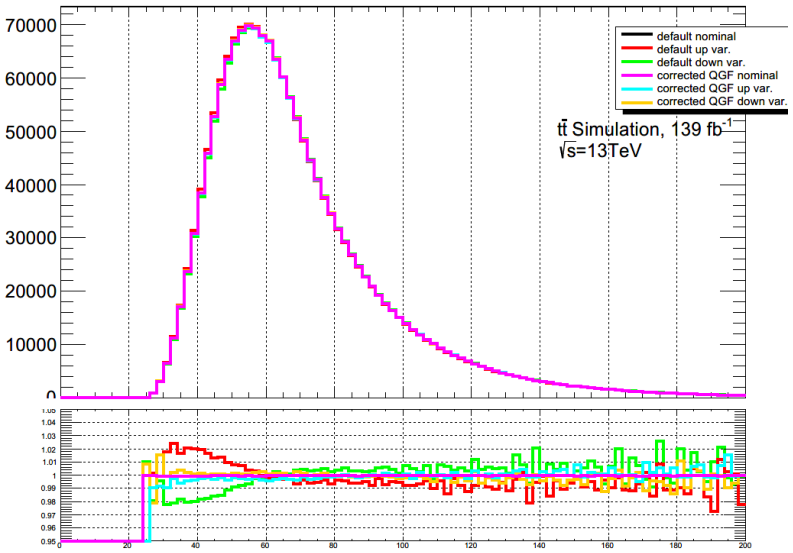

(a) jet flavour response

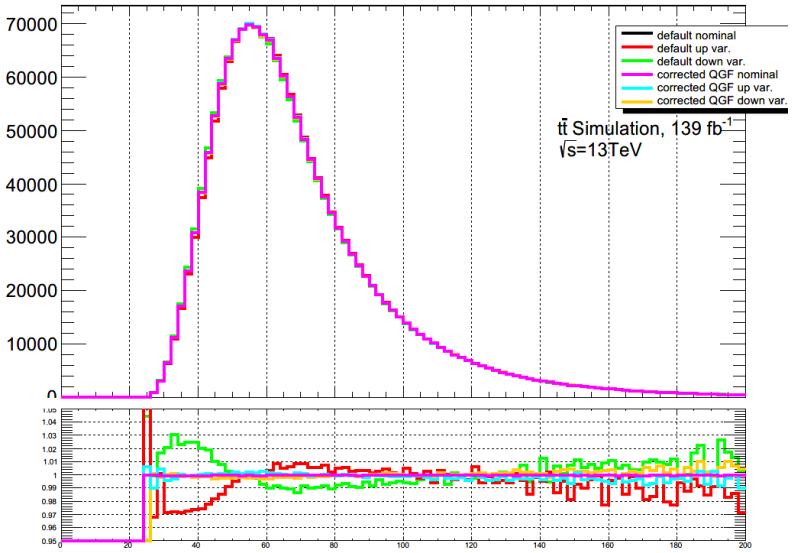

(b) jet flavour composition

Figure A.12: Comparison of uncertainties in the sub-leading jet (second highest p_T jet in event) p_T due to the default quark gluon fraction ($f_g \pm \Delta f_g = 0.5 \pm 0.5$) and the custom analysis values in the Non-AllHad $t\bar{t}$ events satisfying the analysis selection criteria. The difference in uncertainties are shown for jet flavour response (a) and jet flavour composition (b). The different colours represent the default nominal values (black), the default $+1\sigma$ variation (red), the default -1σ variation (green), the custom nominal (magenta) (no difference from the default nominal values expected), the custom $+1\sigma$ variation (blue) and the custom -1σ variation (yellow). The panels below the histograms show the ratio of each distribution to the default nominal values.

A.4 Correlation of systematic uncertainties

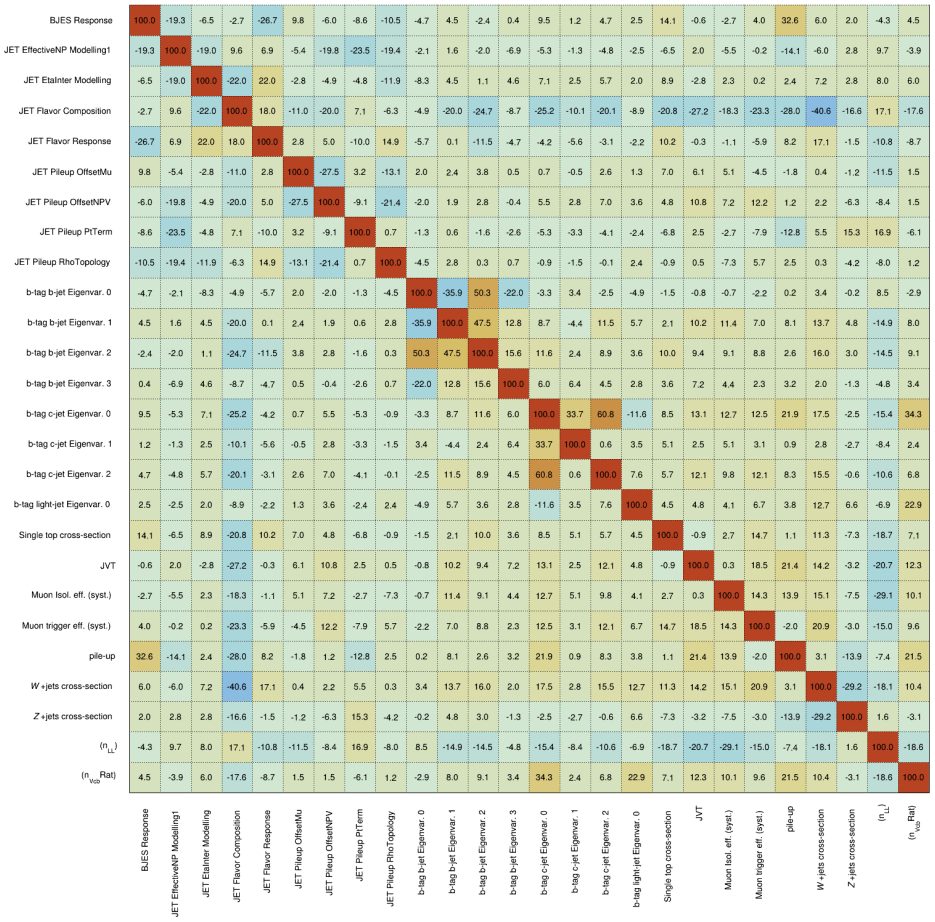

Figure A.13: Correlation matrix of the NPs which have at least 20% correlation with another parameter in the fit.

Bibliography

[1] P. F. Harrison and V. E. Vladimirov, JHEP **01**, 191 (2019), arXiv:1810.09424 [hep-ph] .

[2] R. Brun, F. Rademakers, P. Canal, A. Naumann, O. Couet, L. Moneta, V. Vassilev, S. Linev, D. Piparo, G. GANIS, B. Bellenot, E. Guiraud, G. Amadio, wverkerke, P. Mato, and TimurP, "root-project/root: v6.18/02," (2019).

[3] I. Antcheva, M. Ballintijn, B. Bellenot, M. Biskup, R. Brun, N. Buncic, P. Canal, D. Casadei, O. Couet, V. Fine, and et al., Computer Physics Communications **180**, 2499–2512 (2009).

[4] T. Aoyama, T. Kinoshita, and M. Nio, Atoms **7** (2019), 10.3390/atoms7010028.

[5] J. Chay, H. Georgi, and B. Grinstein, Phys. Lett. B **247**, 399 (1990).

[6] A. V. Manohar and M. B. Wise, Physical Review D **49**, 1310–1329 (1994).

[7] O. Buchmuller and H. Flacher, Phys. Rev. D **73**, 073008 (2006), arXiv:hep-ph/0507253 .

[8] Y. S. Amhis *et al.* (HFLAV), Eur. Phys. J. **C81**, 226 (2021), updated results and plots available at `https://hflav.web.cern.ch/`, arXiv:1909.12524 [hep-ex] .

[9] P. Zyla *et al.* (Particle Data Group), PTEP **2020**, 083C01 (2020).

[10] W. MENGES, Deep Inelastic Scattering DIS 2006 (2007), 10.1142/9789812706706_0085.

[11] CERN Courier Volume 60, Number 1, January/February 2020, https://cds.cern.ch/record/2706508.

[12] R. Aaij, C. Abellán Beteta, T. Ackernley, B. Adeva, M. Adinolfi, H. Afsharnia, C. Aidala, S. Aiola, Z. Ajaltouni, S. Akar, and et al., Physical Review D **101** (2020), 10.1103/physrevd.101.072004.

[13] C. Balzereit, T. Mannel, and B. Plumper, Eur. Phys. J. **C9**, 197 (1999), arXiv:hep-ph/9810350 [hep-ph] .

[14] M. Srednicki, *Quantum field theory* (Cambridge University Press, 2007).

[15] A. Zannoni, On the Quantization of the Monoatomic Ideal Gas (2000).

[16] P. A. M. Dirac, Proceedings of the Royal Society of London. Series A, Containing Papers of a Mathematical and Physical Character **112**, 661 (1926).

[17] W. Pauli, Zeitschrift fur Physik **31**, 765 (1925).

[18] Bose, Zeitschrift fur Physik **26**, 178 (1924).

[19] A. Tureanu, J. Phys. Conf. Ser. **474**, 012031 (2013).

[20] C. S. Wu, E. Ambler, R. W. Hayward, D. D. Hoppes, and R. P. Hudson, Phys. Rev. **105**, 1413 (1957).

[21] J. H. Christenson, J. W. Cronin, V. L. Fitch, and R. Turlay, Phys. Rev. Lett. **13**, 138 (1964).

[22] M. E. Peskin and D. V. Schroeder, *An Introduction to quantum field theory* (Addison-Wesley, Reading, USA, 1995).

[23] H. Fritzsch, M. Gell-Mann, and H. Leutwyler, Phys. Lett. B **47**, 365 (1973).

[24] L. collaboration, Science Bulletin **65**, 1983 (2020).

[25] R. Aaij *et al.* (LHCb), Phys. Rev. Lett. **115**, 072001 (2015), arXiv:1507.03414 [hep-ex] .

[26] D. J. Gross and F. Wilczek, Phys. Rev. Lett. **30**, 1343 (1973).

[27] K. G. Wilson, Phys. Rev. D **10**, 2445 (1974).

[28] R. Alkofer and J. Greensite, Journal of Physics G: Nuclear and Particle Physics **34**, S3–S21 (2007).

[29] S. L. Glashow, Nucl. Phys. **10**, 107 (1959).

[30] S. Weinberg, Phys. Rev. Lett. **19**, 1264 (1967).

[31] A. Salam, Conf. Proc. C **680519**, 367 (1968).

[32] G. Senjanovic and V. Tello, (2020), arXiv:2004.04036 [hep-ph] .

[33] W. Herr and B. Muratori, (2006), 10.5170/CERN-2006-002.361.

[34] M. Hostettler, F. Antoniou, I. Efthymiopoulos, K. Fuchsberger, G. Iadarola, N. Karastathis, M. Lamont, Y. Papaphilippou, G. Papotti, and J. Wenninger, in *8th International Particle Accelerator Conference* (2017).

[35] L. Evans and P. Bryant, Journal of Instrumentation **3**, S08001 (2008).

[36] B. Salvachua, Overview of Proton-Proton Physics during Run 2 , 7 (2019).

[37] J. D. Bjorken and E. A. Paschos, Phys. Rev. **185**, 1975 (1969).

[38] V. N. Gribov and L. N. Lipatov, Sov. J. Nucl. Phys. **15**, 438 (1972).

[39] G. Altarelli and G. Parisi, Nucl. Phys. B **126**, 298 (1977).

[40] Y. L. Dokshitzer, Sov. Phys. JETP **46**, 641 (1977).

[41] L. A. Harland-Lang, A. D. Martin, P. Motylinski, and R. S. Thorne, The European Physical Journal C **75** (2015), 10.1140/epjc/s10052-015-3397-6.

[42] J. C. Collins and D. E. Soper, Nucl. Phys. B **194**, 445 (1982).

[43] A. Sirunyan, A. Tumasyan, W. Adam, F. Ambrogi, E. Asilar, T. Bergauer, J. Brandstetter, M. Dragicevic, J. Erö, A. Escalante Del Valle, and et al., Physical Review D **100** (2019), 10.1103/physrevd.100.072002.

[44] "LHC Top Working group Summary plots," `https://twiki.cern.ch/twiki/bin/view/LHCPhysics/LHCTopWGSummaryPlots` (), accessed 2021-09-04.

[45] E. Mobs, (2018), general photo, available at https://cds.cern.ch/record/2636343.

[46] R. Scrivens and M. Vretenar, Linac2: The tale of a billion-trillion protons (2018).

[47] L. Rossi, Conf. Proc. C **030512**, 141 (2003).

[48] *Luminosity determination in pp collisions at* $\sqrt{s} = 13$ *TeV using the ATLAS detector at the LHC*, Tech. Rep. (CERN, Geneva, 2019) all figures including auxiliary figures are available at https://atlas.web.cern.ch/Atlas/GROUPS/PHYSICS/CONFNOTES/ATLAS-CONF-2019-021.

[49] T. A. Collaboration, Journal of Instrumentation **3**, S08003 (2008).

[50] S. Chatrchyan *et al.* (CMS), JINST **3**, S08004 (2008).

[51] K. Aamodt *et al.* (ALICE), JINST **3**, S08002 (2008).

[52] A. A. Alves, Jr. *et al.* (LHCb), JINST **3**, S08005 (2008).

[53] O. Aberle *et al.*, *High-Luminosity Large Hadron Collider (HL-LHC): Technical design report*, CERN Yellow Reports: Monographs (CERN, Geneva, 2020).

[54] "High luminosity lhc project," `https://hilumilhc.web.cern.ch/content/hl-lhc-project`, accessed: 2021-07-28.

[55] T. Cornelissen, M. Elsing, S. Fleischmann, W. Liebig, and E. Moyse, (2007).

[56] A. Salzburger, Journal of Physics: Conference Series **664**, 072042 (2015).

[57] E. Stanecka (ATLAS), Acta Phys. Polon. B **47**, 1739 (2016).

[58] K. Potamianos, PoS **EPS-HEP2015**, 261 (2015), arXiv:1608.07850 [physics.ins-det] .

[59] G. Aad *et al.* (ATLAS), JINST **9**, P08009 (2014), arXiv:1404.7473 [hep-ex] .

[60] M. Aleksa and M. Diemoz, *Discussion on the electromagnetic calorimeters of ATLAS and CMS*, Tech. Rep. (CERN, Geneva, 2013).

[61] J. Pequenao, "Computer Generated image of the ATLAS calorimeter," (2008).

[62] A. Henriques (ATLAS), in *4th International Conference on Advancements in Nuclear Instrumentation Measurement Methods and their Applications*, IEEE Nucl.Sci.Symp.Conf.Rec. (2015) p. 7465554.

[63] G. Aad, B. Abbott, J. Abdallah, O. Abdinov, B. Abeloos, R. Aben, M. Abolins, O. S. AbouZeid, N. L. Abraham, and et al., The European Physical Journal C **76** (2016), 10.1140/epjc/s10052-016-4120-y.

[64] L. Pontecorvo, (2003), 10.1140/epjcd/s2004-04-013-y, revised version number 1 submitted on 2003-07-27 16:31:16.

[65] G. Aad, B. Abbott, J. Abdallah, S. Abdel Khalek, O. Abdinov, R. Aben, B. Abi, M. Abolins, O. S. AbouZeid, and et al., The European Physical Journal C **75** (2015), 10.1140/epjc/s10052-015-3325-9.

[66] *ATLAS Computing: technical design report*, Technical design report. ATLAS (CERN, Geneva, 2005).

[67] J. Pequenao, "Event Cross Section in a computer generated image of the ATLAS detector." (2008), https://cds.cern.ch/record/1096081, Accessed: 07/07/2021.

[68] R. Fruhwirth, Nucl. Instrum. Meth. A **262**, 444 (1987).

[69] M. Aaboud, G. Aad, B. Abbott, J. Abdallah, O. Abdinov, B. Abeloos, S. H. Abidi, O. S. AbouZeid, N. L. Abraham, and et al., The European Physical Journal C **77** (2017), 10.1140/epjc/s10052-017-5225-7.

[70] T. Cornelissen, M. Elsing, I. Gavrilenko, W. Liebig, E. Moyse, and A. Salzburger, Journal of Physics: Conference Series **119**, 032014 (2008).

[71] M. Aaboud, G. Aad, B. Abbott, J. Abdallah, O. Abdinov, B. Abeloos, R. Aben, O. S. AbouZeid, N. L. Abraham, and et al., The European Physical Journal C **77** (2017), 10.1140/epjc/s10052-017-4887-5.

[72] G. Aad, B. Abbott, J. Abdallah, O. Abdinov, R. Aben, M. Abolins, O. S. AbouZeid, H. Abramowicz, H. Abreu, and et al., The European Physical Journal C **77** (2017), 10.1140/epjc/s10052-017-5004-5.

[73] S. Schramm (ATLAS Collaboration), *ATLAS Jet Reconstruction, Calibration, and Tagging of Lorentz-boosted Objects*, Tech. Rep. (CERN, Geneva, 2017).

[74] *Improved electron reconstruction in ATLAS using the Gaussian Sum Filter-based model for bremsstrahlung*, Tech. Rep. (CERN, Geneva, 2012) all figures including auxiliary figures are available at https://atlas.web.cern.ch/Atlas/GROUPS/PHYSICS/CONFNOTES/ATLAS-CONF-2012-047.

[75] G. Aad, B. Abbott, D. Abbott, A. A. Abud, K. Abeling, D. Abhayasinghe, S. Abidi, O. AbouZeid, N. Abraham, H. Abramowicz, and et al., Journal of Instrumentation **14**, P12006–P12006 (2019).

[76] G. Aad, B. Abbott, D. C. Abbott, A. A. Abud, K. Abeling, D. K. Abhayasinghe, S. H. Abidi, O. S. AbouZeid, N. L. Abraham, and et al., The European Physical Journal C **80** (2020), 10.1140/epjc/s10052-019-7500-2.

[77] M. Aaboud, G. Aad, B. Abbott, D. C. Abbott, O. Abdinov, B. Abeloos, D. K. Abhayasinghe, S. H. Abidi, O. S. AbouZeid, and et al., The European Physical Journal C **79** (2019), 10.1140/epjc/s10052-019-7140-6.

[78] M. Aaboud, G. Aad, B. Abbott, J. Abdallah, O. Abdinov, B. Abeloos, R. Aben, O. S. AbouZeid, N. L. Abraham, and et al., The European Physical Journal C **77** (2017), 10.1140/epjc/s10052-017-4852-3.

[79] S. D. Jones (ATLAS Collaboration), *The ATLAS Electron and Photon Trigger*, Tech. Rep. (CERN, Geneva, 2017).

[80] G. Aad *et al.* (ATLAS), Eur. Phys. J. C **81**, 578 (2021), arXiv:2012.00578 [hep-ex] .

[81] G. Aad, B. Abbott, J. Abdallah, O. Abdinov, B. Abeloos, R. Aben, M. Abolins, O. S. AbouZeid, N. L. Abraham, and et al., The European Physical Journal C **76** (2016), 10.1140/epjc/s10052-016-4120-y.

[82] G. Aad, B. Abbott, D. Abbott, A. A. Abud, K. Abeling, D. Abhayasinghe, S. Abidi, O. AbouZeid, N. Abraham, H. Abramowicz, and et al., Journal of Instrumentation **15**, P09015–P09015 (2020).

[83] G. P. Salam, The European Physical Journal C **67**, 637–686 (2010).

[84] M. Cacciari, G. P. Salam, and G. Soyez, JHEP **04**, 063 (2008), arXiv:0802.1189 [hep-ph] .

[85] M. Aaboud, G. Aad, B. Abbott, J. Abdallah, O. Abdinov, B. Abeloos, S. H. Abidi, O. S. AbouZeid, N. L. Abraham, and et al., The European Physical Journal C **77** (2017), 10.1140/epjc/s10052-017-5031-2.

[86] *E_T^{miss} performance in the ATLAS detector using 2015-2016 LHC p-p collisions*, Tech. Rep. (CERN, Geneva, 2018) all figures including auxiliary figures are available at https://atlas.web.cern.ch/Atlas/GROUPS/PHYSICS/CONFNOTES/ATLAS-CONF-2018-023.

[87] *Tagging and suppression of pileup jets with the ATLAS detector*, Tech. Rep. (CERN, Geneva, 2014) all figures including auxiliary figures are available at https://atlas.web.cern.ch/Atlas/GROUPS/PHYSICS/CONFNOTES/ATLAS-CONF-2014-018.

[88] *Monte Carlo to Monte Carlo scale factors for flavour tagging efficiency calibration*, Tech. Rep. (CERN, Geneva, 2020) all figures including auxiliary figures are available at https://atlas.web.cern.ch/Atlas/GROUPS/PHYSICS/PUBNOTES/ATL-PHYS-PUB-2020-009.

[89] G. Aad, B. Abbott, D. C. Abbott, A. A. Abud, K. Abeling, D. K. Abhayasinghe, S. H. Abidi, O. S. AbouZeid, N. L. Abraham, and et al., The European Physical Journal C **79** (2019), 10.1140/epjc/s10052-019-7450-8.

[90] *Secondary vertex finding for jet flavour identification with the ATLAS detector*, Tech. Rep. (CERN, Geneva, 2017) all figures including auxiliary figures are available at https://atlas.web.cern.ch/Atlas/GROUPS/PHYSICS/PUBNOTES/ATL-PHYS-PUB-2017-011.

[91] *Topological b-hadron decay reconstruction and identification of b-jets with the JetFitter package in the ATLAS experiment at the LHC*, Tech. Rep. (CERN, Geneva, 2018) all figures including auxiliary figures are available at https://atlas.web.cern.ch/Atlas/GROUPS/PHYSICS/PUBNOTES/ATL-PHYS-PUB-2018-025.

[92] *Optimisation and performance studies of the ATLAS b-tagging algorithms for the 2017-18 LHC run*, Tech. Rep. (CERN, Geneva, 2017) all figures including auxiliary figures are available at https://atlas.web.cern.ch/Atlas/GROUPS/PHYSICS/PUBNOTES/ATL-PHYS-PUB-2017-013.

[93] *Identification of Jets Containing b-Hadrons with Recurrent Neural Networks at the ATLAS Experiment*, Tech. Rep. (CERN, Geneva, 2017) all figures including auxiliary figures are available at https://atlas.web.cern.ch/Atlas/GROUPS/PHYSICS/PUBNOTES/ATL-PHYS-PUB-2017-003.

[94] ATLAS, "Expected performance of the 2019 ATLAS b-taggers," ATL-FTAG-2019-005, [Online; accessed 14-July-2021].

[95] *Measurement of the tau lepton reconstruction and identification performance in the ATLAS experiment using pp collisions at* $\sqrt{s} = 13$ TeV, Tech. Rep. (CERN, Geneva, 2017) all figures including auxiliary figures are available at https://atlas.web.cern.ch/Atlas/GROUPS/PHYSICS/CONFNOTES/ATLAS-CONF-2017-029.

[96] M. Aaboud *et al.* (ATLAS), Eur. Phys. J. C **78**, 903 (2018), arXiv:1802.08168 [hep-ex] .

[97] "ATLAS Luminosity Public Results Run 2," `https://twiki.cern.ch/twiki/bin/view/AtlasPublic/LuminosityPublicResultsRun2` (), accessed 2021-07-20.

[98] G. Aad *et al.* (ATLAS), JINST **15**, P10004 (2020), arXiv:2007.12539 [physics.ins-det] .

[99] *ATLAS level-1 trigger: Technical Design Report*, Technical design report. ATLAS (CERN, Geneva, 1998).

[100] A. R. Martínez (ATLAS), J. Phys. Conf. Ser. **762**, 012003 (2016).

[101] S. Höche, "Introduction to parton-shower event generators," (2015), arXiv:1411.4085 [hep-ph] .

[102] S. Catani, F. Krauss, B. R. Webber, and R. Kuhn, Journal of High Energy Physics **2001**, 063–063 (2001).

[103] M. L. Mangano, M. Moretti, and R. Pittau, Nuclear Physics B **632**, 343–362 (2002).

[104] B. Andersson, *The Lund Model*, Cambridge Monographs on Particle Physics, Nuclear Physics and Cosmology (Cambridge University Press, 1998).

[105] J.-C. Winter, F. Krauss, and G. Soff, The European Physical Journal C **36**, 381–395 (2004).

[106] S. Agostinelli *et al.*, Nuclear Instruments and Methods in Physics Research Section A: Accelerators, Spectrometers, Detectors and Associated Equipment **506**, 250 (2003).

[107] S. Alioli, P. Nason, C. Oleari, and E. Re, Journal of High Energy Physics **2010** (2010), 10.1007/jhep06(2010)043.

[108] T. Sjöstrand, S. Ask, *et al.*, Computer Physics Communications **191**, 159 (2015).

[109] B. P. Nachman (ATLAS Collaboration), *Modeling Radiation Damage to Pixel Sensors in the ATLAS Detector. Modeling Radiation Damage to Pixel Sensors in the ATLAS Detector*, Tech. Rep. (CERN, Geneva, 2017) 12 pages, 13 figures; Talk presented at the APS Division of Particles and Fields Meeting (DPF 2017), July 31-August 4, 2017, Fermilab. C170731, arXiv:1710.03916 .

[110] G. Calderini (ATLAS Collaboration), *The ATLAS ITk detector for High Luminosity LHC Upgrade*, Tech. Rep. (CERN, Geneva, 2022).

[111] (2021).

[112] "Grant R5 chiller and TXF200 circulator," `https://www.grantinstruments.com/scientific/chillers-coolers/r5-series-refrigerated-circulating-bath`, accessed: 2020-10-06.

[113] "Honeywell HIH-4000 humidity sensor," `https://sensing.honeywell.com/honeywell-sensing-hih4000-series-product-sheet-009017-5-en.pdf`, accessed: 2020-08-04.

[114] "OGP CNC-500 smartscope," `https://www.ogpnet.com/products/systems/smartscope-video-multisensor-systems/smartscope-flash-systems/smartscope-cnc-500/index.html`, accessed: 2020-08-04.

[115] A. Mitra, "Warwick Cold Test Setup For Modules," `https://indico.cern.ch/event/674730/contributions/2760651/attachments/1543627/2421832/AUW_Mitra_18Sep17.pdf#search=ATLAS%20ITk%20week%2018%20September%202017`, accessed: 2020-08-04.

[116] Physics Letters B **772**, 879 (2017).

[117] A. M. Sirunyan *et al.* (CMS), JHEP **09**, 051 (2017), arXiv:1701.06228 [hep-ex] .

[118] M. Aaboud *et al.* (ATLAS), Eur. Phys. J. C **78**, 487 (2018), arXiv:1712.06857 [hep-ex] .

[119] *Optimisation of the ATLAS b-tagging performance for the 2016 LHC Run*, Tech. Rep. (CERN, Geneva, 2016) all figures including auxiliary figures are available at https://atlas.web.cern.ch/Atlas/GROUPS/PHYSICS/PUBNOTES/ATL-PHYS-PUB-2016-012.

[120] M. Aaboud, G. Aad, B. Abbott, O. Abdinov, B. Abeloos, D. K. Abhayasinghe, S. H. Abidi, O. S. AbouZeid, N. L. Abraham, and et al., Journal of High Energy Physics **2018** (2018), 10.1007/jhep08(2018)089.

[121] *Measurement of b-tagging Efficiency of c-jets in $t\bar{t}$ Events Using a Likelihood Approach with the ATLAS Detector*, Tech. Rep. (CERN, Geneva, 2018) all figures including auxiliary figures are available at https://atlas.web.cern.ch/Atlas/GROUPS/PHYSICS/CONFNOTES/ATLAS-CONF-2018-001.

[122] *Calibration of light-flavour b-jet mistagging rates using ATLAS proton-proton collision data at $\sqrt{s}$ = 13 TeV*, Tech. Rep. (CERN, Geneva, 2018) all figures including auxiliary figures are available at https://atlas.web.cern.ch/Atlas/GROUPS/PHYSICS/CONFNOTES/ATLAS-CONF-2018-006.

[123] M. Aaboud, G. Aad, B. Abbott, O. Abdinov, B. Abeloos, S. Abidi, O. AbouZeid, N. Abraham, H. Abramowicz, H. Abreu, and et al., Physical Review Letters **120** (2018), 10.1103/physrevlett.120.211802.

[124] L. Lista, *Statistical Methods for Data Analysis in Particle Physics* (Springer, Cham, 2017).

[125] O. Behnke, K. Kröninger, *et al.*, *Data Analysis in High Energy Physics : A Practical Guide to Statistical Methods* (John Wiley Sons, Incorporated, 2013).

[126] S. van der Meer, *Calibration of the effective beam height in the ISR*, Tech. Rep. (CERN, Geneva, 1968).

[127] *Luminosity determination in pp collisions at $\sqrt{s}$ = 13 TeV using the ATLAS detector at the LHC*, Tech. Rep. (CERN, Geneva, 2019) all figures including auxiliary figures are available at https://atlas.web.cern.ch/Atlas/GROUPS/PHYSICS/CONFNOTES/ATLAS-CONF-2019-021.

[128] G. Aad *et al.* (ATLAS), Eur. Phys. J. C **81**, 689 (2021), arXiv:2007.02645 [hep-ex] .

[129] M. Aaboud *et al.* (ATLAS), Phys. Rev. D **96**, 072002 (2017), arXiv:1703.09665 [hep-ex] .

[130] G. Aad, B. Abbott, D. Abbott, A. Abed Abud, K. Abeling, D. Abhayasinghe, S. Abidi, O. AbouZeid, N. Abraham, H. Abramowicz, and et al., Physics Letters B **810**, 135797 (2020).

[131] ATLAS, TRExFitter documentation (Internal), accessed: 2021-12-05.

[132] K. Cranmer, G. Lewis, L. Moneta, A. Shibata, and W. Verkerke (ROOT Collaboration), *HistFactory: A tool for creating statistical models for use with RooFit and RooStats*, Tech. Rep. (New York U., New York, 2012).

[133] W. Verkerke and D. P. Kirkby, eConf **C0303241**, MOLT007 (2003), arXiv:physics/0306116 .

[134] L. Moneta, K. Belasco, K. Cranmer, S. Kreiss, A. Lazzaro, D. Piparo, G. Schott, W. Verkerke, and M. Wolf, "The roostats project," (2011), arXiv:1009.1003 [physics.data-an] .

[135] F. James and M. Roos, Comput. Phys. Commun. **10**, 343 (1975).

[136] F. James *et al.*, MINUIT: Function Minimization and Error Analysis Reference Manual (1998), CERN Program Library Long Writeups.

[137] B. Aubert *et al.* (BaBar), Phys. Rev. D **81**, 032003 (2010), arXiv:0908.0415 [hep-ex] .